LOOKING FOR LEPTON FLAVOUR VIOLATION WITH THE ATLAS DETECTOR

A SEARCH FOR $Z \to \tau l$ DECAYS

Hartger Weits

LOOKING FOR LEPTON FLAVOUR VIOLATION WITH THE ATLAS DETECTOR

A SEARCH FOR $Z \to \tau l$ DECAYS

LOOKING FOR LEPTON FLAVOUR VIOLATION WITH THE ATLAS DETECTOR

A SEARCH FOR $Z \to \tau l$ DECAYS

ACADEMISCH PROEFSCHRIFT

ter verkrijging van de graad van doctor
aan de Universiteit van Amsterdam
op gezag van de Rector Magnificus
prof. dr. ir. K.I.J. Maex
ten overstaan van een door het College voor Promoties ingestelde commissie,
in het openbaar te verdedigen in de Agnietenkapel
op woendag 21 september 2016, te 12.00 uur
door Hartger Weits
geboren te Almelo

Promotiecommissie:

Promotoren:	prof. dr. O.B. Igonkina	Radboud Universiteit Nijmegen
	prof. dr. S.C.M. Bentvelsen	Universiteit van Amsterdam
Overige leden:	prof. dr. ir. P.J. de Jong	Universiteit van Amsterdam
	prof. dr. M.H.M. Merk	Vrije Universiteit
	prof. dr. M.P. Decowski	Universiteit van Amsterdam
	prof. dr. N. de Groot	Radboud Universiteit Nijmegen
	dr. S. Xella	University of Copenhagen
	dr. M. Vreeswijk	Universiteit van Amsterdam

Faculteit der Natuurwetenschappen, Wiskunde en Informatica

This work is part of the research program of the Stichting voor Fundamenteel onderzoek der Materie (FOM), which is part of the Nederlandse organisatie voor Wetenschappelijk Onderzoek (NWO). It was carried out at the Nationaal Instituut voor Subatomaire Fysica (Nikhef) in Amsterdam, the Netherlands.

We're all going to die, all of us, what a circus! That alone should make us love each other but it doesn't. We are terrorized and flattened by trivialities, we are eaten up by nothing [1].

Contents

chapter one

Introduction

The current understanding of particle physics is described by the Standard Model. It's aim is to understand and describe the fundamental laws which are governing the substance of which both us and the things around us are made of. Its paradigm is that everything in existence is made up of a number of building blocks, the fundamental particles. These are fundamental in the sense that they do not have a substructure and that their properties are intrinsic and do not originate from some underlying phenomena.

The image that naturally pops up is that these particles are little billiards balls. The picture is a bit more complicated than that however. The Standard Model is described by a Lagrangian, from which all the physical laws can ultimately be extracted, in the same way as classical systems. Unlike in classical systems however, the entities are not point-like particles or classical fields, but quantum fields. The excitations of the quantum fields correspond to the elementary particles, which makes it possible to describe matter and radiation in the same way.

In the current view everything around us is a big ocean of 17 different fundamental particles which are interconnected through four fundamental forces, namely gravity, electromagnetism and the weak and strong nuclear forces, which is schematically shown in figure 1.1. Because gravity is not incorporated we know that the Standard Model is not a complete picture. But since its finalisation in the mid 1970s it has withstood considerable experimental testing and accurately predicted the existence and properties of new particles that were not yet observed at the time. Among others, it predicted the Z and W boson particles, which were first observed at the UA1 and UA2 experiments at CERN in 1983 [2, 3]. Up until now the Standard Model had successfully described all the observed low energy phenomena, apart from the recent observation that neutrinos can oscillate [4].

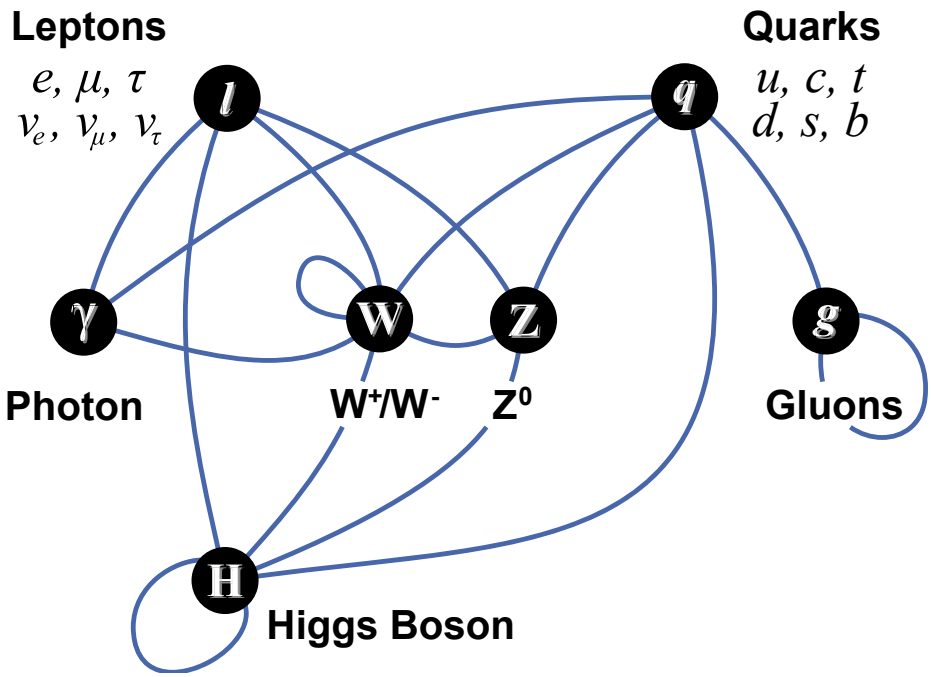

Fig. 1.1 · Quarks carry electric charge, weak isospin, and color charge. Because of this they interact respectively through the electromagnetic, the weak nuclear force, and the strong nuclear force. The leptons don't carry any color charge. Furthermore the three neutrinos do not carry electric charge either, so their motion is directly influenced only by the weak nuclear force, which makes them difficult to detect. The W and Z bosons are the force carriers for the weak interaction, photons for the electromagnetic, and gluons for the strong interaction. The Higgs boson plays a unique role in the Standard Model, by explaining why the other elementary particles, except the photon and gluon, are massive.

In this thesis charged lepton flavour violation is researched. The question why this in an interesting field of research is according to the author best answered in the introductionary text of Bernstein and Cooper [5]:

> Isidor Isaac Rabi's famous question about the muon's existence, "Who ordered that?", was prescient and deep. His question, in modern terms, asked why are there flavours and generations? Why are there muons and taus in addition to the electron? The same question applies to the quark and neutrino sectors. We believe there are three generations in each sector, and that the number in each sector must be the same. We see quarks changing generations, as codified in the Cabibbo-Kobayashi-

> Maskawa matrix, and neutrinos changing from muon to electron to tau neutrinos according to the Pontecorvo-Maki-Nakagawa-Sakata matrix. Lepton Flavour Violation (LFV) is an established fact, but only in the neutral neutrinos. What about their charged partners? Is there Charged Lepton Flavour Violation (CLFV)?

Chapter 1 starts with a theoretical introduction to lepton flavour violation in the Standard Model, and predictions for it from new physics models. Then in chapter 2, the technical design of the Large Hadron Collider and the ATLAS detector is summarised, which provides a basic understanding of how the proton beams are created and how the produced particles from their collision are detected. Subsequently, chapter 3 provides the details of the detector performance in reconstructing and identifying the particles that are used in the search for $Z \to l\tau$ decays, as well as the several Standard Model processes that act as a background. In chapter 4 the constructed measurement model is discussed: a binned likelihood model with the invariant mass of the Z boson as the discriminating variable. Finally, the last chapter gives the unblinded results of the search, using the proton collisions recorded by the ATLAS experiment which totals a recorded luminosity of $\mathcal{L} = 20.3\,\text{fb}^{-1}$.

chapter two

The Standard Model and Lepton Flavour violation

This chapter gives a theoretical introduction to lepton flavour violation in the Standard Model, and predictions for it from new physics models.

2.1 Electroweak Theory

At the end of the 1960s the electroweak theory was formulated in its current form by Weinberg, Salam and Glashow [6–9]. This so-called GWS theory is a gauge theory which combines the electromagnetic and weak nuclear force into a single electroweak force. This electroweak force is mediated by the exchange of particles, the photon and the intermediate vector bosons, W and Z. The other part of the Standard Model is the QCD gauge theory which describes the strong interaction. Since we do not need the strong interaction in the search for lepton flavour violating $Z \to l\tau$ decays, and both parts do not influence each other, only the electroweak interactions will be discussed.

The electroweak Lagrangian [4] for the fermion fields ψ_i is given by

$$\begin{aligned}\mathcal{L}_F = &\sum_I \bar{\psi}_i \left(i\partial\!\!\!/ - m_i - \frac{m_i H}{v} \right) \psi_i \\ &- \frac{g}{2\sqrt{2}} \sum_i \bar{\Psi}_i \gamma^\mu (1-\gamma^5)(T^+ W_\mu^+ + T^- W_\mu^-) \Psi_i \\ &- e \sum_i Q_i \bar{\psi}_i \gamma^\mu \psi_i A_\mu \\ &- \frac{g}{2\cos\theta_W} \sum_i \bar{\psi}_i \gamma^\mu (g_V^i - g_A^i \gamma^5) \psi_i Z_\mu,\end{aligned} \tag{2.1}$$

with

Ψ_i	the left–handed fermion fields $\begin{pmatrix} u_i \\ d_i^I \end{pmatrix}$ and $\begin{pmatrix} \nu_i \\ l_i \end{pmatrix}$
	where $d_i^I = \sum_j V_{ij} d_j$ and V the CKM matrix
H	the Yukawa coupling
g	the gauge coupling constant
θ_W	the weak angle
e	the positron electric charge
Q_i	the charge of ψ_i in units of e
A	the photon field
$W^\pm$	the charged weak boson fields
Z	the neutral weak boson field
$T^\pm$	the weak isospin raising and lowering operators
g_V^i, g_A^i	the vector and axial-vector couplings

In accelerator physics, there are two physical quantities of prime interest, namely decay rates and cross sections. The above Lagrangian predicts these quantities, which can be calculated perturbatively by the use of Feynman diagrams. Each diagram is a topological representation of a physics process and they are built up by glueing together the fundamental vertices[1] of table 2.1.

First one has to find all the diagrams that represent the interaction of interest. Which amounts to selecting all the diagrams that have the corresponding incoming and outgoing particles lines. Each diagram has an amplitude $\mathcal{M}_i$, which can be calculated using the so-called Feynman rules. To find the amplitude of the desired interaction, we simply sum over the number of found diagrams n:

$$\mathcal{M} = \sum_{i=1}^{n} \mathcal{M}_i \tag{2.2}$$

The calculation of the cross section, σ, can be quite involved as it requires calculation of many complicated integrals. For the discussion here, it suffices to say that the cross section is proportional to the matrix element squared like the transition rate:

$$\sigma \propto |\mathcal{M}|^2 \tag{2.3}$$

[1] There are also diagrams representing the coupling among the bosons, but they are not important for our treatment here

Diagram	Vertex Factor
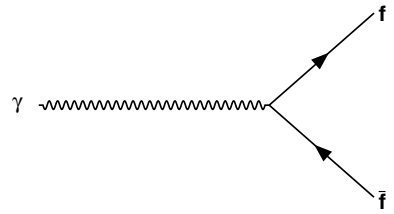	$-ieQ_f\gamma_\mu$
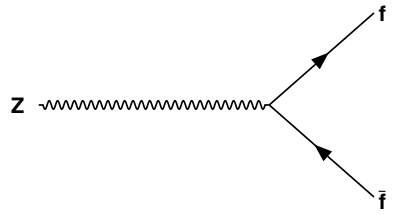	$-i\frac{e}{2\sin\theta_w\cos\theta_W}\gamma_\mu(g_V^f - g_A^f\gamma_5)$
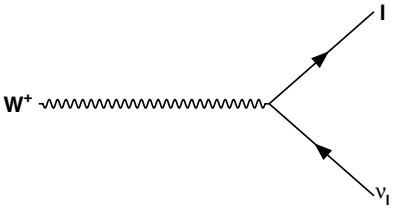	$-i\frac{e}{2\sqrt{2}\sin\theta_w}\gamma_\mu(1-\gamma_5)$
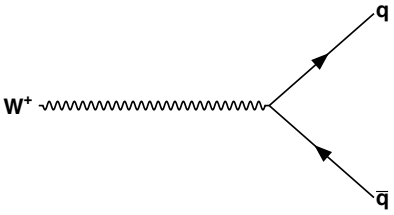	$-i\frac{e}{2\sqrt{2}\sin\theta_w}\gamma_\mu(1-\gamma_5)V_{ij}^{\mathrm{CKM}}$

Table 2.1 · The fundamental vertices and their couplings. V_{ij}^{CKM} is the Cabibbo-Kobayashi-Maskawa matrix which is discussed in more detail in section 2.2. The Dirac matrices are indicated by γ and have specific anticommutation relations.

In principle there are an infinite number of diagrams contributing to a certain physical process. However, because each extra vertex introduces an extra vertex factor which is smaller than 1, the higher order diagrams contribute less to the calculation of $\mathcal{M}_i$, making it possible to predict its value up to an arbitrary precision. From the fundamental vertices of 2.1, a couple of properties of the electroweak theory are already apparent:

Charge conservation: all the interactions must conserve electric charge

Quark flavour violation: the gauge bosons don't couple to the mass eigenstates of the quarks, but to the electroweak flavour eigenstates, which is denoted by the V_{ij}^{CKM} matrix in vertex factor.

Lepton number and flavour conservation: in the electromagnetic vertex the same particle comes out accompanied by a photon. In the weak interaction a lepton can only change into the other lepton of the same generation. However, because neutrino oscillations have been observed, it is already known that this cannot be the complete picture, as will be discussed in the following sections.

2.2 Quark flavour violation

The charged weak interaction is the only process in the Standard Model that does not conserve flavour, as can be seen in figure 2.1. It can transform one type of quark into another one. Furthermore, there is mixing between the quark families. This is caused by the mass eigenstates being different from the interaction eigenstates. The weak force couples to the pairs

$$\begin{pmatrix} u \\ d^I \end{pmatrix}, \begin{pmatrix} c \\ s^I \end{pmatrix} \quad \text{and} \quad \begin{pmatrix} t \\ b^I \end{pmatrix}, \tag{2.4}$$

with d^I, s^I and b^I linear combinations of mass eigenstates d, s and b:

$$\begin{pmatrix} d^I \\ s^I \\ b^I \end{pmatrix} = V_{\text{CKM}} \begin{pmatrix} d \\ s \\ b \end{pmatrix} = \begin{pmatrix} V_{ud} & V_{us} & V_{ub} \\ V_{cd} & V_{cs} & V_{cb} \\ V_{td} & V_{ts} & V_{tb} \end{pmatrix} \begin{pmatrix} d \\ s \\ b \end{pmatrix}. \tag{2.5}$$

The matrix above that holds the coupling for the nine quark transitions is called the Cabibbo-Kobayashi-Maskawa matrix. It is a 3×3 unitary matrix, which can be parameterised by three mixing angles and $\theta_{12}, \theta_{23}, \theta_{13}$, and a single phase called δ responsible for all CP-violating effects in the Standard Model [10–12].

$$V_{\text{CKM}} = \begin{bmatrix} c_{12}c_{13} & s_{12}c_{13} & s_{13}e^{-i\delta} \\ -s_{12}c_{23} - c_{12}s_{23}s_{13}e^{i\delta} & c_{12}c_{23} - s_{12}s_{23}s_{13}e^{i\delta} & s_{23}c_{13} \\ s_{12}s_{23} - c_{12}c_{23}s_{13}e^{i\delta} & -c_{12}s_{23} - s_{12}c_{23}s_{13}e^{i\delta} & c_{23}c_{13} \end{bmatrix}, \tag{2.6}$$

with $s_{ij} = \sin\theta_{ij}$ and $c_{ij} = \cos\theta_{ij}$. The CKM matrix elements are determined using a global fit to all available measurements and imposing constraints from the

Standard Model by the UTfit collaboration [13]. The most recent results are given by:

$$\begin{aligned} \sin\theta_{12} &= 0.22523 \pm 0.00065, \\ \sin\theta_{23} &= 0.0417 \pm 0.00057, \\ \sin\theta_{13} &= 0.0363 \pm 0.00012, \\ \delta &= 69.4 \pm 3.4\ ^\circ. \end{aligned} \tag{2.7}$$

2.3 Neutrino flavour violation

Apart from the discovery of the Higgs boson [14, 15], the observation that neutrinos mix is one of the most significant discoveries in the field of particle physics in recent times [16]. One could argue that it's even more so, as the Higgs boson was already incorporated in the 70s, whereas neutrino mixing requires an extension to the Standard Model.

The observations of neutrino oscillations can be incorporated in the Standard Model in a similar way as quark mixing is treated. However, this requires the neutrino's to be massive so that the familiar flavour eigenstates $\{\nu_e, \nu_u, \nu_\tau\}$ are a quantum superposition of the massive $\{\nu_1, \nu_2, \nu_3\}$ eigenstates. The actual values of the neutrinos masses are still unknown. The most stringent constraint on the total neutrino mass is $\Sigma m_\nu < 0.39$ eV at 95 % confidence level, and comes from the combination of recent cosmic microwave background measurements and galaxy clustering information [17].

In this model the so-called Pontecorvo-Maki-Nakagawa-Sakata matrix quantifies these mixtures in complete analogy to the CKM matrix,

$$\begin{pmatrix} \nu_e \\ \nu_\mu \\ \nu_\tau \end{pmatrix} = V_{\text{PMNS}} \begin{pmatrix} \nu_1 \\ \nu_2 \\ \nu_3 \end{pmatrix}. \tag{2.8}$$

The matrix can be parameterised in the same way as done in equation 2.6, again using three mixing angles $\theta_{12}, \theta_{23}, \theta_{13}$, and a single phase δ related to charge-parity violations. There may also be two phases associated to a possible Majorana character of neutrinos, which is discussed in section 2.4.0.1. However these additional phases are not needed to explain the observation of neutrino oscillations. The minimal model described above using Dirac neutrinos is called the νSM. The mixing angles have been measured by a variety of experiments [18]. The CP-violating phase δ has not been measured directly, but its value can be obtained by fits using the other measurements. All the neutrino measurements are combined by the Nufit collaboration [19]. The results of their global analysis is presented in figure 2.1 which shows the different χ^2 scans of the allowed six-dimensional parameter space.

Although the actual values are still unknown, experiments have given insight in the mass difference between the different eigenstates $\Delta m^2_{ij} = m^2_i - m^2_j$. Oscillation

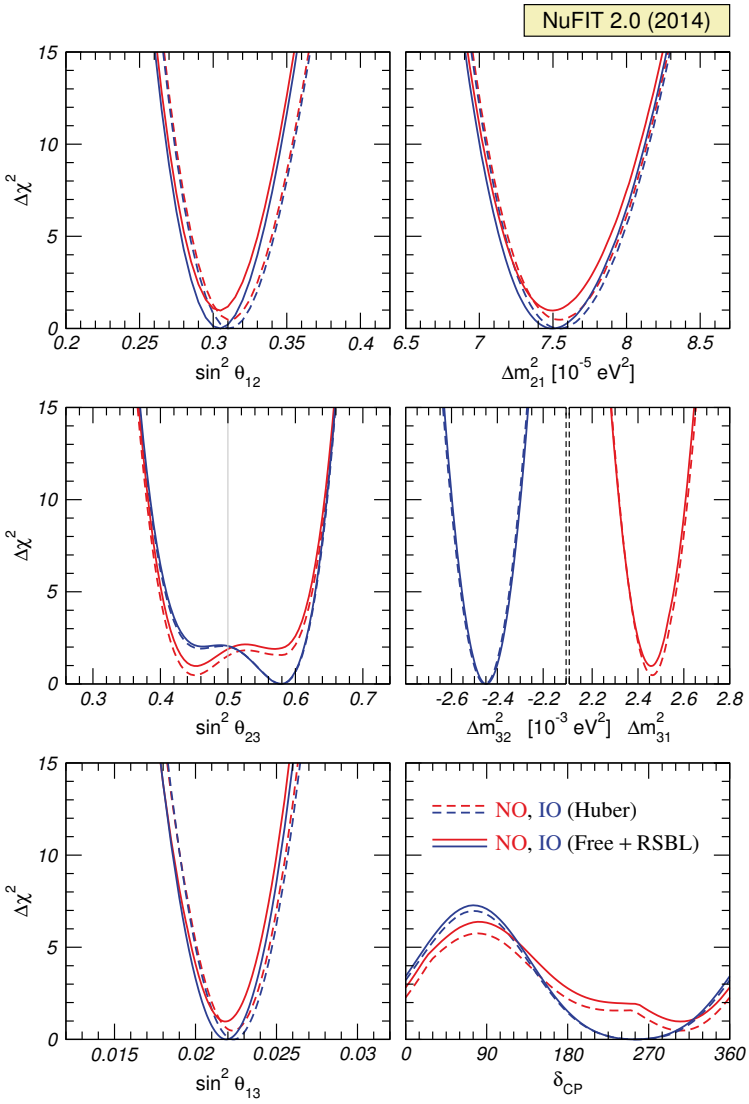

Fig. 2.1 · Results of the global 3ν oscillation analysis. The red and blue curves are for NO and IO ordering respectively. For solid curves the normalisation of reactor fluxes is left free and data from short-baseline (less than 100 m) reactor experiments are included. For dashed curves short-baseline data are not included but calculated reactor fluxes [20] are assumed. The mass-squared splitting Δm^2_{31} for NO and Δm^2_{32} for IO is used. Taken from [19].

measurements indicate that one splitting is quite small, giving rise to two possible mass hierarchies

$$m_1 \simeq m_2 \ll m_3 \Longrightarrow \Delta m^2_{31} > 0 \Longrightarrow \text{normal ordering (NO)}, \tag{2.9}$$

$$m_1 \simeq m_2 \gg m_3 \Longrightarrow \Delta m^2_{31} < 0 \Longrightarrow \text{inverted ordering (IO)}. \tag{2.10}$$

The two hierarchies are depicted schematically in terms of their flavour and mass eigenstates in figure 2.2. Assuming the νSM model as described above, makes

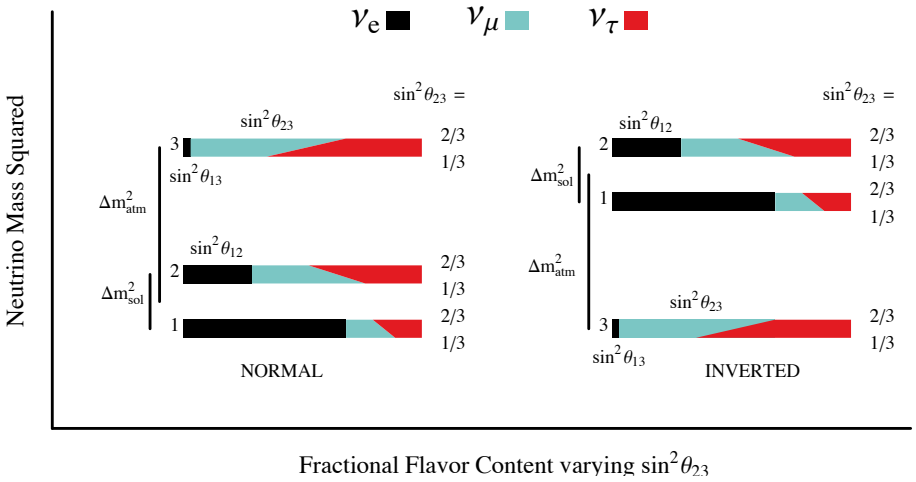

Fig. 2.2 · The range of probability of finding the α–flavour in the i–th mass eigenstate for the two different mass hierarchies. The mixing angle $\sin^2\theta_{23}$ varies over its allowed range at the 90 % C.L. The bottom of the bars is for the minimum allowed value of $\sin^2\theta_{23} \approx 1/3$ and the top of the bars is for the maximum value of $\sin{\theta_{23}}^2 \approx 2/3$. The other mixing parameters are held fixed: $\sin^2\theta_{12} = 0.30$, $\sin^2\theta_{13} = 0.03$ and $\delta = \pi$. One can identify Δm^2_{21} as the neutrino mass squared responsible for the solar ν_e oscillations, and Δm^2_{31} for the dominant atmospheric ν_μ oscillations, therefore they are often denoted as Δm^2_{sol} and Δm^2_{atm} respectively [4]. Illustration taken from [21].

also charged lepton flavour violation possible, however at too small rates to be observable in experiments.

2.4 Fermion mass and mixing

As mentioned before in sections 2.2 and 2.3, flavour violation is strongly connected to the masses of the fermions. The gauge group which describes the weak interaction is $SU(2)_w \times U(1)_Y$, where w stands for weak isospin and Y is called hypercharge [4]. An important concept of the theory are the left– and right–handed fields. They are defined as

$$\psi_L = \frac{1}{2}(1-\gamma^5)\psi, \qquad \psi_R = \frac{1}{2}(1+\gamma^5)\psi. \tag{2.11}$$

The quarks and leptons appear as left-handed doublets:

$$Q^I_{Li} \equiv \begin{pmatrix} u^I_{Li} \\ d^I_{Li} \end{pmatrix}, \quad L^I_{Li} \equiv \begin{pmatrix} \nu^I_{Li} \\ l^I_{Li} \end{pmatrix}, \tag{2.12}$$

and right-handed singlets:

$$u^I_{Ri}, d^I_{Ri}, l^I_{Ri}. \tag{2.13}$$

Here i stands for the three generations of quarks and leptons and I indicates that the interaction basis is used for the fermion fields. From experiments we know that only left–handed neutrinos participate in the weak interactions, and therefore right-handed neutrinos are absent in the Standard Model.

The masses of the quarks and charged leptons appear as bilinears of the form $\bar{\psi}_L\psi_R$ in the Standard Model Lagrangian. However a decomposition in chiral states $-m\bar{\psi}\psi = -m[\bar{\psi}_L\psi_R + \bar{\psi}_R\psi_L]$ would not be gauge invariant since the left-handed doublets and right-handed singlets transform differently under $SU(2)_w \times U(1)_Y$ rotations.

This problem is solved by the Higgs mechanism by writing the mass terms as $\bar{\psi}_{Li}\phi\psi_{Rj}$. By assuming a non-zero vacuum expectation value for the Higgs field ϕ, the gauge symmetry is spontaneously broken:

$$\langle\phi\rangle = \frac{1}{\sqrt{2}}\begin{pmatrix} 0 \\ v \end{pmatrix}, \tag{2.14}$$

and the mass part of the Lagrangian can be written as:

$$-\mathcal{L}_{\text{mass}} = \sum_{i,j=1}^{3}\left(\bar{d}^I_{Li}Y^d_{ij}d^I_{Rj} + \bar{u}^I_{Li}Y^u_{ij}u^I_{Rj} + \bar{l}^I_{Li}Y^l_{ij}l^I_{Rj}\right) + \text{h.c.}\,. \tag{2.15}$$

This part of the Lagrangian describes the interaction between the Higgs doublet and the fermions: the absence of right-handed neutrinos causes the neutrino to be massless. However the observation of neutrino oscillations means that this cannot be the complete picture. The most minimal extension to the Standard Model that

explains this observation is treating the neutrinos as Dirac particles, like the other fermions. The lepton part of the Lagrangian would then read:

$$-\mathcal{L}_{\text{mass}}^{\text{leptons}} = \sum_{i,j=1}^{3} \left(\bar{\nu}_{Li}^{I} Y_{ij}^{\nu} \nu_{Rj}^{I} + \bar{l}_{Li}^{I} Y_{ij}^{l} l_{Rj}^{I} \right) + \text{h.c.} \,. \tag{2.16}$$

The terms Y_{ij}^{ν} and Y_{ij}^{l} are complex 3×3 matrices that describe the strength between the Higgs field and the neutrinos and the charged leptons, and incorporate the so–called Yukawa couplings. To obtain mass eigenstates, these matrices are diagonalised by means of a bi-unitary transformation:

$$M^{\nu} = U_L^{\nu\dagger} Y^{\nu} U_R^{\nu} = \begin{bmatrix} m_{\nu_1} & 0 & 0 \\ 0 & m_{\nu_2} & 0 \\ 0 & 0 & m_{\nu_3} \end{bmatrix}, \tag{2.17}$$

$$M^{l} = U_L^{l\dagger} Y^{l} U_R^{l} = \begin{bmatrix} m_e & 0 & 0 \\ 0 & m_{\mu} & 0 \\ 0 & 0 & m_{\tau} \end{bmatrix}. \tag{2.18}$$

The matrices U are unitary, e.g. $U_L^{\nu} U_L^{\nu\dagger} = \mathbb{1}$, and give the mixings between the different left–handed and right–handed fermions. We can incorporate them and rewrite the Lagrangian:

$$\begin{aligned} -\mathcal{L}_{\text{mass}}^{\text{leptons}} &= \sum_{i,j=1}^{3} \left(\bar{\nu}_{Li}^{I} Y_{ij}^{\nu} \nu_{Rj}^{I} + \bar{l}_{Li}^{I} Y_{ij}^{l} l_{Rj}^{I} \right) + \text{h.c.} \qquad (2.19) \\ &= \sum_{i,j=1}^{3} \left(\bar{\nu}_{Li}^{I} U_L^{\nu} U_L^{\nu\dagger} Y_{ij}^{\nu} U_R^{\nu} U_R^{\nu\dagger} \nu_{Rj}^{I} + \bar{l}_{Li}^{I} U_L^{l} U_L^{l\dagger} Y_{ij}^{l} U_R^{l} U_R^{l\dagger} l_{Rj}^{I} \right) + \text{h.c.} \\ &= \sum_{i=1,2,3} m_{\nu_i} \bar{\nu}_{Li} \nu_{Ri} + \sum_{i=e,\mu,\tau} m_{\nu_i} \bar{l}_{Li} l_{Ri} + \text{h.c.} \,. \end{aligned}$$

Rewriting it this way gives us an expression in terms of the mass eigenstates ν and l instead of the interaction eigenstates ν^I and l^I. The relationship between the two are thus given by:

$$\nu_{Ri} = \sum_{i=1,2,3} (U_R^{\nu\dagger})_{ij} \nu_{Rj}^{I}, \qquad \nu_{Li} = \sum_{i=1,2,3} (U_L^{\nu\dagger})_{ij} \nu_{Lj}^{I}, \tag{2.20}$$

$$l_{Ri} = \sum_{i=1,2,3} (U_R^{l\dagger})_{ij} l_{Rj}^{I}, \qquad l_{Li} = \sum_{i=1,2,3} (U_L^{l\dagger})_{ij} l_{Lj}^{I}. \tag{2.21}$$

We can now rewrite the charged current for the neutrinos and replace the interaction eigenstates with the mass eigenstates:

$$\mathcal{L}^{\nu}_{\text{CC}} = \sum_{i=1}^{3} \bar{\nu}^{I}_{Li}\gamma^{\mu}W^{+}_{\mu}l^{I}_{Li} + \bar{l}^{I}_{Li}\gamma^{\mu}W^{-}_{\mu}\nu^{I}_{Li} \tag{2.22}$$
$$= \sum_{j=1}^{3}\sum_{i=1}^{3} \bar{\nu}_{Li}(U^{\nu\dagger}_{L}U^{l}_{L})_{ij}\gamma^{\mu}W^{+}_{\mu}l_{Li} + \bar{l}_{Li}(U^{l\dagger}_{L}U^{\nu}_{L})_{ij}\gamma^{\mu}W^{-}_{\mu}\nu_{Li}$$

Because the most general mass term cannot be made simultaneously diagonal for both the neutrinos and charged leptons by a redefinition of the left and right-handed fields without producing mixing in the charged current, it is customary to choose the interaction and mass eigenstates to be equal for the charged leptons and rotated for the neutrinos:

$$\nu^{I} = (U^{l\dagger}_{L}U^{\nu}_{L})\nu = U_{\text{PMNS}}\,\nu, \tag{2.23}$$
$$l^{I} = l, \tag{2.24}$$

with the unitary 3×3 PMNS matrix named after Pontecorvo, Maki, Nakagawa and Sakata which is discussed in section 2.3. This means the flavour eigenstate $|\nu\rangle$ is now a superposition of the mass eigenstates, which explains the observed neutrino oscillations:

$$|\nu_{\alpha}\rangle = \Sigma_{i}(U^{l\dagger}_{L}U^{\nu}_{L})_{\alpha i}|\nu_{i}\rangle, \tag{2.25}$$

The observed mixing in U_{PMNS} depends on both the charged and neutrino mixing matrices, and there is not a way to separately measure U^{l} or U^{ν}. The same procedure can be followed to determine the mixing in the quark sector. Here it is customary to choose the interaction and mass eigenstates to be equal for the up–type quarks and the rotated for the down–type quarks:

$$u^{I} = u \tag{2.26}$$
$$d^{I} = (V^{d}_{L}V^{u\dagger}_{L})d = V_{\text{CKM}}d \tag{2.27}$$

with the unitary 3×3 CKM matrix discussed in section 2.2.

Dirac versus Majorana

In the above discussion neutrino oscillations were incorporated in the Standard Model by adding right–handed neutrinos. From experiments however, it has been observed that neutrinos are always produced in predominantly left–handed states, or right–handed in the case of anti–neutrinos [4]. A possible solution to this predicament is that they are singlet under all gauge interactions, which is referred to as sterile neutrinos. In this scenario, ν_R and $\bar{\nu}_L$ will have no gauge interactions and will thus not couple to the W and Z bosons. Because of their mass they would have a gravitational interaction though and could possibly explain phenomena in

astrophysics like dark matter, baryogenesis or dark radiation based on the seesaw theory [22, 23].

Because the neutrino is electrically neutral, there is also the possibility that it is not a Dirac particle like the quarks and charged leptons, but a Majorana particle. In that case the neutrino and anti–neutrino would be the same particle:

$$\nu = \nu^c = \mathcal{C}\bar{\nu}^T, \tag{2.28}$$

with the charge conjugation operation $\mathcal{C} = i\gamma^2\gamma^0$. Their fields are defined as:

$$\nu^M = \nu_L + \nu_L^c = \nu_L + \mathcal{C}\bar{\nu}^T, \tag{2.29}$$

and do not need additional right-handed neutrinos in the mass part of the Lagrangian:

$$\begin{aligned} -\mathcal{L}_{\text{mass}}^{\nu,\text{Majorana}} &= \frac{m}{2}\left(\bar{\nu}_L^c \nu_L + \bar{\nu}_L \nu_L^c\right) \\ &= \frac{m}{2}\left(-\nu_L^T \mathcal{C}^\dagger \nu_L + \bar{\nu}_L \mathcal{C}\bar{\nu}_L^T\right) \\ &= \frac{m}{2}\bar{\nu}^M \nu^M. \end{aligned} \tag{2.30}$$

Which apart from the factor $\frac{m}{2}$ is similar to the Dirac mass term. However the Majorana mass term cannot be generated through the standard Higgs mechanism, which would mean that an extension is needed, such as introducing a Higgs triplet [24]. Furthermore lepton number would no longer be conserved, making it possible to have neutrinoless double beta decay. The search for these rare decays are ongoing as

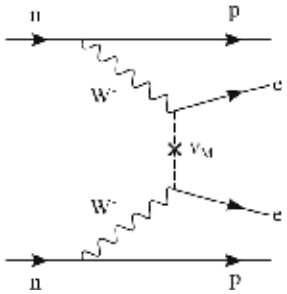

Fig. 2.3 · The neutrinoless double beta decays emit only two electrons, which is possible if the neutrino and anti–neutrino are the same particle. This process would violate the lepton number by two units. Taken from [25]

its experimental observation would prove that the neutrinos would have a Majorana component [26]. In addition this decay could potentially give information on the neutrino mass scale, hierarchy, and Majorana phases in the PMNS matrix.

2.5 Charged lepton flavour violation

As discussed in the previous section, massive neutrino's and the PMNS matrix can incorporate the observation of neutrino mixing and generate charged lepton flavour violating decays in the νSM, through oscillations in loop diagrams as depicted in figure 2.4. However, such transitions are suppressed by sums over $(\Delta m_{ij}/m_W)^4$ and make the charged lepton flavour violation (cLFV) decay rates such as $Z \to l_\alpha l_\beta$ completely negligible, calculations estimate the branching fraction in the order of 10^{-54} [27]. This makes any observation of these decays an unambiguous sign of physics beyond the νSM.

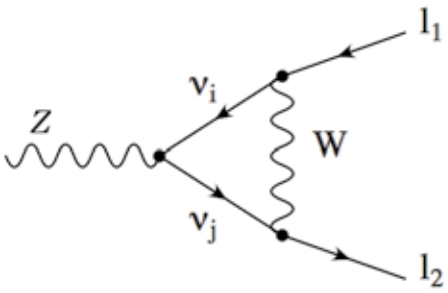

Fig. 2.4 · A Feynman diagram contributing to the νSM decay of $Z \to \mu\tau$. Taken from [27]

Searches for charged lepton flavour violation have been performed and are ongoing through a wide range of experiments investigating the decays of muons, taus and mesons [5]. The LHC produces large amounts of Z bosons, making it possible to explore lepton flavour violation in the production of leptons. The LFV Z decays are complementary to these rare lepton decay searches as effective LFV Z couplings can also be constrained from decays such as $l_i \to l_j l_k \bar{l}_k$ and $l_i \to l_j \gamma$, as shown in figure 2.5 [28–30].

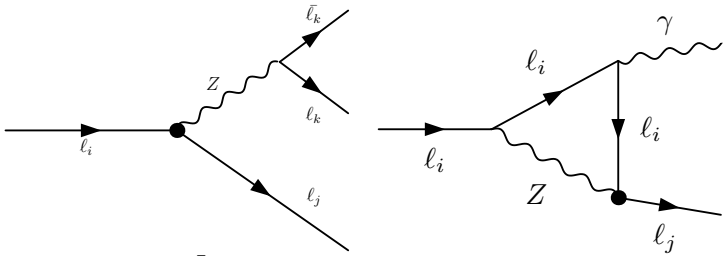

Fig. 2.5 · Feynman diagrams for the three-body $l_i \to l_j l_k \bar{l}_k$ on the left and the radiative decay $l_i \to l_j \gamma$ using the effective Lagrangian approach. The solid round dot represents an effective Z coupling. Taken from [31]

The $Z \to l\tau$ decays have been investigated in the past by other experiments, both of the most sensitive searches have been performed at the LEP collider. The

worldwide upper limit on Br($Z \to \mu\tau$) is set by the DELPHI experiment at 1.2×10^{-5} [32] and the limit on Br($Z \to e\tau$) is set by the OPAL experiment at 9.8×10^{-6} [33], with a confidence level of 95 %. Flores-Tlalpa et al. have made general predictions on the $Z \to l_i l_j$ decay rates from the current experimental bounds on low energy processes, by means of the effective Lagrangian approach [31]. The constraints on $Z \to \tau e$ are weaker than the current direct measurements and similar for $Z \to \tau\mu$, as can be seen in table 2.2.

	$l_i \to l_j l_k \bar{l}_k$	$l_i \to l_j \gamma$
Br($Z \to e\tau$)	$\leq 1.7 \times 10^{-5}$	$\leq\sim 10^{-5}$
Br($Z \to \mu\tau$)	$\leq 1.0 \times 10^{-5}$	$\leq\sim 10^{-5}$

Table 2.2 · Constraints on the $Z \to l_i l_j$ decays obtained from the experimental bounds on $l_i \to l_j l_k \bar{l}_k$ and $l_i to_j \gamma$. Adapted from [31].

$Z \to l\tau$ decays are a sensitive probe for new physics because they are extremely suppressed in the SM but can be greatly enhanced in new physics models like supersymmetry and the seesaw mechanism.

2.5.1 Leptogenesis

The lack of antimatter in the observable universe is one of the big questions in the field of physics. Assuming that the Big Bang produced equal amounts of matter and antimatter, one would naively expect that they would cancel each other out. Protons would annihilate with antiprotons, electrons with positrons, muons with antimuons, et cetera, producing an ocean of radiation without matter or antimatter left in the universe.

Andrej Sakharov suggested in 1967 [34] that this imbalance could be caused by the fact that matter and antimatter can behave differently through the violation of the CP symmetry. The CP transformation entails flipping the sign of the space coordinates and charges of the elementary particles. Current efforts try to explain the antimatter conundrum with a dynamical generation mechanism called baryogenesis, which includes CP violation.

Unfortunately, or fortunately depending on your point of view, the current Standard Model cannot accomodate a successful model of baryogenesis and has to be extended. A popular mechanism of baryogenesis is called leptogenesis, where an asymmetry in the very early universe results in the dominance of leptons over antileptons. Consequently this lepton number excess transforms into baryon number excess through a time-independent solution to the electroweak field equations called a sphaleron. This motivates searches for cLFV, because theory models explaining leptogenenesis predict these decays.

A popular modification to the Standard Model was suggested by M. Fukugita and T. Yanagida in 1986 [35] which permits this process. Right-handed neutrinos

are added to the Standard Model, and consequently through the so-called seesaw mechanism the neutrinos obtain their mass. In this model the decay of right-handed neutrinos produces leptons, which are converted to baryons through the sphalerons.

2.5.2 Seesaw Mechanism

The addition of right-handed Dirac neutrinos to the Standard Model can solve the problem of neutrino oscillation, however it raises the question why they are so much lighter than the other fermions. A minimal extension of the Standard Model which is able to explain why they are so light, is given by the seesaw mechanism [36–38]. It involves the electroweak scale $\epsilon \sim 10^2 - 10^3$ GeV, and a larger mass scale typically of the order $\Lambda \sim 10^{10} - 10^{14}$ GeV or even as high as the Planck scale:

$$0 < \epsilon \ll \Lambda. \tag{2.31}$$

In this model the right-handed neutrinos interact through the Higgs mechanism as discussed in section 2.4, but in addition a Majorana mass term is added:

$$-\mathcal{L}^{\nu}_{\text{mass}} = \sum_{i,j=1}^{3} \left(Y^{\nu}_{ij} \bar{\nu}_{Li} \nu_{Rj} + \frac{1}{2} \nu^{T}_{Ri} M^{R}_{ij} \nu_{Rj} \right) \tag{2.32}$$

In this way the neutrino masses would be the result of an interplay between the Dirac mass matrix m_D and the Majorana mass matrix M_R neutrino mass term after the electroweak symmetry breaking. The effective neutrino mass matrix M^{ν} after the electroweak symmetry breaking is given by:

$$M^{\nu} = \begin{bmatrix} 0 & m_D \\ m_D^T & M_R \end{bmatrix}. \tag{2.33}$$

The diagonalisation of the neutrino mass matrix yields a superlight neutrino with mass of order ϵ^2/Λ and a superheavy neutrino with mass of order Λ. The smallness of the neutrino masses follow from the combination of two larger scales and not a fine–tuning of the Standard Model parameters; physics waiting at very high energies might manifest itself at low energies through the light neutrinos.

Furthermore the possible existence of heavy neutrinos at some higher energy scale can enhance the lepton flavour violating Z decays. A calculation of the branching ratio $\text{Br}(Z \to \mu\tau)$ in presence of heavy Dirac or Majorana that mix with lighter neutrinos taking into account the present experimental results is shown in figure 2.6. The observed branching fraction strongly depends on the mass of these heavy neutrinos. As can be seen heavy neutrinos that are still outside the range of the current energy of collider experiments, can produce a detectable rate of lepton flavour violating Z decays, making these decays a convenient probe.

2.5.3 Supersymmetry

Supersymmetry (SUSY) is a generalisation of the space-time symmetries that transforms fermions into bosons and vice versa [40]. Each particle from one group is

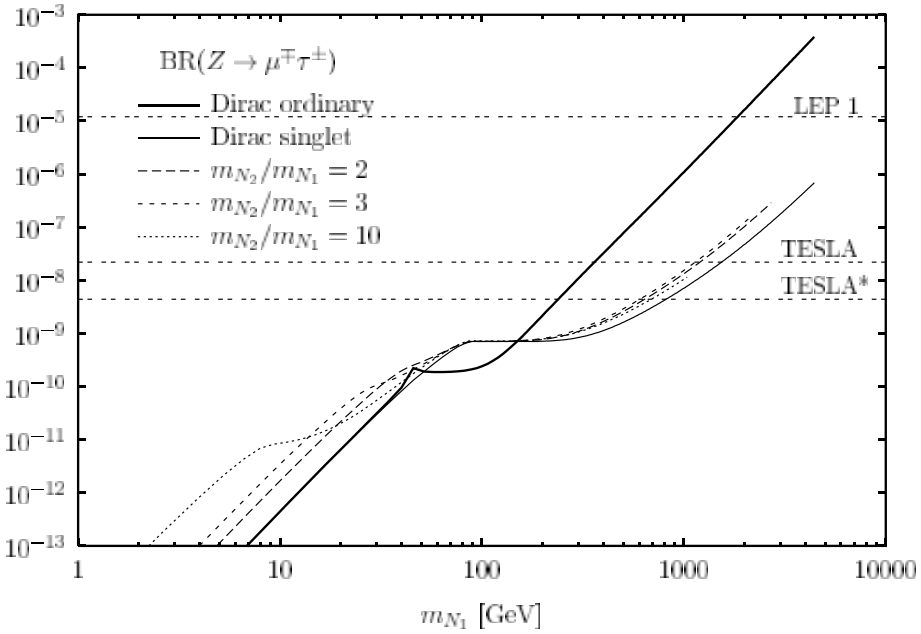

Fig. 2.6 · The upper limit of Br($Z \to \mu\tau$) assuming a light neutrino sector mixing with an additional heavy neutrino. The thick–solid, thin–solid and dashed lines depict a heavy ordinary Dirac, singlet Dirac and two heavy right-handed singlet Majorana neutrinos respectively with a mass of m_{N_1} and m_{N_2}. The horizontal lines indicate the observed limit from the LEP experiment and the expected sensitivity of the TESLA experiment, a proposed linear collider that recently merged into the International Linear Collider project. Taken from [39].

associated with a particle from the other, known as its superpartner, the spin of which differs by a half-integer. If supersymmetry were an exact symmetry of nature, then particles and their superpartners would have the same mass. Since superpartners have not been observed yet, supersymmetry must be a broken symmetry [41, 42].

The popular mSUGRA combined with the seesaw mechanism predicts large flavour mixings of sleptons at the weak scale [43]. Both the charged sleptons and the left-handed sneutrinos could have mixings in flavour space. The flavour mixing of the charged sleptons induces the neutral $\tilde{\chi}^0_\alpha l_I \tilde{l}_J$ and $Z\tilde{l}_I\tilde{l}_J$ couplings, while the flavour mixing of left-handed sneutrinos induces the charged $\tilde{\chi}^+_\alpha l_I \tilde{\nu}_J$ couplings. These flavour-changing couplings will contribute to the LFV Z-decays shown in figure 2.7.

Using the constraints from current neutrino oscillation experiments and introducing two right-handed neutrinos with masses of 10^{13} and 10^{15} GeV the branching

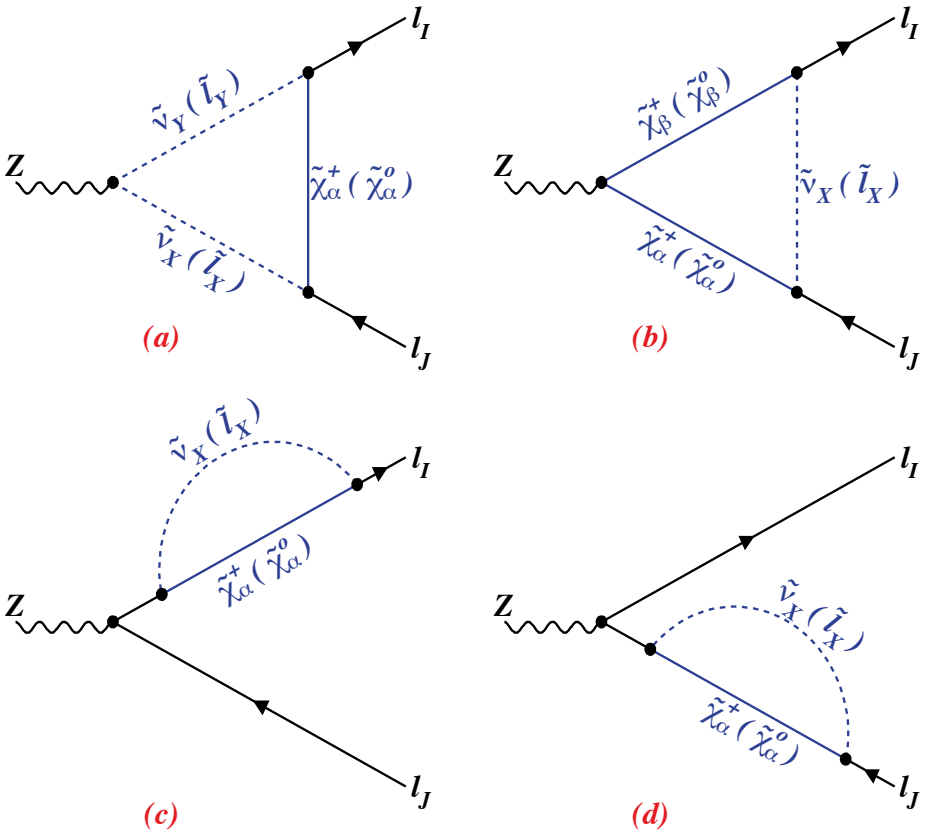

Fig. 2.7 · Feynman diagrams of SUSY contributions to the LFV processes $Z \to l_i l_j$, taken from [43].

ratio of $Z \to \tau\mu$ can be enhanced up to 10^{-8} and thus may serve as a probe of supersymmetric seesaw models.

2.5.4 Higgs doublet

The recent discovery of a new boson with a mass of around 125 GeV at the both the ATLAS [14] and CMS [15] experiment, seems to strongly indicate that it is indeed the Higgs boson as predicted by the Standard Model. One of the objectives of the LHC is to now measure precisely the properties of this boson, like its spin, parity and the Yukawa couplings. In the search for possible new physics the lepton flavour violating $H \to \mu\tau$ has been both measured at ATLAS [44] and CMS [45]. An excess of events with a significance of 2.4 σ was reported by CMS, which corresponds to a branching fraction of $(H \to \tau\mu) = 0.84^{+0.39}_{-0.37}\%$. ATLAS observed

a smaller excess of events of 1.3 σ, corresponding with a best fit value on the branching fraction of $(H \to \tau\mu) = 0.77^{+0.62}_{-0.62}\%$.

Under the assumption that the observed excess of CMS is caused by new physics, the lepton flavour violation in a generic two-Higgs-doublet model has been studied in [46]. The two-Higgs-doublet model consists of two CP–even neutral Higgs bosons h and H, one CP–odd pseudo-scalar A, and two charged Higgs bosons $H^{\pm}$. This model introduces new couplings to the Z bosons as shown in figure 2.8, which results in an upper limit on the branching fraction of $\mathrm{Br}(Z \to \mu\tau) < 10^{-6}$, when using the constrained parameters that fit the CMS results.

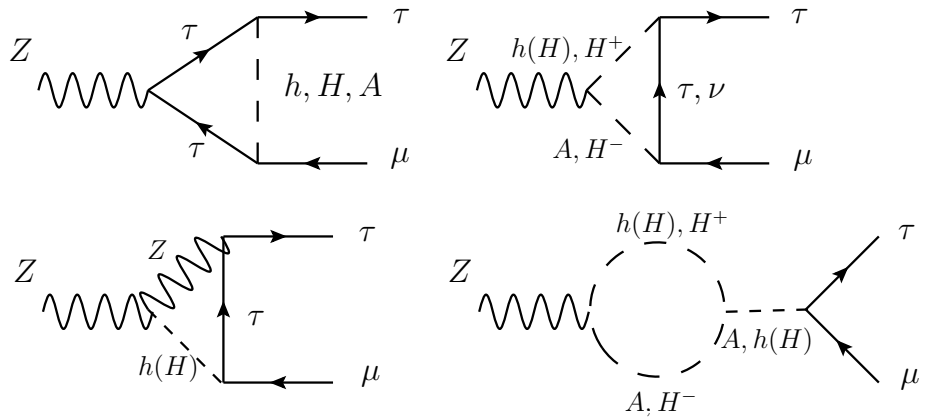

Fig. 2.8 · Feynman diagrams contributing to $Z \to \mu\tau$ decays in a generic two-Higgs-doublet model. Taken from [46].

Conclusion

Flavour violation is observed both in the quark and neutrino sector. The recent observation of lepton flavour violation for neutrinos can be incorporated by the minimal extension of the Standard Model, the so-called νSM. The νSM makes charged lepton flavour violation (cLFV) theoretically possible, but unobservably small. However there is a strong motivation to search for cLFV processes as they can possibly explain the matter and anti–matter asymmetry and the physics behind the neutrino masses. Furthermore many theoretical models predict a sizeable branching fraction of $Z \to \tau l$ decays, up to current upper limits, making them interesting channels to probe in experiments.

chapter three

The LHC and the ATLAS detector

This chapter summarises and discusses the technical designs of the Large Hadron Collider and the ATLAS detector which are relevant for the charged lepton flavour search described in this thesis.

3.1 CERN

The Conseil Européen pour la Recherche Nucléaire (CERN) was founded in 1954 by 12 European states. Its goal was for the European countries to work together on fundamental nuclear research. At the time of writing it's celebrating its 62th anniversary and has expanded to 21 member states with many non-European countries contributing to the financing, construction and operation of the experiments. Over 600 institutes and universities participate in the project and half of the world's particle physicists has come to CERN at one point in their research. [47]

It has been a large contributor in our current fundamental understanding of matter, which is expressed in the many Nobel prizes it facilitated [48, 49]. Furthermore it has driven technical development. Notable examples are the World Wide Web technology that it made available on a royalty-free basis [50] and the development of detectors that are key in modern PET scans [51].

CERN has an intimate history with the Z boson, which is used to probe for lepton flavour violation in this thesis. This neutral boson was first discovered at the laboratory in 1983 by the UA1 and UA2 experiments [2, 3] and its properties were precisely determined between 1989 and 2000 by the experiments situated at the electron positron LEP collider [52]. The excavated tunnel from the LEP accelerator is currently being re–used for the Large Hadron Collider.

3.2 LHC

The Large Hadron Collider (LHC) is the most powerful particle collider ever built. At full operating power it will collide proton beams at a record centre-of-mass energy of 14 TeV with a peak luminosity of $\mathcal{L} = 10^{34}\text{cm}^{-2}\text{s}^{-1}$. It can also collide heavy ions such as lead, with an energy of 2.8 TeV per nucleon with a peak luminosity of $\mathcal{L} = 10^{27}\text{cm}^{-2}\text{s}^{-1}$ [53].

To achieve these highly energetic proton beams a succession of machines and pre–existing accelerators are used, as schematically depicted in figure 3.1. The process can be summarised as follows:

- Hydrogen gas from a bottle is fed into a duoplasmatron, which strips off its electrons, and the produced protons are sent to the linear accelerator Linac2 using a radio frequency quadrupole [54].
- Linac2 accelerates the protons to an energy of 50 MeV
- The protons are then further accelerated by three successive synchrotrons:
  - the Proton Synchrotron Booster: from 50 MeV to 1.4 GeV
  - the Proton Synchrotron: from 1.4 GeV to 25 GeV
  - the Super Proton Synchrotron: from 25 GeV to 450 GeV
- Finally the protons are injected into the LHC both in a clockwise and an anti-clockwise direction. The almost circular LHC is 26.6 km in circumference and it takes around 20 minutes to accelerate the protons from 450 GeV to the maximum energy of 7 TeV.

To save costs the LEP tunnel and its injection chain are re–used. The electron and positron beams of the LEP experiment were housed in a single ring. A consequence of having counter-rotating particles of the same charge is that two separate rings are needed to provide the opposed electrical and magnetic fields. Accommodating two completely separate proton rings in the 3.7 meter diameter tunnel would have been difficult. This lack of space is the main reason that the twin bore super-conducting magnet system depicted in figure 3.2 is used. It consist of two sets of coils and beam channels within the same mechanical structure and cryostat. To keep the trajectory of the beams circular, the magnet system consists of 1232 dipole magnets of 15 meters long. The LHC relies on superconducting magnets using niobium-titanium alloy cables, which are cooled down to 1.9 K using superfluid helium, which provide a magnetic field strength of 8.33 T.

To control the trajectory of the protons several pieces of hardware are employed: the dipole magnets maintain the almost circular orbits, quadrapoles are used to focus the beam and radio frequency cavities accelerate the particles and compensate for energy losses. Additional sextupoles and decapoles are also in place for higher order corrections to the manipulate the beam path.

The protons fly around the LHC ring in bunches, which is a consequence of the acceleration scheme. They can only be accelerated when the electromagnetic field has the correct orientation as they pass through the radio frequency cavities. In 2012, the proton beam consisted of roughly 1374 bunches which were separated by a spacing of 50 ns, each of which in turn contains around 1.6×10^{11} protons. A bunch has the dimensions of a few centimers long and a millimeter wide, however it is squeezed to about 16 μm at the collision points to increase the probability of an interaction [55].

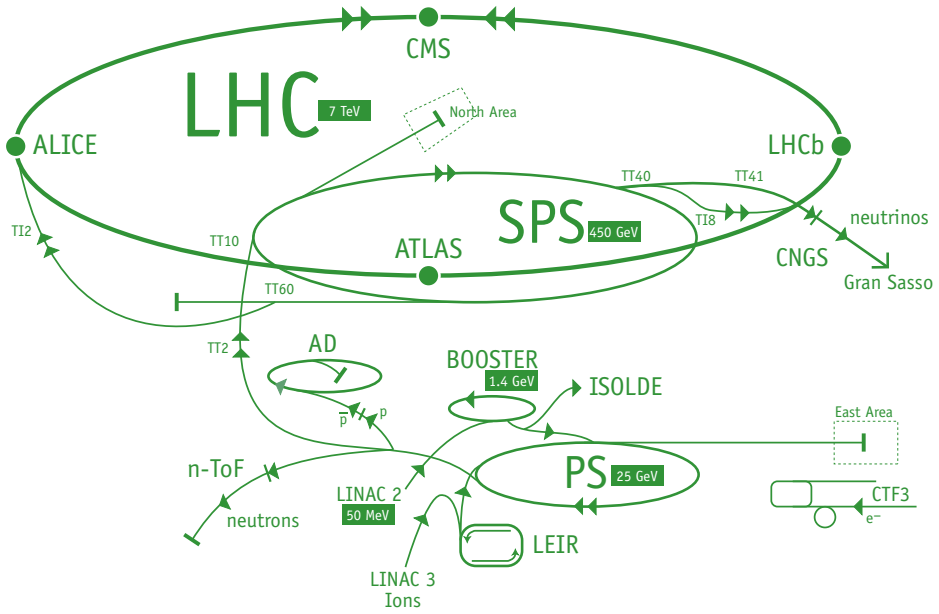

Fig. 3.1 · The accelerator complex at CERN creates a pair of clockwise and anti-clockwise proton beams at centre-of-mass energy of 14 TeV from a bottle of hydrogen gas. Taken from [55].

The proton beams smash into each other at four collision points, around which four underground caverns are built. These caverns host the six experiments installed at the LHC: A Large Ion Collider Experiment (ALICE) [56], A Toroidal LHC ApparatuS (ATLAS) [57], the Compact Muon Solenoid (CMS) [58], the Large Hadron Collider beauty (LHCb) experiment [59], the Large Hadron Collider forward (LHCf) experiment [60] and the TOTal Elastic and diffractive cross section Measurement (TOTEM) experiment [61]. The smaller TOTEM and LHCf experiments are installed near CMS and ATLAS respectively.

3.3 ATLAS

The LHC has two general-purpose high luminosity experiments, ATLAS and CMS, both designed to cover a wide range of physics using different designs and technologies. The ATLAS collaboration consists of over 5000 scientists from around 180 institutes (March 2016) from 38 different countries, making it one of the largest scientific cooporations in history [62].

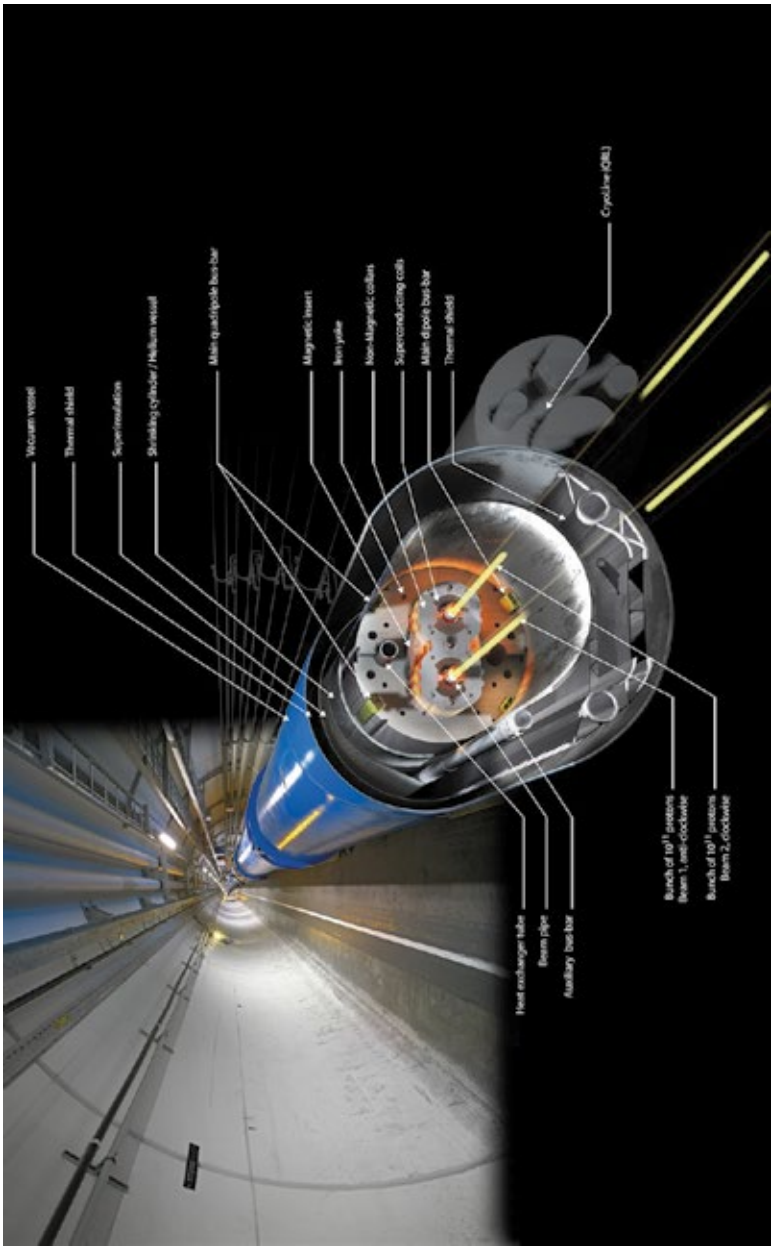

Fig. 3.2 · A cutout of the LHC twin bore magnet system.Taken from [55].

Fig. 3.3 · An image of the ATLAS detector. It is the largest collider-detector even constructed, being 46 m long, 25 m high and 25 m wide and weighing 7000 tonnes. Note the one–armed lady and disproportionally large shouldered man for sense of scale. Taken from [57].

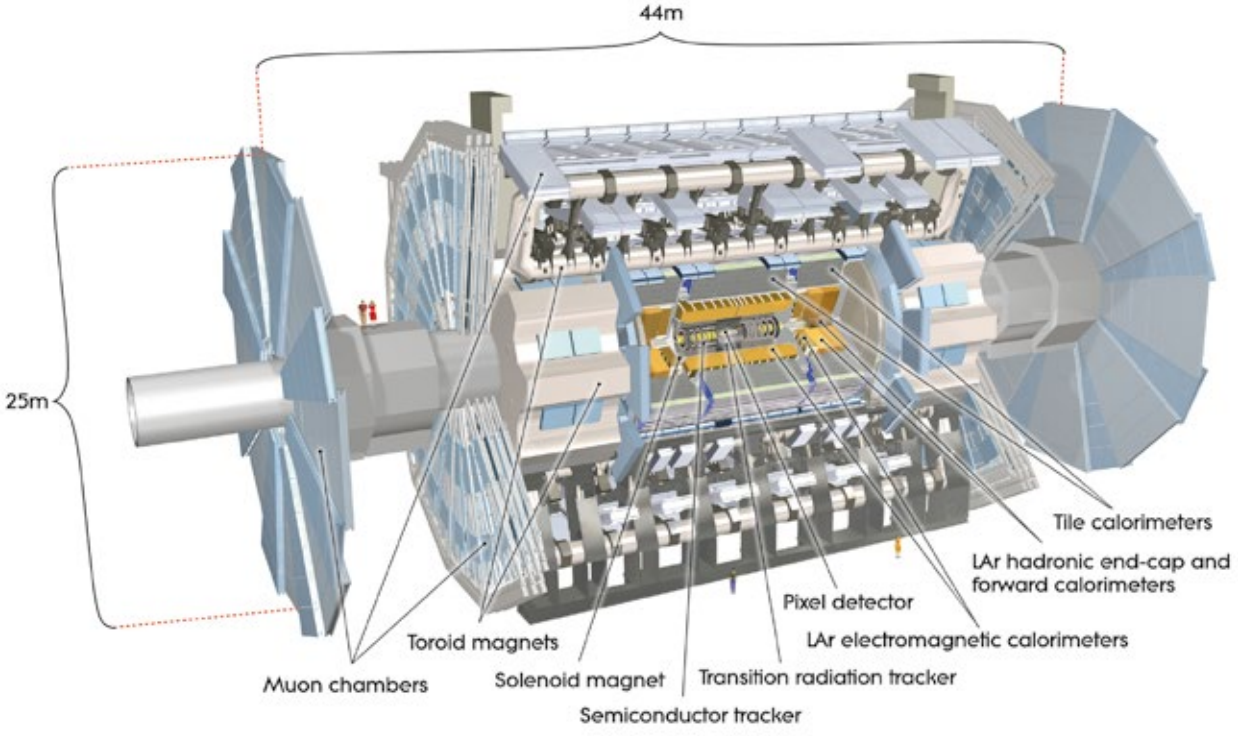

The ATLAS detector, shown in figure 3.3, is the largest collider-detector ever constructed, being 46 meters long, 25 meters high and 25 meters wide and weighing 7000 tonnes. It provides an almost hermetic coverage around the beam–pipe, and is characterised by a very large superconducting magnet system which has been the driving force of the detector design. The various sub–detectors are installed in layers around the interaction point.

The produced stable and relatively long-lived particles are the observables of the high energy collisions. To detect and identify these particles and reconstruct the underlying physical process is quite challenging giving the busy environment. The detection and identification are based on how the different particles interact with the material of the detector, each leaving an unique fingerprint as they pass through the various sub–systems, as illustrated in figure 3.4. The design and performance of the sub–detectors are discussed in the subsequent sections.

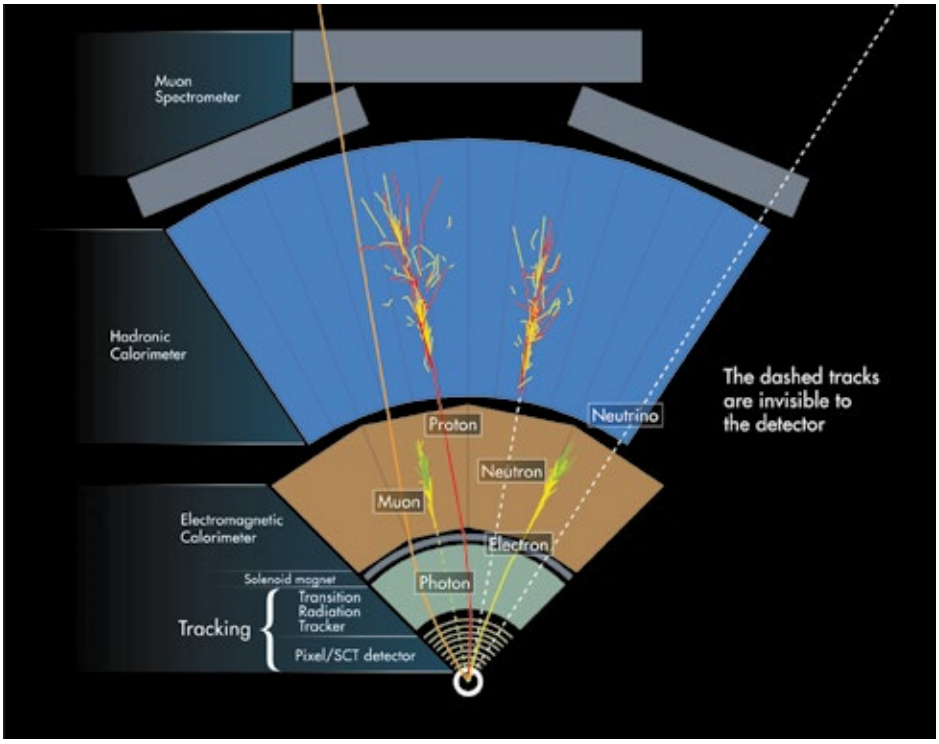

Fig. 3.4 · An illustration of the different particles signatures in the ATLAS detector. Taken from [63].

Magnet system and inner detector

A schematic of the ATLAS magnet system is shown in figure 3.5. It consists of a solenoid encircling the inner detector for which it provides a 2 T strong magnetic field along the beam-pipe. There is also a barrel toroid and two end-cap toroids, which produce toroidal magnetic fields for the central and end–cap regions of 0.5 T and 1 T respectively.

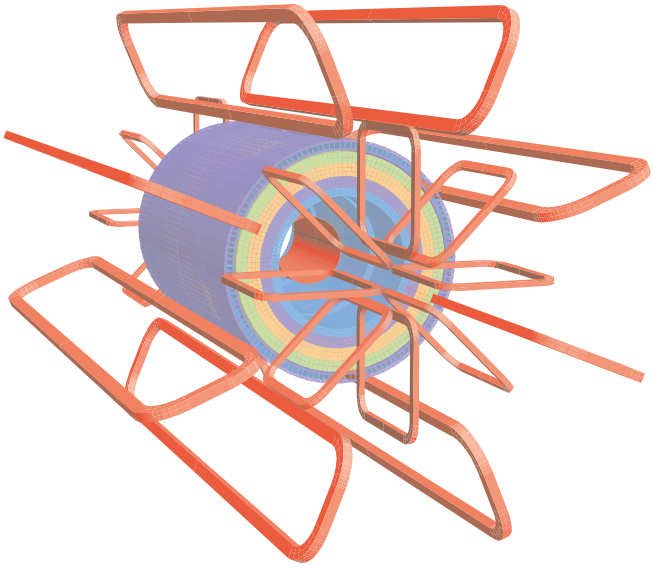

Fig. 3.5 · The geometry of the ATLAS magnet system which has been the driving force of the detector design. The solenoid depicted as blue lies inside of the calorimeter encircling the inner detector. The eight–fold barrel coils and smaller end–cap toroid coils are depicted in red. Taken from [57].

When a charged particle moves through the magnetic field of the inner detector, it traces out a helix. Its initial z-component of the momentum remains unaltered and in the transverse plane it traces out a circle. This path is described in ATLAS convention by the five track parameters $\{z_0, d_0, \phi_0, \theta, q/p\}$. From these 5 track parameters the algebraic expression of the trajectory is given by.

$$x = r\sin(\phi_0 + l/r) - (r + d_0)\sin\phi_0 \tag{3.1}$$
$$y = -r\cos(\phi_0 + l/r) + (r + d_0)\sin\phi_0 \tag{3.2}$$
$$z = z_0 + l/\tan\theta \tag{3.3}$$
$$p_x = p_T\cos(\phi_0 + l/r) \tag{3.4}$$
$$p_y = p_T\sin(\phi_0 + l/r) \tag{3.5}$$
$$p_z = p_T/\tan\,\theta \tag{3.6}$$

Variable l is the distance travelled in the transverse plane and the radius of the circle in the transverse plane $r = \frac{p_T}{|q|B_z}$. So when three points of the track are measured, the curvature thus the transverse momentum is known. A high p_T particle will appear as a straight line; a lower p_T particle will be more curved. When a low p_T particle dissipates all its energy to the detector, the descending radius gives rise to a spiral.

Instead of the track parameter θ, the pseudorapidity $\eta \equiv -\ln \tan \frac{\theta}{2}$ is frequently used as a spatial coordinate. It has the convenient property that differences in this quantity are Lorentz invariant.

When a produced charged particle travels at relativistic speeds through the material of the inner detector, it loses energy through electromagnetically interacting with the electrons of its atoms. By measuring the trail of ionised atoms and liberated electrons it is possible to reconstruct the trajectory of this particle. The inner detector has three different system to do this: the pixel detector, the semiconductor tracker (SCT) and the transition radiation tracker (TRT) which is shown in figure 3.6.

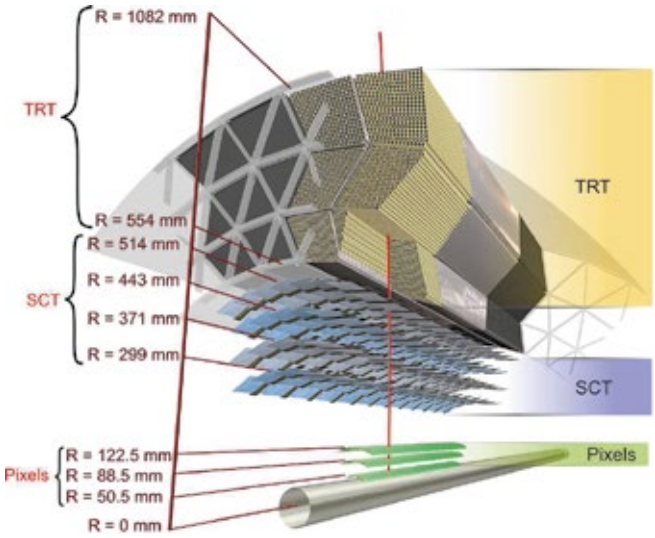

Fig. 3.6 · Drawing showing the inner detector. The design of the detector is such that a particle originating from the interaction point crosses three pixel layers, eight SCT strip layers and around 36 TRT straws, giving on average 43 position measurements on a track. Taken from [57].

The most precise tracking is done by the pixel detector close to the interaction point, which consists of silicon pixels with a surface of 50×400 μm. When a charged particle traverses the doped wafer, electron hole pairs are created by the ionisation and will be registered by the detector. Then signal is read out through amplification electronics and by combining the lit up pixels the path can be determined. The semi

conductor tracker works in the same way, but has large strips of $80\,\mu\text{m} \times 12\,\text{cm}$ instead of pixels.

The Transition Radiation Tracker is a drift–tube system comprising of 370,000 straws [64]. The straws are of 4 mm diameter in diameter and are kept at -1500 V, acting as cathodes. In the middle they each have a 30 μm diameter gold-plated tungsten wire and are filled with a gas mixture of Xe, CO_2 and O_2. This mixture increases the electron drift velocity and is used for photon-quenching. When a charged particle traverses a drift–tube it ionises the gas mixture, the resulting ions and electrons are accelerated by the electric field across the chamber, causing a localised cascade of ionisation, resulting in a proportional charge on the wire. The particle trajectory can be determined by combining the measured pulses from all the wires. Furthermore the layers of straws are interleaved with polypropylene foils and fibres which acts as radiators. By making use of the fact that energy depositions due to transition radiation are typically four to five times higher for electrons than for minimum-ionising particles, such as pions, the TRT provides stand-alone electron and pion separation.

Calorimeters

The next line of subdetectors are the calorimeters of figure 3.7, which measure the energy of both charged and neutral particles. To determine the original energy of a particle, its energy is absorbed through high-density metal and the resulting shower shape is periodically sampled. Around the inner detector is first an electromagnetic (EM) calorimeter, which is ideally suited for precision measurements of electrons and photons. The more outer hadronic calorimeter has a coarser granularity and is designed to detect particles that pass through the EM calorimeter, which are predominantly hadrons that interact through the strong nuclear force.

The EM calorimeter has a barrel part in the pseudo–rapidity region $|\eta| < 1.475$ and two end–cap components (EMEC) extending the region to $1.375 < |\eta| < 3.2$, which all have their own cryostats. The barrel has two identical parts, separated by a small gap of 4 mm in the middle. Each end–cap has an inner and outer coaxial wheel, covering the $1.375 < |\eta| < 2.5$ and $2.5 < |\eta| < 3.2$ region respectively. It is a liquid argon based calorimeter with accordion–shaped kapton electrodes and lead absorber plates. The accordion geometry provides complete ϕ symmetry and coverage around the beam axis, which is essential to perform a good E_T^{miss} measurement. To distinguish between electrons and photons upstream of the calorimeter a presampler detector is installed in the $|\eta| < 1.8$ region.

The hadronic calorimeter has several components. Firstly, there is the so–called tile calorimeter which is located directly behind the EM calorimeter. It uses steel as the absorber and scintillating tiles as the active material. It consists of both a barrel and extended barrel part, covering the $|\eta| < 1.0$ and $0.8 < |\eta| < 1.7$ respectively, and extends radially from 2.28 to 4.25 meters.

Secondly, there are two hadronic end–cap calorimeters (HEC), which both consists of two independent wheels, made out of copper plates and liquid argon. They are located next to EMECs, with which they share the liquid argon cryostats.

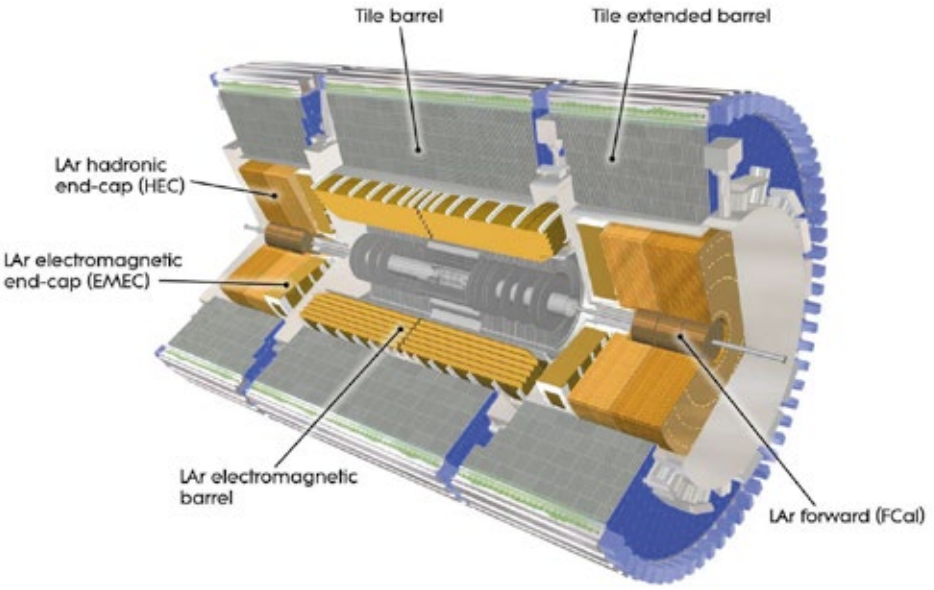

Fig. 3.7 · Image displaying the ATLAS calorimeter system. Taken from [57].

The HEC covers $1.5 < |\eta| < 3.2$ pseudo–rapidity regions, and extends radially from 0.475 to 2.03 meters, apart from the region shared with the forward calorimeter where the inner radius becomes 0.372 meters.

Thirdly, there is a forward calorimeter (FCal) on each side, integrated into the end–cap cryostats. Because they are located at high pseudo–rapidity regions, the FCal design is optimised to measure high particle fluxes. Therefore a scheme with very small liquid-argon gaps as the sensitive medium is employed, which are placed in tubes oriented parallel to the beam pipe. The first module of the FCal is optimised for electromagnetic interactions and uses copper as the absorber, while the other two are designed for hadronic interactions and are made out tungsten.

Muon system

The ATLAS muon spectrometer and its chambers are shown in figure 3.8. The traversing muons are deflected by large superconducting air-core toroid magnets which provide a field which is predominantly orthogonal to the muon trajectories. The bending is done with the use of a large barrel toroid in the $|\eta| < 1.4$ region, by two smaller end-cap magnets for $1.6 < |\eta| < 2.7$, and by a combination of both in the $1.4 < |\eta| < 1.62$ transition region. The bending power is 1.5 to 5.5 Tm and 1 to 7.5 Tm in the barrel and the end–cap region respectively, and somewhat lower in the transition region.

The tracks are measured by muon chambers, which are positioned in three cylindrical layers in the barrel region around the beam, and three perpendicular

planes to the beam in the transition and end–cap region. Monitored Drift Tubes (MDT's) provide the track measurement over most of the $|\eta|$ range, while at larger pseudo–rapidities of $2 < |\eta| < 2.7$ Cathode Strip Chambers (CSC's) with higher granularity are used to withstand the larger particle flux.

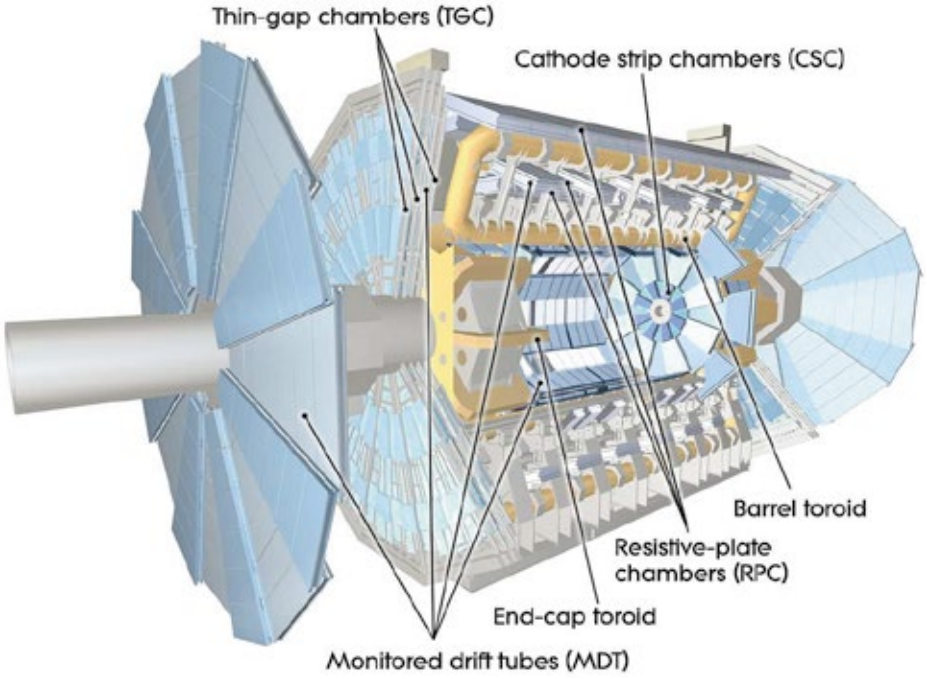

Fig. 3.8 · Computer generated image displaying the ATLAS muon system. Taken from [57].

The muon trigger system covers the pseudo–rapidity range $|\eta| < 2.4$ with the use of Resistive Plate Chambers (RPC's) and Thin Gap Chambers (TGC's) in the barrel and end–cap region respectively. It provides bunch-crossing identification, well–defined p_T thresholds and measures muons flying at small angles to the beam–pipe.

Trigger

The ATLAS trigger system consists three subsequent levels: level–1, level–2 and event filter. The first level uses hardware to make a decision within $2.5\,\mu$s based on the detector information, which reduces the rate to roughly 75 kHz. As input information it takes the calorimeters and the trigger chambers of the muon spectrometer. It saves the event if it is likely to contain a high p_T electron, muon or photon or is characterised by a large total transverse energy. The two higher levels access more detector information for a final rate of up to 400 Hz with an event size of approximately 1.6 Mb.

3.4 Data taking

The analyses described in this thesis make use of the proton-proton collisions recorded by ATLAS in 2012. At the start–up of the LHC, during power tests of the dipole circuit, a fault occurred in the electrical bus connection in the region between a dipole and a quadrupole, which caused mechanical damage and the release of helium into the tunnel [65]. As a precaution it was then decided to increase the centre–of–mass energy over the course of several years. The run conditions compared to its design values are shown in table 3.1.

The collisions with a center-of-mass energy of $\sqrt{s} = 8$ TeV were recorded between April 4$^{\text{th}}$ and December 6$^{\text{th}}$. Figure 3.9 shows how the integrated luminosity accumulated during the year, totalling a recorded luminosity of $\mathcal{L} = 20.3\,\text{fb}^{-1}$ suitable for physics. Due do the high instantaneous luminosity, on average there were 20.7 interactions per crossing. The luminosity-weighted distribution of this pile–up can be seen in figure 3.9.

The various sub-detectors have been performing well, as can be seen in table 3.2, totalling a recordering effiency of 95.5 % .

	2012	design
center-of-mass energy [TeV]	8	14
delivered integrated luminosity [fb^{-1}]	23.25	80–120
number of bunches	1380	2808
bunch spacing [ns]	50	25
peak instantaneous luminosity [$\text{cm}^{-2}\text{s}^{-1}$]	7.73×10^{33}	10^{34}
average pile–up	20.7	19.2

Table 3.1 · The LHC running conditions in 2012 compared to its design values. Taken from [66].

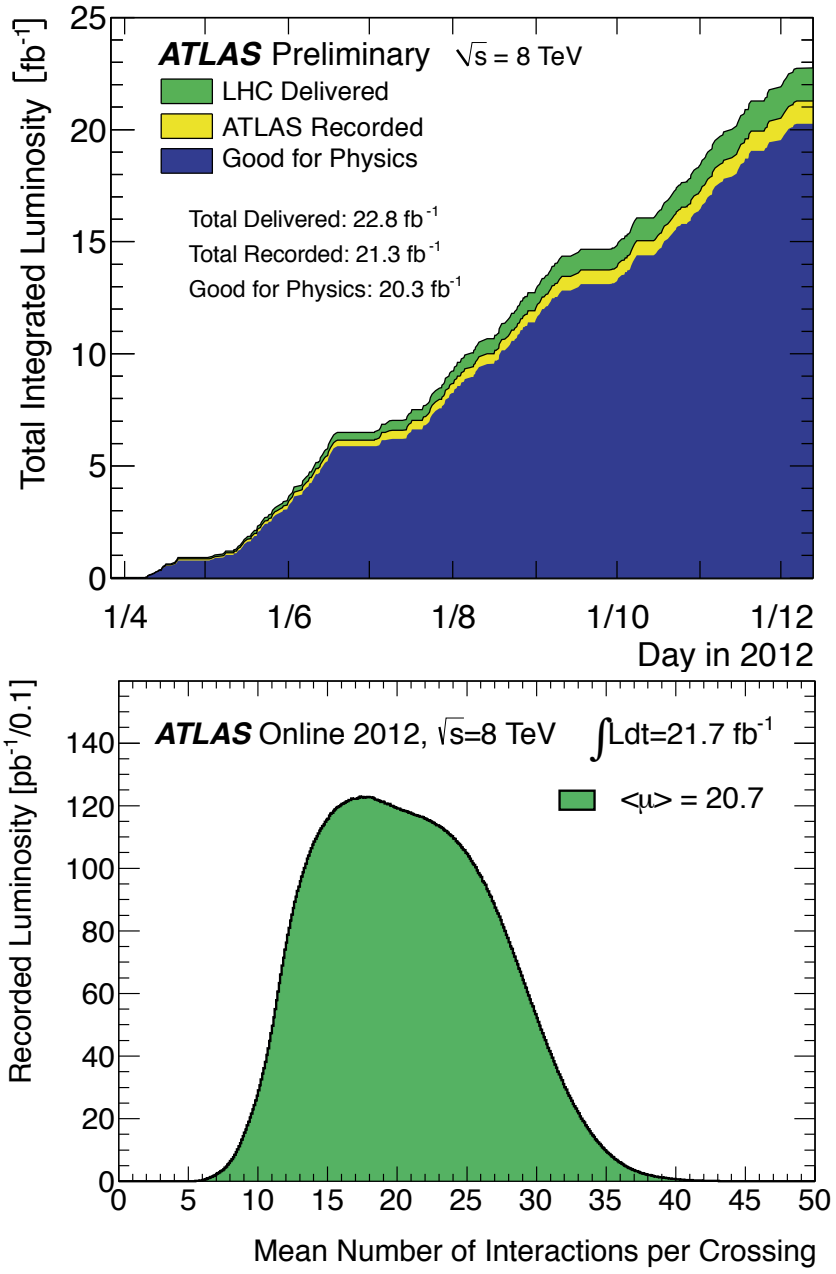

Fig. 3.9 · The top plot shows the cumulative luminosity versus time delivered by the LHC, recorded by ATLAS, and certified to be good quality data during stable beams in 2012. The bottom plot shows the luminosity-weighted distribution of the mean number of interactions per crossing for 2012. Taken from [67]

Inner Tracker			Calorimeters	
pixel	SCT	TRT	LAR	Tile
99.9	99.1	99.8	99.1	99.6

Muon Spectrometer				Magnets		
MDT	RPC	CSC	TGC	Solenoid	Toroid	All Systems
99.6	99.8	100.0	99.6	99.8	99.5	95.5

Table 3.2 · Luminosity weighted relative detector uptime and good quality data delivery in percentage, corresponding to $\mathcal{L} = 21.3\,\text{fb}^{-1}$ of recorded data. Taken from [66].

Conclusion

Proton collisions with a center-of-mass energy of $\sqrt{s} = 8$ TeV have been recorded by the ATLAS experiment at the Large Hadron Collider. The 2012 dataset is used for the $Z \to l\tau$ analysis of this thesis, which totals a recorded luminosity of $\mathcal{L} = 20.3 fb^{-1}$ after passing quality criteria.

chapter four

Particle and event reconstruction

The reconstructed particles that are used for the analysis described in the next chapter are identified by the signatures that they leave in the detector. Muons are reconstructed using tracks from both the muon spectrometer and inner detector, while electrons are identified by maching a track from the inner detector to an energy deposit in the calorimeter. Three-dimensional clusters of calorimeter cells form the input for the jet reconstruction, which is done using the anti–k_t algorithm. These reconstructed jets are the input for identification of hadronically decaying taus, for which the main challenge is to distinguish them from hadrons produced from the fragmentation of quark and gluon jets. Finally the missing transverse momentum is computed from the combination of all the reconstructed physics objects and the remaining energy deposits.

The above mentioned physics objects are all utilised to reconstruct the invariant mass of the Z boson of the LFV $Z \to l\tau$ decays. A modified version of the Missing Mass Calculator is used to calculate this invariant mass, which will be used as a hypothesis test in the subsequent chapters. There are several Standard Model processes after the event reconstruction that will act as a background in the search for $Z \to l\tau$ decays, namely $Z \to \tau\tau$, $t/t\bar{t}$, $W + jets$, $Z/VV \to ll$, $H \to \tau\tau$ and QCD multi-jets and are modelled by a combination of Monte Carlo simulation and data–driven methods.

4.1 Muon reconstruction

The ATLAS detector can detect and measure muons both in the inner dectector and the dedicated muon spectrometer. According to information recorded by the detector systems, muons are classified in the following reconstruction types:

Combined muons (CB) are the main type of reconstructed muons and are formed when a track from the muon spectometer and the inner detector are succesfully matched and their information combined.

Stand-alone muons (SA) are reconstructed using only the information from the muon spectrometer. Stand-alone muons make it possible to extend the coverage to an additional $2.4 < |\eta| < 2.7$ range which is outside of the scope of the inner detector.

Segment-tagged muons (ST) are reconstructed when a track in the inner detector is extrapolated to the muon spectrometer, and in doing so matches with at least one segment in the monitored drift tube or cathode strip chambers. This category can be used to incorporated to muons with a low p_T or that traverse regions in the muon spectrometer with reduced acceptance.

Calorimeter-tagged muons (CaloTag) are reconstructed when a track in the inner detector can be matched with an calorimeter energy deposit. It has the lowest purity of all categories, but it allows to recover the efficiency in the $|\eta| < 0.1$ region.

The muons are reconstructed with two different independent algorithms, called Chain 1 and 2. Chain 1 uses the track parameters and their corresponding covariance matrices to combine the information from the inner detector and the muon spectrometer. Chain 2 achieves this by using all the registered hits and doing a refit of the track. Figure 4.1 shows the reconstruction efficiency measured using $Z \to \mu\mu$ events for the different categories and reconstruction algorithms. The combination of all the muon reconstruction types gives a uniform muon reconstruction efficiency of about 99 % over full phase space and exhibits a percent level agreement between observed and simulated data.

For the search in this thesis the chain 2 algorithm is used in combination with muons identified as loose. This definition includes both combined and segment tagged muons. Additional muon quality criteria from the muon working group are applied, such as inner detector hit requirements, to achieve a precise measurement of the muon momentum and to reduce the misidentification rate.

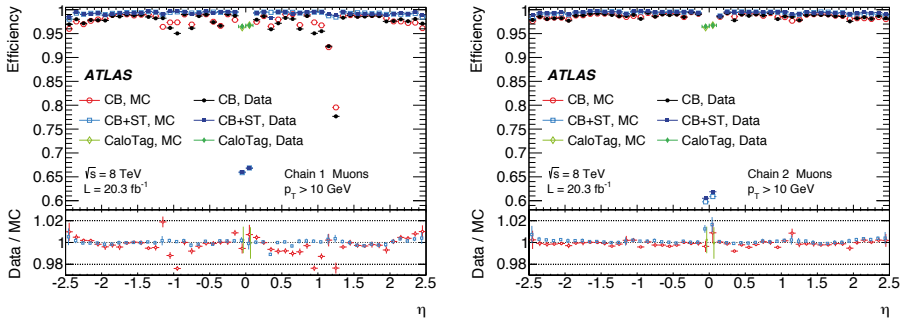

Fig. 4.1 · The reconstruction efficiency as a function of η for muons with $p_T > 10$ GeV for the Chain 1 (left) and Chain 2 (right) algorithms. Calorimeter-tagged muons are only shown for the $|\eta| < 0.1$ region where there is a gap in the muon spectrometer for support structures. The error bars on the efficiency represents statistical error, for the ratio the systematic uncertainty is included as well. The dip on the η distribution around 0 is caused by a gap in detector that is used for cabling. The dip around $+1$ is caused chambers that were not installed yet. Taken from [68].

4.2 Electron reconstruction

Tracks of charged particles in the inner detector that are matched to an energy deposit in the electromagnetic calorimeter are the seed for the electron identification algorithm [69]. Because of the acceptance of the inner detector, electrons are only measured in the angle $|\eta| < 2.49$. The electromagnetic clusters are reconstructed using a sliding-window instead of the topological algorithm that is used for jets. The sliding-window algorithm is based on summing cells within a fixed-size rectangular window; the position of the window is adjusted so that its contained transverse energy is a local maximum. It is an efficient tool for precisely reconstructing electromagnetic showers and allows for a very precise cluster energy calibration, but has less noise suppresion that the topological algorithm.

To distinguish real electrons from backgrounds such as hadronic jets a number sequential cuts on discriminating variables that are used. Among the 21 used variables are the number of hits in the pixel detector, the ratio of the energy deposited in the electromagnetic and hadronic calorimeter, and the shower width. Four working points are created, namely loose, medium, tight and multilepton, depending on the desired signal efficiency and background rejection of a given analysis.

Using a tag-and-probe method with $Z \rightarrow ee$ events, the reconstruction and identification efficiency is determined and shown in figure 4.2. Depending on the E_T, the reconstruction effiency is expected to be around 85 % for the medium working point used for the analysis of this thesis. Candidates found in the transition region between the end–cap and barrel calorimeters ($1.37 < |\eta| < 1.52$) are not considered. The total uncertainties on the identification efficiency measurements are around 1-2% for electrons with a transvere energy above 25 GeV.

4.3 Jet Reconstruction

Jets are collimated bunches of stable hadrons, produced by quark and gluons that have undergone fragmentation and hadronisation. Jets are reconstructed by first clustering energy deposits into so-called "TopoClusters" [70]. This topological algorithm starts with a seed cell and iteratively adds to the cluster the neighbor of a cell already in the cluster, provided that the energy in the new cell is above a threshold defined as a function of the expected noise. The produced three-dimensional clusters of the calorimeter cells form the input for the jet reconstruction algorithm. Through the years several methods have been developed to identify the jets produced by hadronic collisions. At ATLAS a sequential recombination algorithm called anti–k_t is employed, using a distance parameter of $R = 0.4$ [71]. It introduces a distance d_{ij} between clusters i and j, based on their tranverse momentum p_T and angular separation ΔR_{ij} as

$$d_{ij} = \min\left(\frac{1}{p_{Ti}^2}, \frac{1}{p_{Tj}^2}\right)\frac{{\Delta R_{ij}}^2}{R^2} \tag{4.1}$$

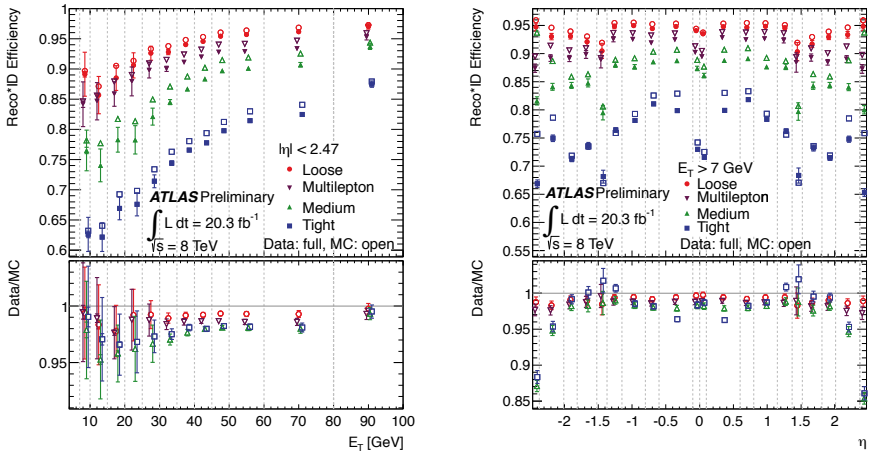

Fig. 4.2 · Measured combined reconstruction and identification efficiency for electrons as a function of E_T (left) and η (right) for the loose, multilepton, medium and tight selections. The lower panel shows the data to Monte Carlo agreement. The measured efficiency ratios are applied as correction or scale factors in analyses at ATLAS. The inner error bars quantify the statistical uncertainties and the outer errors bars with the systematic uncertainties included. Taken from [69].

and the distance between any cluster i and the proton beam direction B as

$$d_{iB} = \frac{1}{p_{Ti}^2} \tag{4.2}$$

The algorithm proceeds by calculating all possible distances. If the smallest value is given by d_{ij}, the four-momenta of the clusters i and j are combined, and all the distances are recalculated. If the smallest value is d_{iB}, cluster i is identified as a jet, and removed from the list of clusters that are iterated over. This process is repeated until all clusters are combined into jets. This algorithm exhibits the desirable characteristic that the jet shapes are resilient with respect to soft radiation, yet flexible with respect to hard radiation.

In the case of an event with a few well-separated hard particles and many soft ones, the distance between soft particles will be much larger. Consequently soft particles will cluster with hard ones before they cluster among themselves. If a hard particle has no hard neighbours within $\Delta R = 0.8$, then it will simply accumulate all the soft particles within a circle of radius 0.4, resulting in a perfectly conical jet. If another hard particle is present such that $0.4 < \Delta R < 0.8$ then there will be two hard jets. In case one jet has a much higher p_T, this jet will be conical, while the other will miss the overlapping part. When the two jets have a similar transverse momentum, both cones will clipped. When the other hard particle is within $\Delta R < 0.4$, the two particles are merged within a single jet. This single jet

will also be conical, unless the two particles have a similar p_T in which case the shape can be more complex. An example of this behaviour can be seen in figure in 4.3.

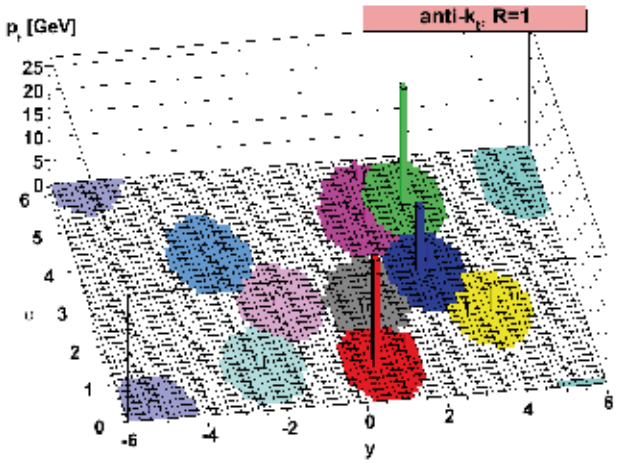

Fig. 4.3 · The result of a simulation using the anti–k_t with a distance parameter of 1. The variable y stands for pseudorapidity. Taken from [71].

Jets are calibrated to account for several effects, which are among others: energy lost in inactive areas of the detector, energy deposits below noise thresholds and multiple proton collisions in the same bunch. The topo-clusters are initially reconstructed at the electromagnetic scale. Then a second topo-cluster collection is built using the local cluster weighting (LCW) method, that improves the resolution by corrections that include a classification wether or not the clusters are electromagnetic or hadronic.

Only jets with $|\eta| < 4.5$ are selected for the analysis in this thesis. Furthermore a jet-vertex fraction (JVF) is used to reduce the number of jets in the event due to pile-up activity. The JVF is defined as the ratio between the sum of the transverse momentum of the tracks in the jet associated to the primary vertex and the sum of the transverse momentum of the tracks in the jet associated to any vertex in the event. Conventionally, $|\text{JFV}| = -1$ is assigned to jets without tracks. To suppress contributions from pileup, jets with $|\eta| > 2.4$ and $p_T < 50$ GeV are required to have $|\text{JFV}| > 0.50$.

The uncertainty on the central value of the reconstructed jet energy scale (JES) and the jet energy resolution (JER) at ATLAS are shown in figure 4.4. The jet energy scale is measured with an uncertainty below 4.5% and drops off with higher reconstructed transverse momentum, untill it reaches the $p_T > 800$ GeV region. The jet energy resolution is measured with an uncertainty below 3% at 20 GeV and less than 1% above 100 GeV for the jets reconstructed with the anti–k_t algorithm.

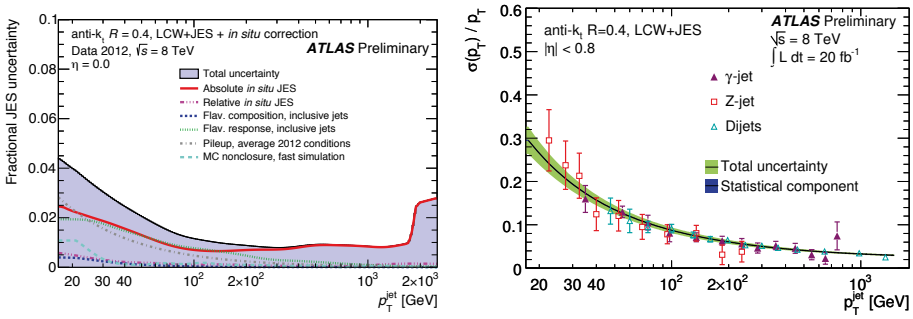

Fig. 4.4 · Total uncertainty on the jet energy scale (JES) of anti–k_t, $R = 0.4$ as a function of p_T using fast simulation is shown on the left. "Absolute in situ JES" refers to the uncertainty arising from V+jets and multi-jet measurements, whilst "Relative in situ JES" refers to the uncertainty arising from the dijet η-intercalibration. "MC non- closure, fast simulation" refers to the additional non-closure observed in fast simulation when comparing to full simulation. The uncertainty on the jet resolution (JER) as a function of p_T is shown on the right. Both figures are taken from [72].

The ability to identify jets containing b hadrons is important for treatment of the $t/t\bar{t}$ background. Several b–jet identifications algorithms have been developed. The IP3D algorithm is based on the impact parameter, SV1 exploits the secondary vertex and JetFitter uses a Kalman filter to exploit the topology of the b and c decays [73]. The MV1 tagger which is used for the search in the next chapter is a neural network that uses the most discriminating variables from both IP3D, SV1 and JetFitter [74]. Its efficiency to select the different jet flavours is evaluated on a sample of $t\bar{t}$ events is shown in figure 4.5. For the search described in the next chapter the MV1 output discriminant is chosen to be 70% efficient.

4.4 Tau lepton reconstruction

With a mass of 1776.86 ± 0.12 MeV, the tau is the heaviest particle of the lepton family [4]. Having a proper decay length of 87 μm, it decays too rapidly to be detected by the ATLAS detector. For this reason the identification happens through its decay products, which are summarized schematically in figure 4.6.

Because of its heavy mass, there are several decay modes which are kinematically allowed: $\tau^- \to \nu_\tau e^- \bar{\nu}_e$ $\tau^- \to \nu_\tau \mu^- \bar{\nu}_\mu$, $\tau^- \to \nu_\tau d\bar{u}$ and $\tau^- \to \nu_\tau s\bar{u}$, which are depicted in figure 4.7. Neglecting the fermion masses, the universality of the W couplings implies that these decay modes have equal amplitudes, apart from a factor $n_c|V_{ui}|^2$. Here n_c stands for the number of quark colours which is three, and for the elements of the CKM mixing matrix the approximation $|V_{ud}|^2 + |V_{us}|^2 \approx 1$

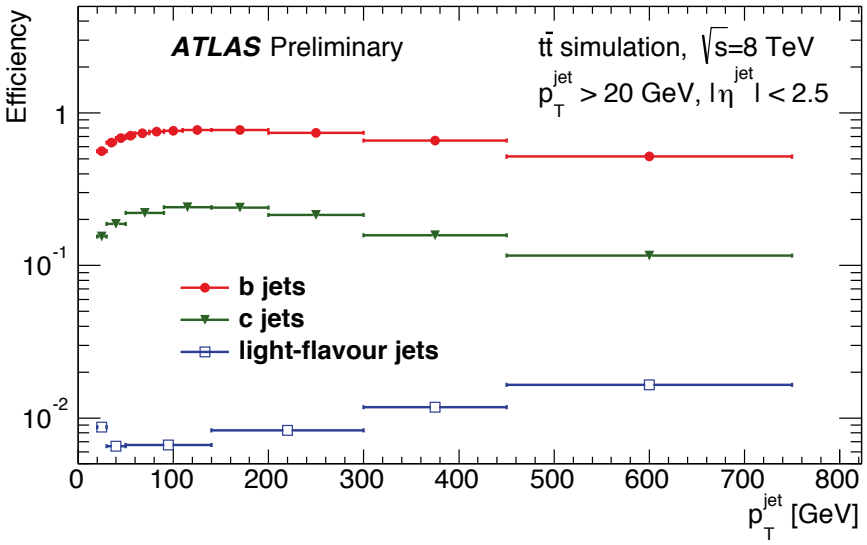

Fig. 4.5 · Efficiency of the MV1 tagger to select b, c, and light-flavour jets, as a function the p_T of the measured jet. The weight selection on the MV1 output discriminant is chosen to be 70% efficient for b–jets with $p_T > 20$ GeV and $|\eta| < 2.5$, as evaluated on a sample of simulated $t\bar{t}$ events. Taken from [74].

can be used. This gives the following lowest order approximation of the branching fraction:

$$\frac{\mathrm{Br}(\tau^- \to \nu_\tau + \mathrm{hadron})}{\mathrm{Br}(\tau^- \to \nu_\tau e^- \bar{\nu}_e,)} = \frac{\frac{1}{4} n_c |V_{ud}|^2 + \frac{1}{4} n_c |V_{us}|^2}{\frac{1}{4}} \approx 3 \tag{4.3}$$

So the measurement of the τ decay fractions provides strong evidence for the quark colours. The numerical differences with experimental results are mainly due to missing QCD corrections which amplify the hadronic decays by roughly 20 % [75]

The leptonic modes are difficult to be distinguished from muons or electrons that were produced directly at the proton collision and are therefore not used in the reconstruction. The search in this thesis utilises only hadronic tau decays that make up 65% of all the possible decay modes. In these cases the neutrino remains undetected apart from the total energy imbalance they produce, leaving only the hadrons to be used for reconstruction and identification. The produced hadrons consists of one or three charged pions $\pi^\pm$ in 72 and 22 % of all cases respectively. In the majority of the remaining decays charged kaons $K^\pm$ are present. Furthermore in 78% of the cases one or more neutral pions π^0 are produced. The hadrons that make up the visible decay products are referred to as τ_{had} in this thesis.

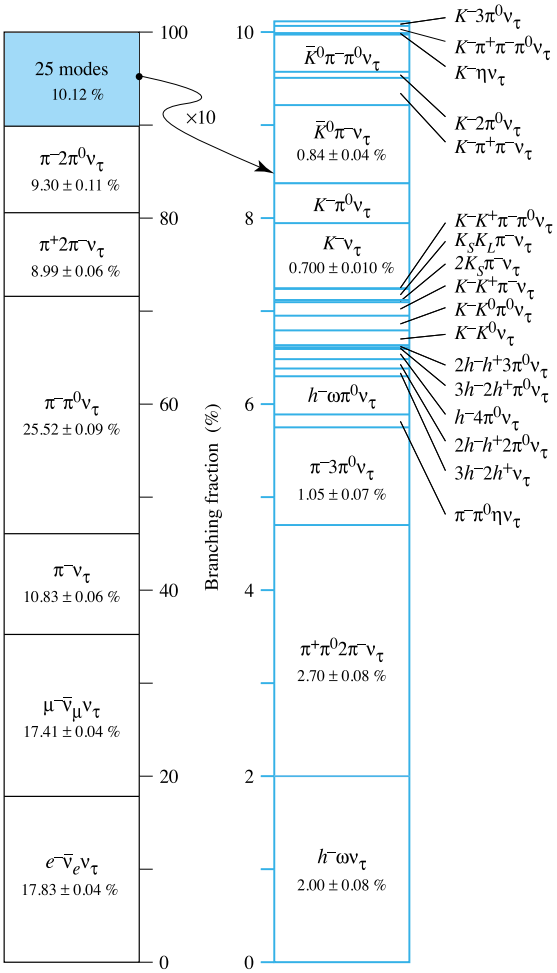

Fig. 4.6 · The various branching fractions of the τ-lepton. The leptonic modes account for 35% of the decays, the hadronic modes account for the remaining 65%. Taken from [4].

Jets that are reconstructed using the anti–k_t algorithm form the input for the τ_{had} reconstruction algorithm, under the requirement that they have a $p_T > 10$ GeV and $|\eta| < 2.5$. The main challenge of the identification of the τ_{had} is to distinguish them from hadrons produced from the fragmentation of quark and gluon jets. The ATLAS tau identification uses eleven discriminating variables, summarized in table 4.1, combined in Boosted Decision Trees (BDT) to reject these backgrounds [76].

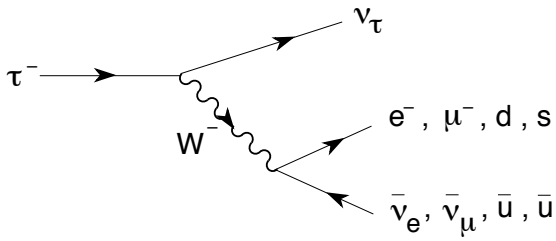

Fig. 4.7 · Feynman diagram for the decay of the τ-lepton. Taken from [75].

variable	definition
f_{cent}	central energy fraction
f_{track}	leading track momentum fraction
R_{track}	track radius
$S_{\text{leadtrack}}$	leading track IP significance
$N^{\text{iso}}_{\text{track}}$	number of tracks in the isolation region
ΔR_{max}	maximum ΔR between a track from the τ_{had} and its direction
$S_{\text{T}}^{\text{flight}}$	decay length of the secondary vertex in the transverse plane, divided by its estimated uncertainty
m_{track}	invariant mass of the tracks, assuming a pion mass for each track.
$m_{\pi^0+\text{track}}$	invariant mass of the tracks and π^0 mesons
N_{π^0}	number of reconstructed π^0 mesons
$p_T^{\pi^0+\text{track}}/p_T$	ratio of the transverse momentum using the track and π^0 information and the calorimeter-only measurement.

Table 4.1 · Discriminating variables used as input to the tau identification algorithm. More detailed information can be found in [76].

The distributions of two important variables, the central energy fraction (f_{cent}) and the leading track momentum fraction (R_{track}) are shown in figure 4.8. The narrow shower shape combined with a few collimated tracks characteristic of hadronic tau decays are useful in discriminating such decays from other signatures in the detector. The hadronic decay is classified into one and three tracks, for which separate BDT algorithms are trained. The background rejection and signal efficiency curve for these two algorithms are shown in figure 4.9. Three working points are defined namely tight, medium and loose. For the analysis described in chapter 5, the medium tau BDT was found to give the highest search sensitivity.

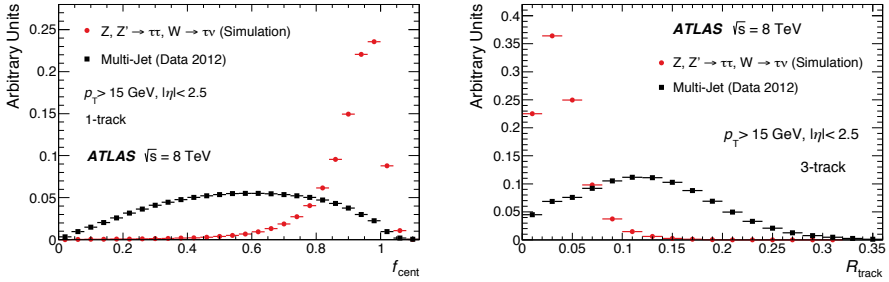

Fig. 4.8 · Distribution of f_{cent} on the left, and R_{track} on the right, which are used for the identification of hadronic tau leptons. Taken from [76].

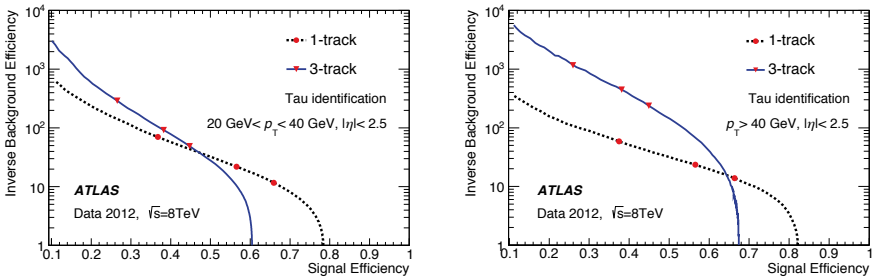

Fig. 4.9 · The inverse background efficiency versus signal efficiency of the tau identification for low and high p_T τ_{had} candidates, are shown on the left and right respectively. The signal events are a mixture of $Z \rightarrow \tau\tau$, W + jets and Z' processes, while the background consists of QCD multi-jet events. The red markers correspond to the tight, medium and loose working points. The reason the curves do not reach a signal effiency of 1, is that not all τ_{had} are identified as candidates. Which in turn is caused by the reconstruction efficiency and misassociation of the tracks used to reconstruct the τ_{had} . Taken from [76].

Electrons can also mimic 1-track τ_{had} decay and an additional dedicated BDT algorithm is used to discriminate against them. Among other distinct properties, the algorithm makes use of higher ratio of high- to low-threshold track hits in the TRT for electrons compared to pions, the distance between the track and the calorimeter direction and the ratio of energy deposited in the electromagnetic and hadronic calorimeter.

Muons are unlikely to deposit enough energy in the calorimeters to be reconstructed as τ_{had} candidates, because their relatively higher mass cause less Brems–strahlung to be produced compared to electrons. However, when a sufficiently energetic cluster in the calorimeter is associated with a muon, the muon track and the calorimeter cluster together may be misidentified as a τ_{had} . Muons which deposit a large amount of energy in the calorimeter and therefore fail muon spectrometer

reconstruction are characterized by a low electromagnetic energy fraction and a large ratio of track p_T to E_T deposited in the calorimeter. Low-momentum muons which stop in the calorimeter and overlap with calorimeter deposits of different origin are characterized by a large electromagnetic energy fraction and a low p_T to E_T ratio. The applied muon veto is a simple cut-based selection based on these two variables, which reduces the muon contamination to a negligible level.

4.5 Missing transverse energy

As the protons fly along the beam pipe in the $z-$direction, momentum conversation dictates that the total transverse momenta of the decay products in the the $x-y$ plane should be zero. Any deviation from this is quantified by the missing transverse energy E_T^{miss}, which is a measure of the particles that escape the detector unnoticed such as neutrinos. It is calculated by taking the negative vector sum of the transverse momenta of all the calibrated physics objects, e.g. the x and y component are given by

$$-E_{x/y}^{\text{miss}} = E_{x/y}^{e} + E_{x/y}^{\gamma} + E_{x/y}^{\tau_{\text{had}}} + E_{x/y}^{\text{jets}} + E_{x/y}^{\mu} + E_{x/y}^{\text{soft term}} \tag{4.4}$$

Energy deposits in the calorimeters and tracks are associated with the physics objects in the following order: electrons e, photons γ, the visible decay products of the tau τ_{had}, jets and muons μ. The remaining unassociated deposits and tracks are labeled as "sof term", and contain contributions from hard-scattering, the underlying event and pileup interactions. Calculating the soft term contribution is the most challenging part of the missing energy reconstruction, and several algorithms have been developed to reconstructed it at ATLAS [77]:

Calorimeter Soft Term (CST): is based on energy deposits in the calorimeter which are not associated to reconstructed particles and jets. Noise suppression is achieved by only using topocluster cells with the same LCW calibration as the jets. Low momentum particles that do not reach the calorimeter are added by using the inner detector tracks. Tracks reaching the calorimeter that are not associated to high momentum objects are also used.

Track Soft Term (TST): only uses unassociated tracks for the reconstruction of the soft term. Although this method is very pile-up independent it misses contributions from the soft neutral particles.

Track: reconstructs the complete E_T^{miss} based on tracks instead of deposits in the calorimeter. However for electrons it uses the measurement of the calorimeter instead of the track momentum, as it is more precise. The soft term for is defined to be identical to the TST by only using unassociated tracks as well.

Extrapolated Jet Area with Filter (EJAF): has a pile-up correction applied on the CST, based on the jet area [78].

Soft Term Vertex Fraction (STVF): is a different pile-up correction to the CST, utilising the information of the inner detector tracks. The correction factor α_{STVF} is calculated by taking the fraction of the total transverse momentum of the tracks originating from the primary vertex:

$$\alpha_{STVF} = \sum_{\text{tracks from PV}} p_T / \sum_{\text{all tracks}} p_T \tag{4.5}$$

Each event is then multiplied by this factor. Its mean value versus the number of reconstructed vertices N_{PV} is shown in figure 4.10.

The stability of the above algorithms against pileup is also shown in figure 4.10. As expected the Track and TST method shows the least dependency on N_{PV}, while the CST method without an pileup suppression technique applied the most. As can be seen the STFV outperforms the EJAF pileup suppression.

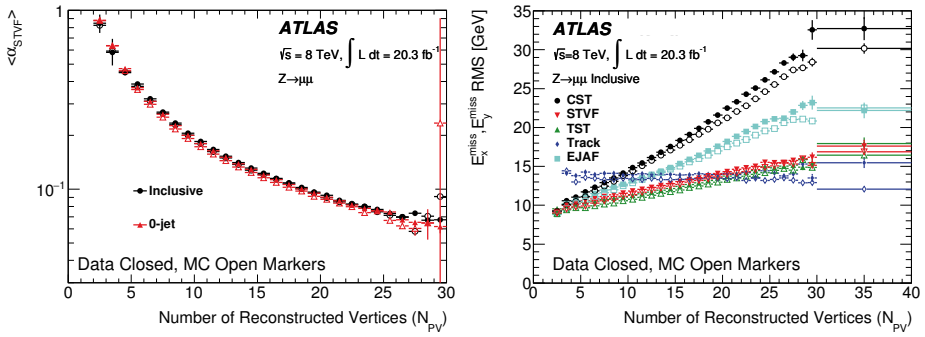

Fig. 4.10 · On the left the mean α_{STVF} event weight to suppress pileup effects is shown versus the number of reconstructed vertices for 0-jet (red) and inclusive (black) events for $Z \to \mu\mu$ events. On the right the resolution of the E_T^{miss} versus the number of constructed vertices $N_{\text{PV}}$is shown. The closed markers represent data while the open markers depict the result of Monte Carlo. Taken from [77].

The resolution and accuracy of the E_T^{miss} reconstruction for the different methods of reconstruction can be seen in figure 4.11. All algorithms except for the Track show similar performance, whereas the latter starts to degrade in resolution and accuracy because it does not include high–p_T neutral particles coming from jets. The resolution agreement between Monte Carlo and data is in excellent agreement for the Track method, however for the other algorithms there is a 20 % discrepancy for events with a total missing energy higher than 300 GeV. A positive bias is observed for events with $E_T^{\text{miss,truth}} < 40$ GeV. This is due to the finite resolution on the E_T^{miss} reconstruction and the fact that it is non-zero by definition.

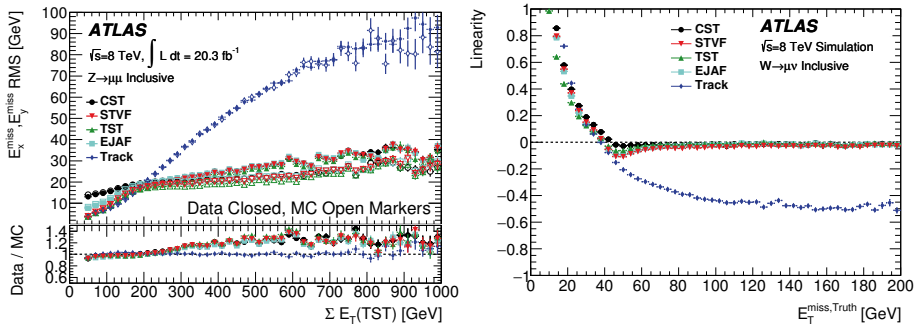

Fig. 4.11 · On the left the resolution of the different methods is shown versus the total reconstructed missing energy $\sum E_T^{\text{miss}}$ using $Z \to \mu\mu$ events. The total reconstructed missing energy is calculated with the TST method to suppress pileup effects. On the right the linearity versus the $E_T^{\text{miss,truth}}$ is shown using $W \to \mu\nu$ events. The linearity is defined as the ratio $E_T^{\text{miss}} - E_T^{\text{miss,truth}} / E_T^{\text{miss,truth}}$ and is expected to be zero if the E_T^{miss} is reconstructed at the correct scale. Taken from [77].

4.6 Event selection

The signatures of $Z \to l\tau$ decays are characterised by the presence of an energetic lepton originating directly from the boson decay and carrying roughly half of its energy, and the hadronic products of a τ-lepton. The analysis described in this thesis makes use of the proton collisions recorded at the ATLAS experiment in 2012. The measured data in both $Z \to l\tau$ channels is collected with single–lepton triggers: a single–muon trigger with a threshold of $p_T > 24$ GeV and a single–electron trigger with a threshold $E_T > 24$ GeV.

Muon candidates are reconstructed using the Chain 2 algorithm that combines information from the inner detector and the muon spectrometer. Muon quality criteria such as inner-detector hit requirements are applied to achieve a precise measurement of the muon momentum and to reduce the misidentification rate. Muons are required to have $p_T > 30$ GeV and to be within $|\eta| < 2.5$. The distance between the z-position of the point of closest approach of the muon inner-detector track to the beam-line and the z-coordinate of the primary vertex is required to be less than 1 cm. Here the primary vertex is chosen as the proton–proton collision vertex candidate with the highest sum of the squared transverse momenta of all associated tracks.

Electron candidates are required to have a transverse energy of $E_T > 30$ GeV, to be within the pseudorapidity range $|\eta| < 2.47$, and to satisfy the medium shower shape and track selection criteria discussed in section 4.2. Candidates found in the transition region between the end-cap and barrel calorimeters ($1.37 < |\eta| < 1.52$) are not considered.

Exactly one lepton (electron or muon) satisfying the above identification requirements is allowed. All lepton (electron or muon) candidates must satisfy ad-

ditional isolation criteria, based on tracking and calorimeter information, in order to suppress the background from misidentified jets or from semileptonic decays of charm and bottom hadrons. The calorimeter isolation variable $I(E_T, \Delta R)$ is defined as the sum of the total transverse energy in the calorimeter in a cone of size ΔR around the electron cluster or the muon track, divided by the E_T of the electron cluster or the p_T of the muon, respectively. The track-based isolation $I(p_T, \Delta R)$ is defined as the scalar sum of the transverse momenta of tracks within a cone of size ΔR around the electron or muon track, divided by the E_T of the electron cluster or the muon p_T, respectively. The isolation requirements used are optimised to reduce the contamination from non-prompt leptons.

Hadronically decaying τ-leptons are identified by means of the multivariate analysis technique discussed in section 4.4 based on boosted decision trees, which exploits information about ID tracks and clusters in the electromagnetic and hadronic calorimeters. The τ_{had} candidates are required to have $+1$ or -1 net charge in units of electron charge, and must be 1- or 3-track (1- or 3-prong) candidates. Events with exactly one τ_{had} candidate satisfying the medium identification criteria with $p_T > 30$ GeV and $|\eta| < 2.47$ are considered in the τ_{had} channels. Dedicated vetos to separate τ_{had} candidates from misidentified electrons and muons are applied. In addition to reduce the contamination due to backgrounds where a muon mimics a τ_{had} signature, events in which an identified muon with $p_T > 4$ GeV overlaps with an identified τ_{had} are also rejected.

Jets are required to be reconstructed in the range $|\eta| < 4.5$ and to have $p_{\text{T}} > 30$ GeV. To suppress jets from multiple proton–proton collisions in the same or nearby beam bunch crossings, tracking information is used for central soft jets with $|\eta| < 2.4$ and $p_T < 50$ GeV. Tracks originating from the primary vertex must contribute more than half of the jet p_{T} when summing the scalar p_{T} of all tracks in the jet; jets with no associated tracks are retained. In the pseudorapidity range $|\eta| < 2.5$, jets containing b-hadrons (b–jets) are selected using a the MV1 tagging algorithm with at a 70% working point.

When different objects selected according to the above criteria overlap with each other within $\Delta R < 0.2$, only one of them is considered for further analysis. The overlap is resolved by selecting muon, electron, τ_{had} and jet candidates in order of priority.

The missing transverse momentum is reconstructed using the STFV scaling procedure, as discussed in section 4.5, to achieve a more accurate reconstruction under high pile–up conditions. The reconstruction algorithm utilises the medium instead of the standard tight τ_{had} BDT, to be in line with the used τ_{had} selection.

The complete event selection is summarized in table 4.2.

object	selection
muon	Chain 2, combined + segment tagged
	$p_T > 30$ GeV
	$\|\eta\| < 2.5$
	ID quality criteria
	$I(E_{\mathrm{T}}, 0.2) < 0.06$
	$I(p_{\mathrm{T}}, 0.4) < 0.06$
electron	medium
	$p_T > 30$ GeV
	$\|\eta\| < 2.47$ and not in $1.37 < \|\eta\| < 2.47$
	ID quality criteria
	$I(E_{\mathrm{T}}, 0.2) < 0.06$
	$I(p_{\mathrm{T}}, 0.4) < 0.06$
τ_{had}	BDT medium
	$p_T > 30$ GeV
	$\|\eta\| < 2.47$
	electrical charge $= \pm 1$
	electron/muon veto
	1 or 3 tracks
jet	LCW, anti–k_t, $R = 0.4$
	$p_T > 30$ GeV
	$\|\eta\| < 4.5$
	$\|\mathrm{JFV}\| > 0.50$ for $\|\eta\| < 2.4$ and $p_T < 50$ GeV
	MV1 at 70% working point for b–jets veto
E_T^{miss}	STVF
	BDT medium for the identifaction for τ_{had}

Table 4.2 · The selection criteria that is used for the objects used for the for the LFV $Z \to l\tau$ analysis described in the chapter 5. The overlap is resolved by selecting muon, electron, τ_{had} and jet candidates in this order of priority.

4.7 Backgrounds

There are several Standard Model processes after the event selection of 4.6 that will act as a background in the search for $Z \to l\tau$ decays, namely $Z \to \tau\tau$, $t/t\bar{t}$, $W +$ jets, $Z/VV \to ll$, $H \to \tau\tau$ and QCD multi-jets. These backgrounds are identified after reconstruction as having the same $l\tau_{\text{had}}$ final state as the signal. As the misidentification rate of τ_{had} is much higher than for electron and muons, the reconstructed events can be broadly classified into three categories:

- events with a real lepton and τ_{had}
- events with a jet misidentified as a τ_{had}
- events with a lepton misidentified as a τ_{had}

Now the characterics, topologies and modeling of these backgrounds will be discussed, which are used for the event selection of the various signal and control regions.

$Z \to \tau\tau$

The largest source of Z boson production is shown in figure 4.12. It occurs when a quark of one proton and an antiquark of another proton annihilate, creating an on/off shell photon or Z boson which then decays into a pair of oppositely-charged leptons. Both $Z \to \tau\tau$, $Z \to \mu\mu$ and $Z \to ee$ are backgrounds to this analysis.

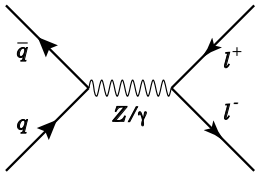

Fig. 4.12 · Example of lowest order Feynman diagram diagram for Z boson production and decay, taken from [79]

The $Z \to \tau\tau$ decay is the largest background due to its similarity with signal. As $Z \to l\tau$ decays it produces both a real lepton and a hadronically decaying tau, but two additional neutrino's are also produced by the other leptonically decaying tau. Although the produced lepton will be softer and the resulting reconstructed mass Z peak shifted towards lower values, the limitations in E_T^{miss} resolution do not make it possible to completely separate this background from the signal.

Because it is the largest contribution to the background, a good modelling is essential to this analysis. As discussed in section 4.4 the identification of hadronic tau decays is rather involved, so selecting a completely data–driven high statistics $Z \to \tau\tau$ sample is not feasible. However a hybrid method of real data and Monte Carlo simulation was devised. By selecting two isolated, energetic leptons with an invariant mass close to the Z resonance, a high statistics and pure sample of

$Z \to ll$ decays are selected. Apart from effects due to differences in lepton masses these two decays are are identical, including additional jets from the underlying event. Then these leptons are replaced by taus, of which the decay is modelled by Monte Carlo simulation. By using this embedded sample of which the details are further explained here [80], the variables related to the number of jets in the event, E_T^{miss}, pile-up and the underlying event are data driven and are not subjected to systematic uncertainties which improves the sensitivity of the analysis.

As this embedded sample is data driven it contains a raw number of events which are not directly related to its cross section. Therefore the normalisation is floated freely in the fit model which is described in more detail in section 5.4.

$Z/VV \to ll$

In addition to the $Z \to \mu\mu$ and $Z \to ee$ backgrounds of figure 4.12, the diboson decays $VV \to ll$ (where $V = W, Z$) decays produce a large amount of di-lepton events. Although no actual tau is produced in these decays apart from $VV \to \tau\tau$ the misidentification of the τ_{had} still produces a sizeable amount of background. There are two components to this misidentification, namely events where the reconstructed tau is a misidentified lepton ($l \to \tau_{\text{fake}}$) or a jet ($j \to \tau_{\text{fake}}$).

To obtain normalisation and shape corrections for the $Z \to ll$ background in case of $j \to \tau_{\text{fake}}$ a control region (ZllCR) is used, by selecting two oppositely charged leptons with an invariant mass in the range of $80 < m_{l^+l^-} < 100$ GeV, see section 5.2. Since this background is symmetric under charge a single correction factor is derived for both opposite sign (OS) and same sign (SS) events.

The predictions for the diboson and $Z \to \mu\mu\,(\mu \to \tau_{\text{fake}})$ are obtained from Monte Carlo simulation and normalised based on the production cross-section. For the $Z \to ee\,(e \to \tau_{\text{fake}})$ this contribution is much larger and floated freely in the fit to account for possible mis-modelling.

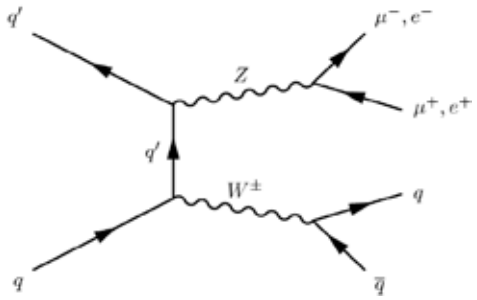

Fig. 4.13 · Example of a lowest order Feynman diagram for diboson production and decay, taken from [81]

W + jets

The W + jets is the second largest background and predominantly consists of a real high p_T lepton and a jet misidentified as a hadronically decaying tau. This lepton can

either be directly created in the case of $W \to l\nu$ or can originate from a tau decay from $W \to \tau\nu$, see also figure 4.14. Because the misidentified jet and the lepton do not originate from the decay of a single particle, the resulting reconstructed $M_{\tau l}^{\text{MMC}}$ distribution is very wide compared to $Z \to l\tau$ or $Z \to \tau\tau$ events, as can be seen in figure 5.8 for example.

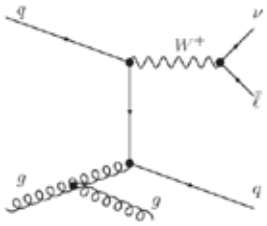

Fig. 4.14 · Example of lowest order Feynman diagram diagram for $W + 2$jets production and decay, taken from [82]

Because the τ_{had} identification algorithm overestimates the number of simulated $W +$ jets events with respect to collision data, a control region dominated with this background (WCR) is used to account for this effect, see section 5.2. The simulated $W +$ jets events are scaled by a factor such that the simulated and observed event yields are equal in the WCR. The misidentification differs for jets from quark and gluon hadronisation. Events with an oppositely charged lepton and hadronic tau have a bigger component of quark jets compared to those with same charge. Because of this two separate normalisation factors are obtained for opposite and same sign events.

$t/t\bar{t}$

The top quark is the heaviest known fundamental particle, first observed in 1995 at the Tevatron [83, 84]. Its dominant production channel is pair creation through the strong interaction depicted in figure 4.15. Top quarks are produced alone through the weak interaction shown in figure 4.16 of which the t-channel exchange of a virtual W boson is the dominant contribution. Both processes are distinct from other backgrounds by the presence of multiple high p_T jets including those from b quarks, which provides a convenient characteristic for designing a control region.

$H \to \tau\tau$

The $H \to \tau\tau$ decays appears as a small background. The measured signal strength was measured by ATLAS to be $\mu = 1.4 \pm 0.4$ [80]. As this falls within one standard deviation of the Standard Model prediction, the SM cross-section is used for the background prediction.

QCD multi-jets

Parton scattering is the most frequent occurring process at the LHC. Through the strong interaction two-parton scattering and hard gluon emission several energetic jets are produced, which is commonly called QCD multi-jets. It occurs as a back-

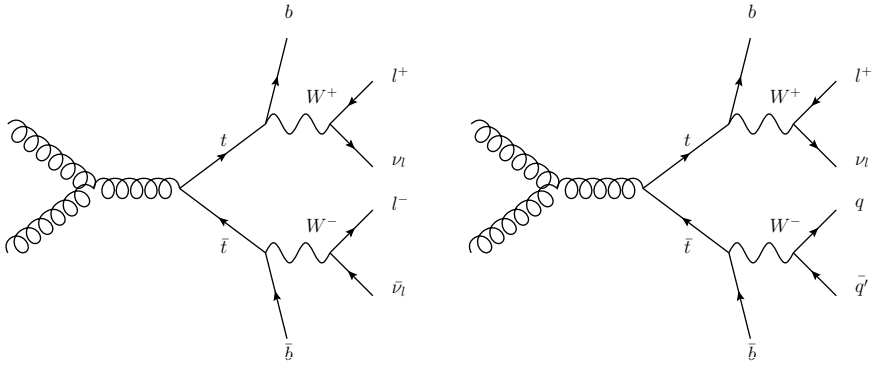

Fig. 4.15 · Example of lowest order Feynman diagrams for $t\bar{t}$ production, taken from [85]. On the left is the dilepton and on the right the single-lepton decay mode.

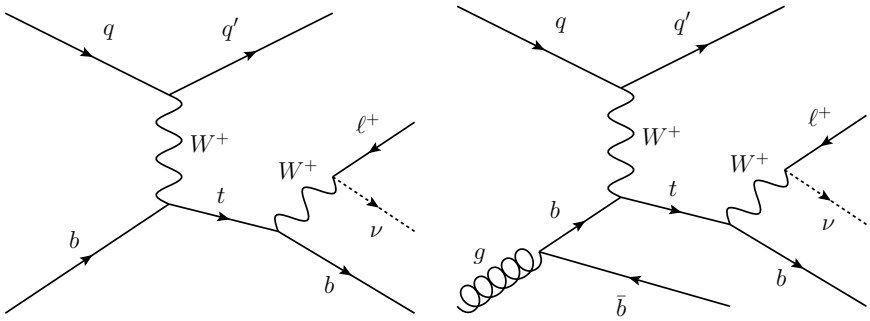

Fig. 4.16 · Example of lowest order Feynman diagrams for single top-quark production and decay, taken from [86]

ground when one jet fakes a lepton and another jet fakes a hadronically decaying tau. As this process is practically impossible to model by Monte Carlo simulation due to limited computing resources, it is obtained through a data-driven method as well, which is discussed in the section 5.2.

4.8 Monte Carlo simulation

To model these various backgrounds, several different Monte Carlo generators and samples are used. The detector simulation for all the Monte Carlo samples is performed with GEANT4 [87] and the reconstruction is made with the same software as is used for data. For the next to leading order generators POWHEG [88] and MC@NLO [89], the CT10 parton distribution function [90] is used, while for the leading order generators PYTHIA [91] and ALPGEN [92] the CTEQ6L1 parton distribution function [93] is used.

The Monte Carlo samples for W + jets are generated with ALPGEN [92]. ALPGEN calculates the hard scattering matrix elements by only including tree-level diagrams. To model the subsequent parton showering, hadronisation as well as the underlying event it is interfaced to either PYTHIA [91] or HERWIG combined with JIMMY [94, 95]. When comparing the event yields of the HERWIG and PYTHIA sample, it was found that even after normalisation to the data events in the WCR there are significant differences in the shape and normalisation of their predictions in the signal regions. Because the choice of event generators have this effect on the modelling of jet $\rightarrow \tau_{\text{had}}$ in the different regions of phase space a corresponding systematic uncertainty was introduced.

The $t\bar{t}$ samples are produced with the fully next to leading order calculator for the hard scattering MC@NLO [89]. The single top samples are simulated with the tree level matrix element generator ACERMC [96]. The subsequent parton showering and hadronisation is done with HERWIG with the underlying event simulated by JIMMY [95].

The Monte Carlo samples for $Z \rightarrow ll$ are also generated with ALPGEN and interfaced with PYTHIA 8. The diboson (WW, WZ, ZZ) samples are generated using HERWIG for WZ and ZZ processes and ALPGEN interfaced to HERWIG for the WW process. The loop-induced $gg \rightarrow WW$ processes are generated using gg2WW [97].

Lastly the $H \rightarrow \tau\tau$ decays are simulated by PYTHIA 8 as well [91].

4.9 Missing mass calculator

The invariant mass of the lepton flavour violation $Z \rightarrow l\tau$ decay is reconstructed using a modified version of the missing mass calculator [98].

It was originally developed for reconstructing the invariant mass of the $H \rightarrow \tau\tau$ system, which depending on whether each τ decays hadronically or leptonically, produces two, three or four neutrinos. Therefore the x, y, and z-components of the momentum carried away by the neutrino(s), and the invariant mass of the neutrinos in case of a leptonic decay are unkown. This results in 2 to 4 degrees of freedom, and it is therefore not possible to find one exact solution. However, not all solutions of this underconstrained system are equally likely. To find a better estimator of the invariant mass $m_{\tau\tau}$, an event likelihood $\mathcal{L}$ is constructed by,

$$\mathcal{L} = \mathcal{P}\left(\Delta R_1, p_{\tau 1}\right) \times \mathcal{P}\left(\Delta R_2, p_{\tau 2}\right) \times \mathcal{P}\left(\Delta E_x^{\text{miss}}\right) \times \mathcal{P}\left(\Delta E_y^{\text{miss}}\right). \tag{4.6}$$

The first two probability density functions describe the expected angular distance between the neutrinos and the visible decays products ΔR_x for a given momentum of the lepton $p_{\tau x}$, which are obtained from simulated $Z \rightarrow \tau\tau$ events. An example

for the three different decay modes of the τ are shown in figure 4.17. The latter two describe the resolution effects of the missing energy:

$$\mathcal{P}\left(\Delta E_{x/y}^{\text{miss}}\right) = \exp\left(\frac{-(\Delta E_{x/y}^{\text{miss}})^2}{2\sigma^2}\right), \tag{4.7}$$

where σ is the the resolution and $\Delta E_{x/y}^{\text{miss}}$ are the variations of the x and y component of the missing energy.

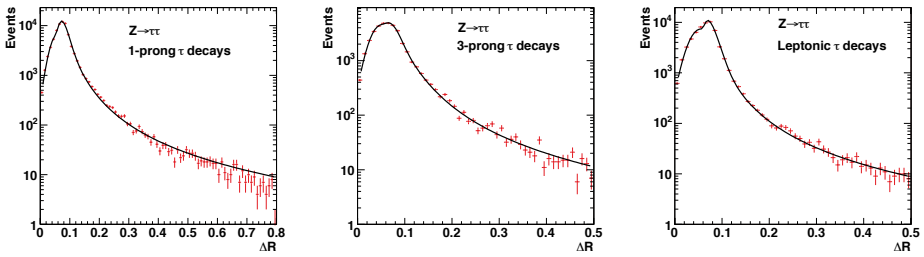

Fig. 4.17 · Example of the probability distribution functions $\mathcal{P}(\Delta R, p_\tau)$ for a particular value of the original τ lepton momentum. The probability density function are obtained by fitting a linear combination of Gaussian and Landau functions to the datapoints obtained from a simulated $Z \to \tau\tau$ sample. These functions are then used in the calculation of the likelihood $\mathcal{L}$ for three cases: 1-prong (left plot), 3-prong (middle plot), and leptonic (right plot) decays. These distributions depend only on the decay type and initial momentum of the τ lepton. Taken from [98].

In case of the LFV $Z \to l\tau$ decays, the kinematic equation can actually be solved exactly for the decay of the tau lepton. Assuming that the neutrinos from the τ decay are the only source of missing energy in the event, we can constrain the x and y component of the neutrino's momentum by the measured missing energy. A three sigma window around the measured $E_{x/y}^{\text{miss}}$ values is scanned to find the most likely invariant mass. The four momentum equation is given by

$$p_\tau = p_{\tau_{\text{had}}} + p_\nu \tag{4.8}$$

Squaring both sides and rearanging the terms gives:

$$\vec{p}_{\tau_{\text{had}}} \cdot \vec{p}_\nu - E_{\tau_{\text{had}}}|\vec{p}_\nu| + \frac{m_\tau^2 - m_{\tau_{\text{had}}}^2}{2} = 0 \tag{4.9}$$

Writing it out in terms of momentum components

$$p_\nu^z + \frac{2p_{\tau_{\text{had}}}^x p_\nu^x + 2p_{\tau_{\text{had}}}^y p_\nu^y + m_\tau^2 - m_{\tau_{\text{had}}}^2}{2p_{\tau_{\text{had}}}^z} = \frac{E_{\tau_{\text{had}}}}{p_{\tau_{\text{had}}}^z}\sqrt{(p_\nu^x)^2 + (p_\nu^y)^2 + (p_\nu^z)^2} \tag{4.10}$$

Rewriting the terms above reveals the reduced quadratic equation which describes the $z-$ component of the neutrinos momentum:

$$p_\nu^z + \alpha_1 = \alpha_2 \sqrt{\alpha_3 + (p_\nu^z)^2}, \tag{4.11}$$

$$(p_\nu^z)^2 + \frac{2\alpha_1}{1-\alpha_2^2} p_\nu^z + \frac{\alpha_1^2 - \alpha_2^2 \alpha_3}{1-\alpha_2^2} = 0. \tag{4.12}$$

Solving the above equation, gives rise to two possible solutions for the four momentum equation. Each solution is then weighted by the appropriate E_T^{miss} resolution probability and by the probability of a reconstructed tau decay topology $\mathcal{P}(\Delta R, p_\tau)$:

$$\mathcal{L} = \mathcal{P}(\Delta R, p_\tau) \times \mathcal{P}\left(\Delta E_x^{\text{miss}}\right) \times \mathcal{P}\left(\Delta E_y^{\text{miss}}\right). \tag{4.13}$$

The estimator for the invariant mass $M_{\tau l}^{\text{MMC}}$, is then defined as the solution with the highest probability. The result after the event selection described in the next section can be seen in figure 4.18.

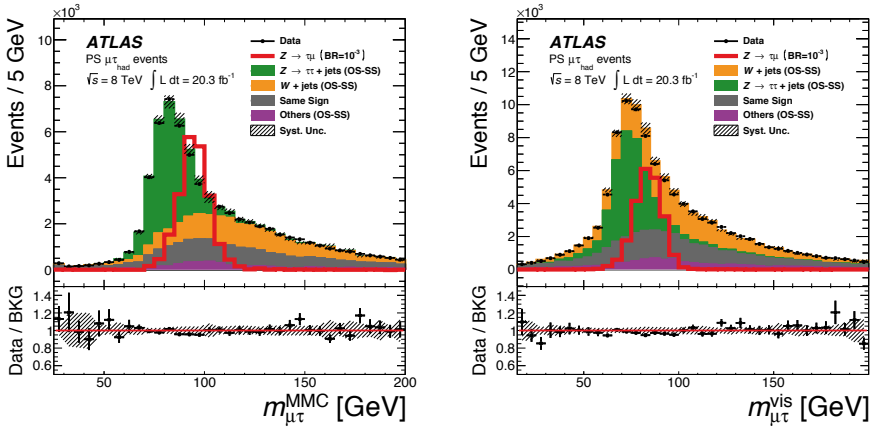

Fig. 4.18 · A comparision of the invariant mass $M_{\tau\mu}^{\text{MMC}}$reconstructed with the Missing Mass Calculator (on the left) and the invariant mass $M_{\tau\mu}^{\text{vis}}$ (on the right) using only the visible τ_{had} and μ decay products after the event selection described section 4.6. As can be seen the MMC method provides a substantially more accurate reconstruction of the mass and in addition reduces the background yield under the $Z \to \mu\tau$ peak. For the normalisations of the background distributions, their listed cross-sections are used with a rate and shape correction applied obtained from the control regions, see section 5.2. The systematic uncertainties are added in quadrature.

Conclusion

The algorithms that are used to identify and reconstruct the particles, jets and missing energy which are used in the search for LFV $Z \rightarrow l\tau$ decays at the ATLAS experiment are discussed. The event selection which forms the basis for the analysis of the next chapter is described. After this event selection there are several Standard Model processes that will mimic the LFV signatures, which are modelled by a combination of Monte Carlo methods and data driven techniques. Lastly, to reconstruct the invariant mass of the Z boson, a modified version of the Missing Mass Calculator is used. The Missing Mass Calculator method provides a substantially more accurate reconstruction of the Z mass compared to only its visible decay products, and in addition reduces the background contribution substantially.

chapter five

Measurement model

This chapter describes the model that will be used in the search for the charged lepton flavour violation (cLFV) in the $Z \to l\tau$ (with $l = e, \mu$) channel, by looking at tau leptons decaying hadronically. The characteristics and modelling of these decays are discussed in section 5.1.

Several Standard Model (SM) processes will contribute to the observed events after the event selection and reconstruction. To model the expected SM backgrounds, both Monte Carlo and data-driven techniques are utilised, which are discussed in section 5.2. Because processes where a jet fakes a hadronically decaying tau lepton are not well modelled by means of Monte Carlo simulation, dedicated control regions are used to correct these prediction.

Subsequently the event selection is optimised to create signal regions that are both sensitive to the cLFV Z decays while at the same time reduce the contamination from the SM processes. In these signal regions the background (SM) and signal (SM with $Z \to \tau l$) hypotheses are tested. The employed scheme is discussed in section 5.3 and was chosen to possess a large shape difference in the $M_{\tau l}^{MMC}$ distribution for the signal and background processes in addition to having a high statistical significance. This is done to have robustness when dealing with the different systematic uncertainties which alter these distributions.

The mass of the Z boson $M_{\tau l}^{MMC}$ is reconstructed using the Missing Mass Calculator package. The hypothesis test is chosen to be a binned likelihood fit of the distribution of $M_{\tau l}^{MMC}$, which is discussed in detail in section 5.4. The branching fractions of the $Z \to l\tau$ decays are extracted from the fit, by comparing the observed data to the sum of the expected backgrounds, while taking into account the various systematic uncertainties of section 5.5.

To avoid possible biasing, the search is performed as a blinded analysis. The invariant mass distributions are blinded in the mass window of $80 < M_{\tau l}^{MMC} < 115$ GeV of the signal regions. For reference, throughout this analysis a branching fraction of $Br(Z \to l\tau) = 10^{-5}$ is assumed. To make the kinematic distributions visible in the plots, their histograms are multiplied by a factor of hundred.

5.1 Signal modelling

In the researched $Z \to l\tau$ channels a neutral Z boson decays to a lepton l, either a muon, μ, or an electron, e, and a tau lepton, τ. The latter decays hadronically, to one or more hadrons, τ_{had}, and a tau neutrino, ν_τ. To model these decays,

lepton flavour violating signal samples are generated with Pythia 8.165 using the AU2MSTW2008LO generator tune. Due to a large number of theoretical models that could cause lepton flavour violation, a flat phase space decay of the Z boson is assumed. These signal samples contain 100000 events after an applied filter that requires at least one lepton with $p_T > 5$ GeV and $|\eta| < 2.8$ in the event, which results in a generator efficiency of 82.4 %. The decays of the τ are modelled with Pythia 8 as well. The signal events are characterised by the following key features, which are shown in figure 5.1:

- the presence of a high-p_T lepton, with the corresponding distribution peaking at $p_T(l) \sim M_{\tau l}^{\text{MMC}}/2$
- a τ_{had} roughly back-to-back this lepton l, the angular distance $\Delta R(l, \tau_{\text{had}})$ peaking around π rad
- the presence of only one tau neutrino ν_τ from hadronic τ-decays, which is almost collinear with τ_{had}
- a large transverse mass of the lepton l and the E_T^{miss} system, due to a large average $p_T(l)$ and a large $\Delta R(l, \nu_\tau)$ angle
- a small transverse mass of the τ_{had} and E_T^{miss} system, caused by the relatively soft p_T spectrum of the τ_{had} , together with a small angular separation $\Delta R(\nu_\tau, \tau_{\text{had}})$ with respect to the escaping neutrino

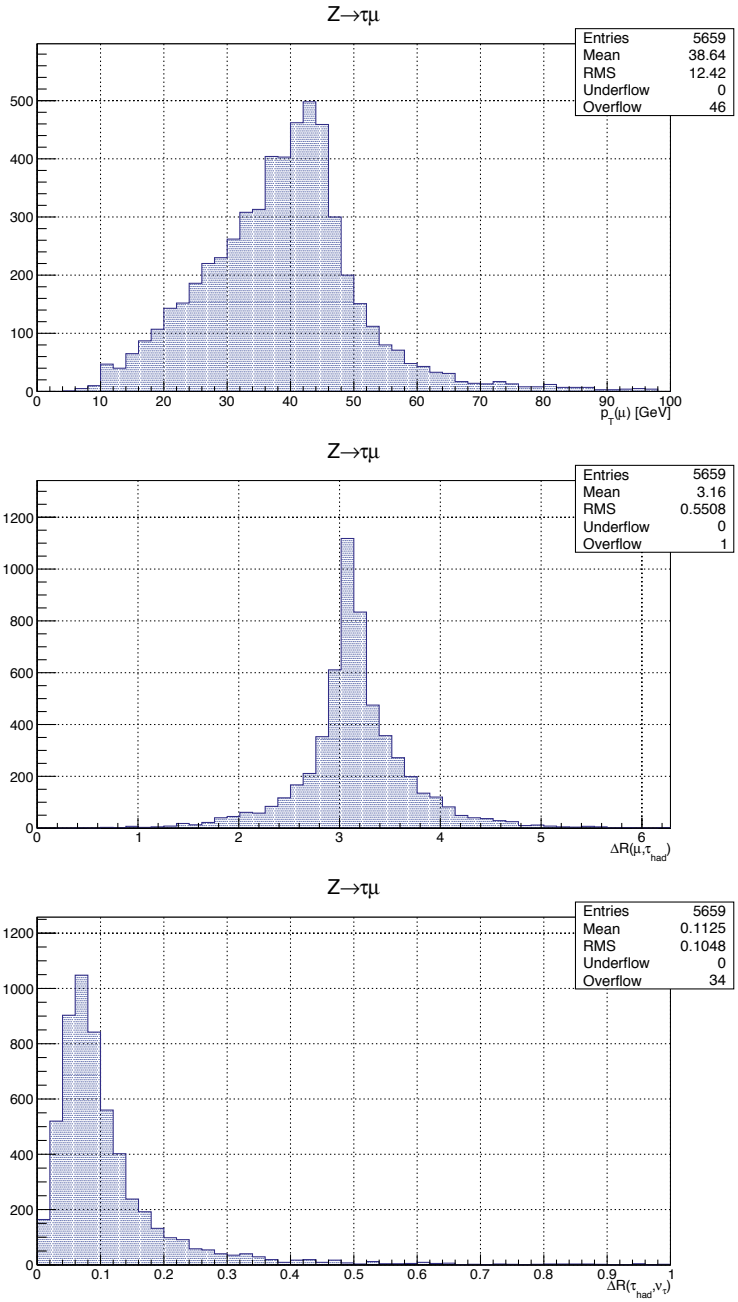

Fig. 5.1 · The kinematic properties of the lepton flavour violating $Z \rightarrow \mu\tau$ decays. From top to bottom: $p_T(\mu)$, $\Delta R(\mu, \tau_{\text{had}})$ and $\Delta R(\nu, \tau_{\text{had}})$ distributions are displayed at MC truth level before full reconstruction.

5.2 Standard Model estimation

It is known that processes where a jet fakes a τ_{had} are not well modelled by Monte Carlo simulation at ATLAS, and this effect has been accounted for in past publications [99, 100]. Therefore these contributions either need to be estimated by data driven techniques or Monte Carlo predictions need to be corrected from dedicated control regions. The background estimation method that is used relies on the following assumptions:

- The shape of the reconstructed invariant mass distribution $M_{\tau l}^{\text{MMC}}$ is the same for events with a opposite sign (OS) and same sign (SS) reconstructed muon and τ_{had} for the QCD multi-jet background in the signal regions.
- The scale factor $k = N(\text{data})/N(\text{MC})$ is the same for the processes in the signal and corresponding control regions for the electroweak backgrounds. They can be different for OS and SS events for certain background however, and need to be obtained separately in that case. The Monte Carlo predictions based on the luminosity and cross section are then multiplied by these k-factors in order to account for mis-modelling of $j \to \tau_{\text{fake}}$ rates and to reduce systematic uncertainties on their normalisation.

The prediction for the number of OS background events, $N_{\text{OS}}^{\text{bkg}}$, for each bin of the $M_{\tau l}^{\text{MMC}}$distribution is consequently given by the following formula:

$$N_{\text{OS}}^{\text{bkg}} = r_{\text{QCD}} \cdot N_{\text{SS}}^{\text{data}} + N_{\text{add-on}}^{Z\to\tau\tau} + N_{\text{add-on}}^{W+\text{jets}} + N_{\text{add-on}}^{t/t\bar{t}} + N_{\text{add-on}}^{VV\to ll} + N_{\text{add-on}}^{H\to\tau\tau} + N_{\text{add-on}}^{Z\to ll(l\to\tau_{\text{fake}})} + N_{\text{add-on}}^{Z\to ll(j\to\tau_{\text{fake}})}, \tag{5.1}$$

where the ratio $r_{\text{QCD}} = N_{\text{OS}}^{\text{QCD}}/N_{\text{SS}}^{\text{QCD}}$ accounts for the rate difference in QCD multi-jets when requiring OS or SS events, which is caused by their different flavour composition. The value of r_{QCD} is derived from a QCD multi-jet control region in data, as discussed in detail in [80]. Figure 5.2 shows the comparison of the visible and transverse mass in the control region for the $\mu\tau_{\text{had}}$ finalstate.

The rate difference is determined to be $r_{\text{QCD}} = 1.10 \pm 0.14$ for the $\mu\tau_{\text{had}}$, and $r_{\text{QCD}} = 1.00 \pm 0.13$ for the $e\tau_{\text{had}}$ final final state, both including systematic error. The term add-on in the above equation refers to a certain electroweak background contribution predicted by MC events in addition to those already included in $N_{\text{SS}}^{\text{data}}$. The individual add-on components are are given by:

- $N_{\text{add-on}}^{Z\to\tau\tau} = k_{Z\to\tau\tau} \cdot \left(N_{\text{OS}}^{Z\to\tau\tau} - r_{\text{QCD}} \cdot N_{\text{SS}}^{Z\to\tau\tau}\right)$. The $Z \to \tau\tau$ background consists of a real lepton and τ_{had} . The factor $k_{Z\to\tau\tau}$ is not a rate correction as in the case of the other backgrounds, but rather the normalisation for the embedded sample. For the extraction of the signal it is floated freely without constraints in the fit model, which is described in more detail in section 5.4. This background exhibits a strong charge correlation between the lepton and

the τ_{had} , e.g. the number of events with opposite sign charges is much larger then the number with same sign charges, $N_{\text{OS}} \gg N_{\text{SS}}$.

- $N_{\text{add-on}}^{W+\text{jets}} = k_{W+\text{jets}}^{\text{OS}} \cdot N_{\text{OS}}^{W+\text{jets}} - r_{\text{QCD}} \cdot k_{W+\text{jets}}^{\text{SS}} \cdot N_{\text{SS}}^{W+\text{jets}}$. Because the $W+$ jets background consists of a jet misidentified as a τ_{had}, a rate correction is applied. The quark and gluon composition differ for OS and SS events causing some charge asymmetry $N_{\text{OS}} > N_{\text{SS}}$. Therefore two separate corrections are obtained from a control region, namely $k_{W+\text{jets}}^{\text{OS}}$ and $k_{W+\text{jets}}^{\text{SS}}$.

- $N_{\text{add-on}}^{t/t\bar{t}} = k_{t/t\bar{t}}^{\text{OS}} \cdot N_{\text{OS}}^{t/t\bar{t}} - r_{\text{QCD}} \cdot k_{t/t\bar{t}}^{\text{SS}} \cdot N_{\text{SS}}^{t/t\bar{t}}$. For the $t/t\bar{t}$ background a separate OS and SS rate correction is obtained from its corresponding control region as well.

- $N_{\text{add-on}}^{VV\to ll} = k_{VV\to ll} \cdot \left(N_{\text{OS}}^{VV\to ll} - r_{\text{QCD}} \cdot N_{\text{SS}}^{VV\to ll}\right)$, with $k_{VV\to ll}$ assumed to be unity.

- $N_{\text{add-on}}^{H\to\tau\tau} = k_{H\to\tau\tau} \cdot \left(N_{\text{OS}}^{H\to\tau\tau} - r_{\text{QCD}} \cdot N_{\text{SS}}^{H\to\tau\tau}\right)$, with $k_{H\to\tau\tau}$ assumed to be unity.

- $N_{\text{add-on}}^{Z\to ll(l\to\tau_{\text{fake}})} = k_{Z\to ll(l\to\tau_{\text{fake}})} \cdot \left(N_{\text{OS}}^{Z\to ll(l\to\tau_{\text{fake}})} - r_{\text{QCD}} \cdot N_{\text{SS}}^{Z\to ll(l\to\tau_{\text{fake}})}\right)$. For the $\mu\tau_{\text{had}}$ final-state this component is rather small and $k_{Z\to\mu\mu(\mu\to\tau_{\text{fake}})}$ is assumed to be unity. Because an electron gets misidentified as a τ_{had} more often due to its energy deposition in the calorimeter, this component is much larger for the $e\tau_{\text{had}}$ final state. Therefore a rate correction $k_{Z\to ee(e\to\tau_{\text{fake}})}$ is obtained in this case, see 5.4 for more details.

- $N_{\text{add-on}}^{Z\to ll(j\to\tau_{\text{fake}})} = k_{Z\to ll(j\to\tau_{\text{fake}})} \cdot N_{\text{OS}}^{Z\to ll(j\to\tau_{\text{fake}})} (1 - r_{\text{QCD}})$, with $k_{Z\to ll(j\to\tau_{\text{fake}})}$ obtained from the ZllCR. As the number of OS and SS events are expected to be the same, only $N_{\text{OS}}^{Z\to ll(j\to\tau_{\text{fake}})}$ is used.

A consequence of the used background estimation technique is that some of the add-on components can be negative. This can happen in the case of statistical fluctuations, when a background has a very small difference between the number of OS and SS events. In such cases, the content of corresponding bins is set to the average statistical error of the distributions.

The corrections to the Monte Carlo prediction are obtained from dedicated control regions where that particular process dominates. The selection scheme conveniently makes use of the fact that the signal and the various background processes are differently distributed in $m_T(l, E_T^{\text{miss}})$ -$m_T(\tau_{\text{had}}, E_T^{\text{miss}})$ space, which is shown for the $\mu\tau_{\text{had}}$ final-state in figure 5.3. The definition of the control regions and the obtained values of all normalisation and MC-to-data scale factors are summarised in table 5.1.

These MC-to-data scale factors are applied to produce all the kinematic distributions in this chapter. As they are all obtained from their respective control

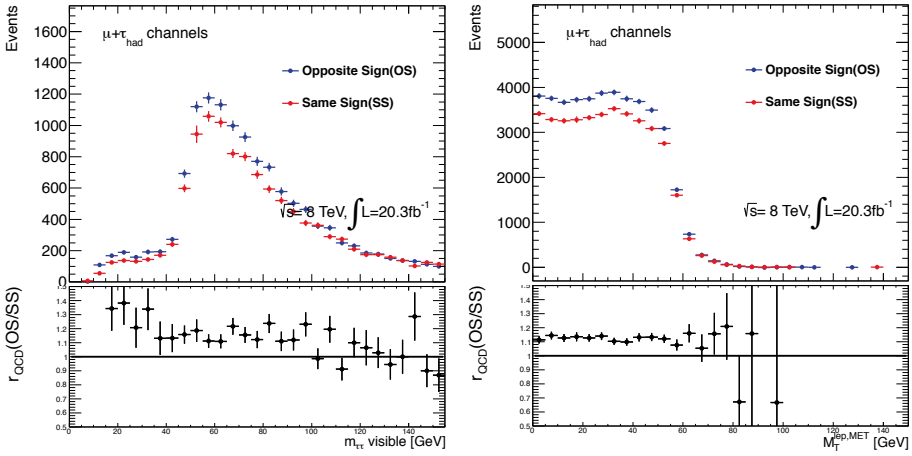

Fig. 5.2 · Comparison of the visible mass and $m_T(\mu, E_T^{\text{miss}})$ distributions for opposite sign (red) and same sign (blue) QCD multi-jet . The distributions are determined by substracting the electroweak backgrounds from observed data in QCD control regions for the $\mu\tau_{\text{had}}$ channel. From the event yield in the QCD control regions, the rate difference $r_{\text{QCD}} = N_{\text{OS}}^{\text{QCD}}/N_{\text{SS}}^{\text{QCD}}$ is determined. Taken from the support material of the ATLAS $H \to \tau\tau$ analysis [80]

region separately they are still subject to change when performing the likelihood minimisation on all the unblinded signal and control regions simultaneously, which is described in section 5.4. Therefore the applied scale factors should be interpreted as providing an initial normalisation value to the fit, the composition of the distributions are altered somewhat when extracting the final result in chapter 6 and are therefore labeled 'pre-fit'. The resulting pre-fit $M_{\tau l}^{\text{MMC}}$and other variables can be seen in figures 5.4, 5.5 and 5.6.

Two orthogonal signal regions, SR1 and SR2, are used to test the background (SM) and signal (SM with $Z \to \tau l$) hypotheses, as will be discussed in section 5.3. The normalisation of the embedding events for $Z \to \tau\tau$ are taken from the sideband of SR2, and can be seen in figure 5.9.

region	process	cuts	scale factor $\mu\tau_{\text{had}}$	scale factor $e\tau_{\text{had}}$
ZttCR	$Z \to \tau\tau$	$m_T(l, E_T^{\text{miss}}) < 30$ GeV $m_T(\tau_{\text{had}}, E_T^{\text{miss}}) < 45$ GeV $60 < M_{\tau l}^{\text{MMC}} < 85$ GeV no 2$^{\text{nd}}$ l MV1 b-jet veto $\Delta\eta(l, \tau_{\text{had}}) < 2$ $p_T(l) > 30$ GeV	$k = 0.487 \pm 0.009$	$k = 0.66 \pm 0.02$
WCR	$W +$ jets	$m_T(l, E_T^{\text{miss}}) > 60$ GeV $m_T(\tau_{\text{had}}, E_T^{\text{miss}}) > 40$ GeV $M_{\tau l}^{\text{MMC}} > 60$ GeV no 2$^{\text{nd}}$ l MV1 b-jet veto $\Delta\eta(l, \tau_{\text{had}}) < 2$ $p_T(l) > 30$ GeV	$k_{\text{OS}} = 0.79 \pm 0.02$ $k_{\text{SS}} = 0.87 \pm 0.06$	$k_{\text{OS}} = 0.80 \pm 0.03$ $k_{\text{SS}} = 1.14 \pm 0.07$
TCR	$t/t\bar{t}$	≥ 2 jets with $p_T > 30$ GeV ≥ 1 b-jet selected with MV1 $M_{\tau l}^{\text{MMC}} > 60$ GeV no 2$^{\text{nd}}$ l $\Delta\eta(l, \tau_{\text{had}}) < 2$ $p_T(l) > 30$ GeV	$k_{\text{OS}} = 0.93 \pm 0.03$ $k_{\text{SS}} = 1.23 \pm 0.1$	$k_{\text{OS}} = 0.96 \pm 0.03$ $k_{\text{SS}} = 1.44 \pm 0.12$
ZllCR	$Z \to ll$ ($j \to \tau_{\text{had}}$)	2 opposite charged isolated l $M_{\tau l}^{\text{MMC}} > 60$ GeV $60 < m_{l^+l^-} < 100$ GeV	$k = 0.782 \pm 0.008$	$k = 0.71 \pm 0.02$

Table 5.1 · The definitions of the various regions and the extracted scale factors for opposite charge (OS) and same charge (SS) requirement. For $Z \to \tau\tau$ an embedding sample is used, so the listed scale factor is actually a normalisation and should not be interpreted as a rate correction. The term l stands for either a muon or an electron.

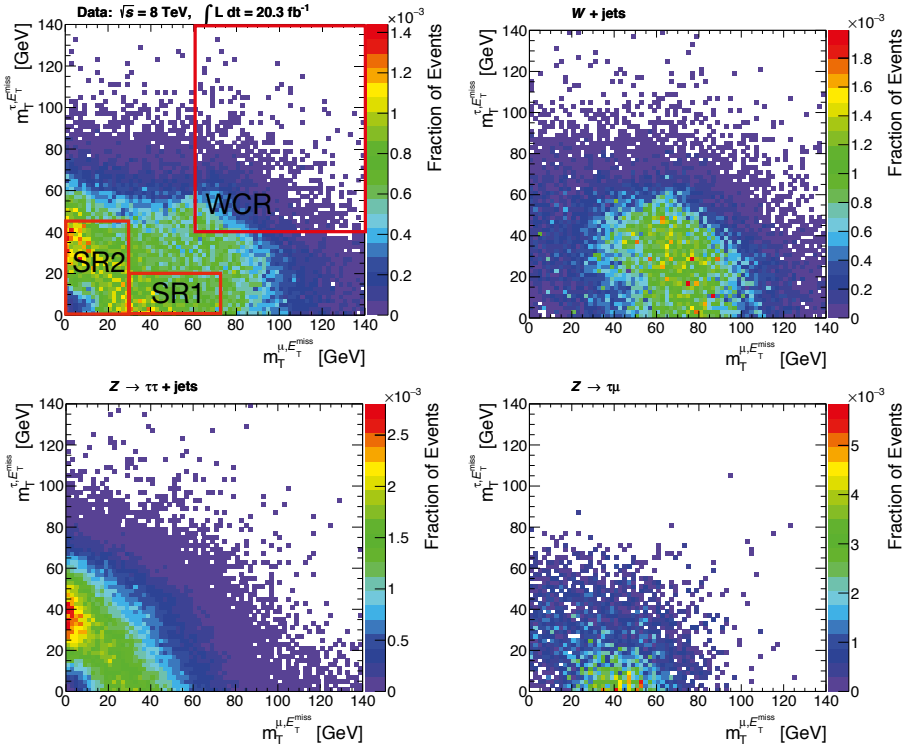

Fig. 5.3 · The distribution of events in $m_T(\mu, E_T^{\text{miss}})$ -$m_T(\tau_{\text{had}}, E_T^{\text{miss}})$ space for signal and the various background processes in the $\mu\tau_{\text{had}}$. From top to bottom and left to right: the full 2012 ATLAS dataset corresponding to 20.3 fb^{-1}, W + jets , $Z \to \tau\tau$ and $Z \to \mu\tau$.

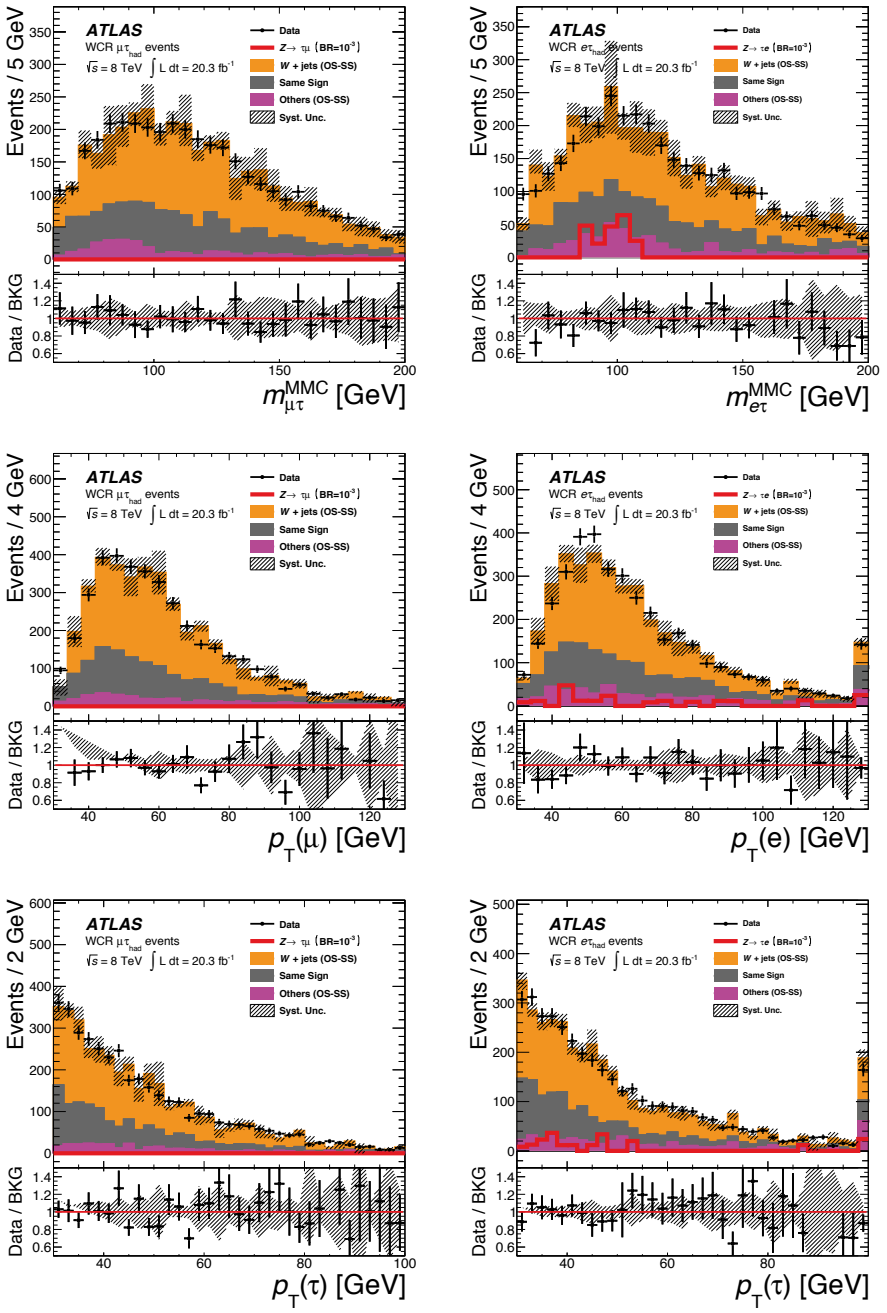

Fig. 5.4 · Various pre-fit kinematic distributions of the WCR. The left column shows the $M_{\tau\mu}^{\text{MMC}}$, $p_T(\mu)$ and $p_T(\tau_{\text{had}})$ for the $\mu\tau_{\text{had}}$ final state. The right column shows the $M_{\tau e}^{\text{MMC}}$, $p_T(e)$ and $p_T(\tau_{\text{had}})$ for the $e\tau_{\text{had}}$ final state.

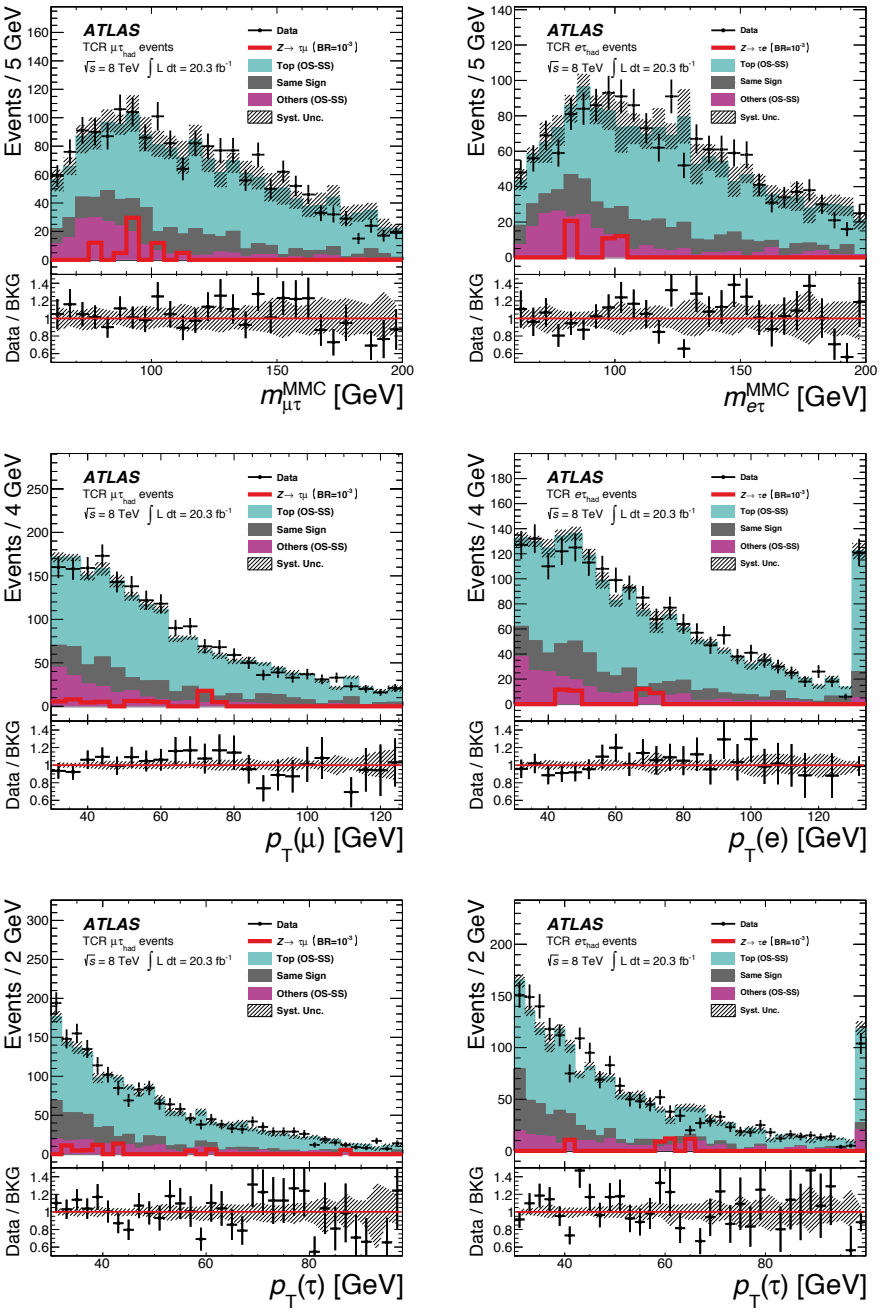

Fig. 5.5 · Various pre-fit kinematic distributions of the TCR. The left column shows the $M_{\tau\mu}^{\text{MMC}}$, $p_T(\mu)$ and $p_T(\tau_{\text{had}})$ for the $\mu\tau_{\text{had}}$ final state. The right column shows the $M_{\tau e}^{\text{MMC}}$, $p_T(e)$ and $p_T(\tau_{\text{had}})$ for the $e\tau_{\text{had}}$ final state.

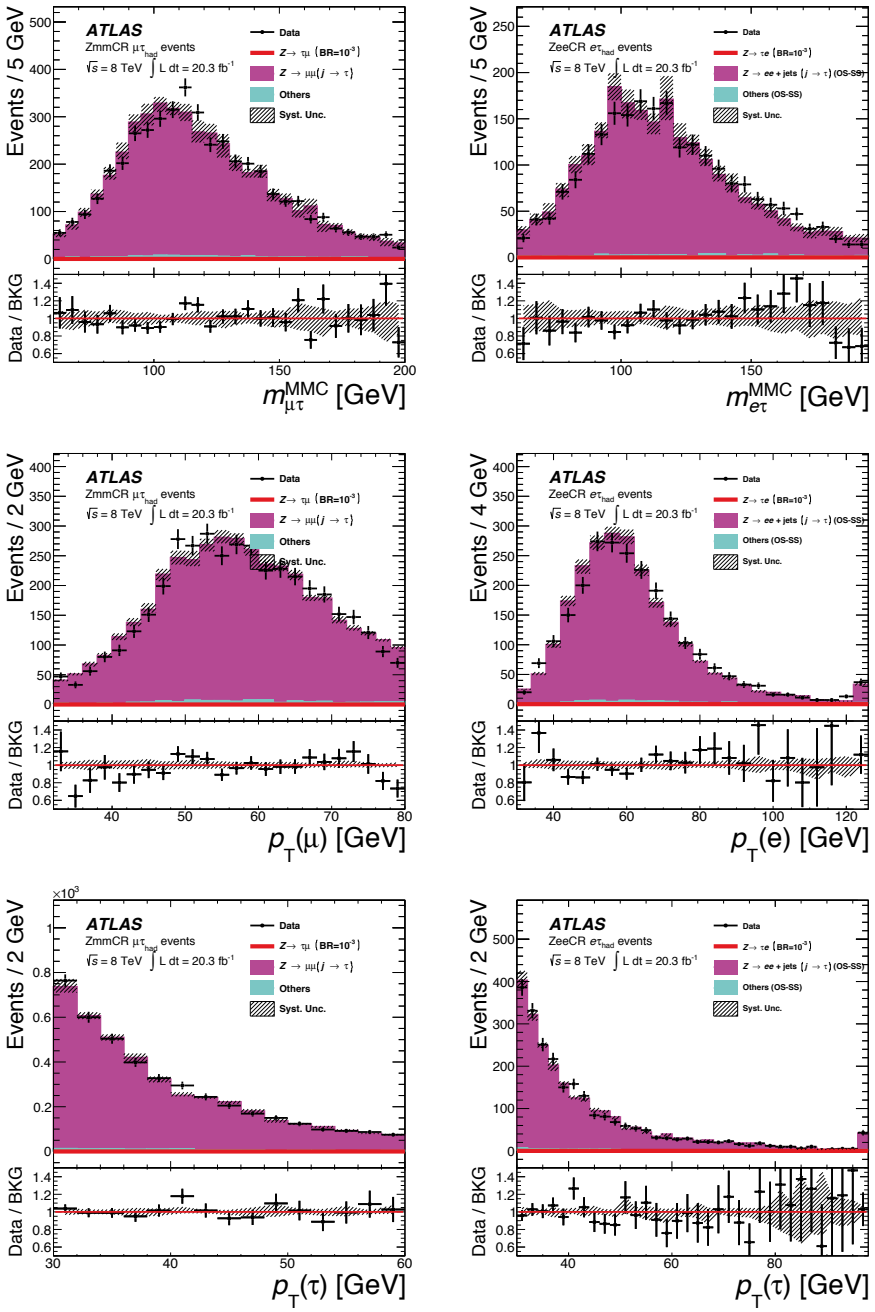

Fig. 5.6 · Various pre-fit kinematic distributions of the ZllCR. The left column shows the $M_{\tau\mu}^{\text{MMC}}$, $p_T(\mu)$ and $p_T(\tau_{\text{had}})$ for the $\mu\tau_{\text{had}}$ final state. The right column shows the $M_{\tau e}^{\text{MMC}}$, $p_T(e)$ and $p_T(\tau_{\text{had}})$ for the $e\tau_{\text{had}}$ final state.

5.2.1 Shape Corrections

To compensate for the observed discrepancy between the Monte Carlo prediction and the observed data, which can be seen in figure 5.7, shape corrections are applied to the distributions of W + jets and $Z \rightarrow ll$ backgrounds. For both these backgrounds the shape correction is extracted from their corresponding control region and subsequently applied to their complete phase space. The shape corrections are essentially (multidimensional) per bin scale-factors, which are obtained from taking the ratio of the particular background prediction and the residual one gets from subtracting the other backgrounds from the observed data. The shape corrections are based on the n_{jet} , $p_T(\tau_{\text{had}})$ and $\Delta\eta(l, \tau_{\text{had}})$ variables and follow the following binning scheme:

$$\begin{aligned} n_{\text{jet}} &= [0 - \geq 1], \\ p_T(\tau_{\text{had}}) &= [30 - 35 - 40 - 200], \\ \Delta\eta(l, \tau_{\text{had}}) &= [0 - 1.0 - 2]. \end{aligned} \tag{5.2}$$

The shape corrections are as follows:

- W + jets : Because the WCR has little contamination from the QCD multi-jet background, a separate shape correction for both OS and SS events can be extracted, allowing for possible differences in modelling between the two types. The W + jets contribution is scaled in each of the above listed bins in other to match the observed event count in data.

  Additionally for the $\mu\tau_{\text{had}}$ final-state a combined OS and SS shape correction is obtained from the high mass sideband in SR1, using events with $M_{\tau l}^{\text{MMC}} >$ 110 GeV. Because the $e\tau_{\text{had}}$ final-state has a a large component of QCD multi-jet here as can been seen in figure 5.9, this additional shape correction is not possible.

  As the W +jets contribution in SR2 is relatively small and no sideband similar to SR1 is present here, no shape correction is applied.

- $Z \rightarrow ll\,(j \rightarrow \tau_{\text{fake}})$: Secondly, a combined OS and SS shape correction is obtained and applied for jets combing from $Z \rightarrow ll$ events that fake a τ_{had} .

For each shape correction a systematic uncertainty is assigned, chosen to be the difference between the original and shape corrected distributions. Although no separate shape correction to the W +jets is applied for SR2, a systematic uncertainty is assigned however. This is done by applying the W + jets shape correction in SR1 to the W + jets distribution in SR2, and defining the difference to be the systematic uncertainty. These and other systematic uncertainties are discussed in section 5.5.

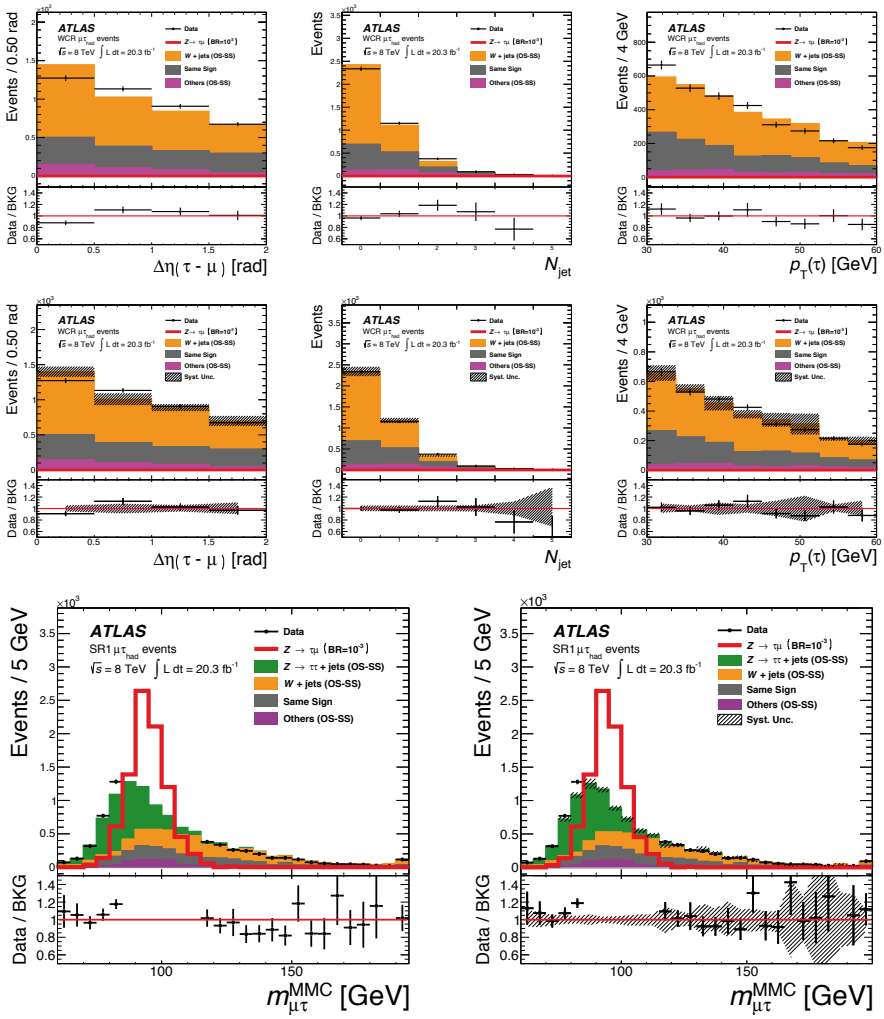

Fig. 5.7 · The top row shows the $\Delta\eta(\mu, \tau_{\text{had}})$, n_{jet} , and $p_T(\tau_{\text{had}})$ distributions of the WCR before the reweighing scheme of W + jets is applied. The middle row shows the corrected distributions. The bottom row shows the $M_{\tau\mu}^{\text{MMC}}$distribution before (left) and after (right) the reweighting in SR1, where the mis-modelling of W + jets can be seen in the sidebands.

5.3 Signal regions

After the event and physics object selection described in section 4.6 and the requirement for an oppositely charged μ and τ_{had} , the background model described in 5.2 predicts 135071 background events, both from electroweak and QCD SM processes. For the $e\tau_{\text{had}}$ final-state 124493 background events are expected. The $M_{\tau l}^{\text{MMC}}$, $p_T(l)$ and $p_T(\tau_{\text{had}})$ distributions after this selection can be seen in figure 5.8. Assuming a branching fraction of $\text{Br}(Z \to l\tau) = 10^{-5}$, the expected signal yield consists of 246 $Z \to \mu\tau$ and 205 $Z \to e\tau$ events.

The kinematic properties of the $Z \to l\tau$ decays are used to separate signal from backgrounds and define the signal regions. The event selection is chosen to give a high statistical significance as discussed in [101]. For the background yields the control region corrections are applied, as discussed in section 5.2. For the signal yield the before mentioned branching fraction of $\text{Br}(Z \to l\tau) = 10^{-5}$ is assumed. The difference in shape between signal and background is taken into account by binning the $M_{\tau l}^{\text{MMC}}$distribution according to table 5.4, and calculating the combined significance $\sqrt{\sum_{i=1}^{\text{bins}} S_i}$ of the two signal regions.

Finally two orthogonal signal regions were chosen, SR1 and SR2, of which the complete event selection after preselection is listed in tables 5.2 and 5.3. For this selection, it was also taken into account that they should exhibit a relative high difference in their shape compared to background. This seperation will make the binned likelihood minimisation discussed in section 5.4 more robust under the influence of systematics variations, which alter the $M_{\tau l}^{\text{MMC}}$distributions. Furthermore it makes the control region definitions easier by basing it on rectangular cuts in $m_T(l, E_T^{\text{miss}})$ -$m_T(\tau_{\text{had}}, E_T^{\text{miss}})$ space, of which the distributions at preselection can be seen in figure 5.8. The $M_{\tau l}^{\text{MMC}}$distributions of the two signal regions can be seen in figure 5.9. To avoid possible biasing, the data within $80 < M_{\tau l}^{\text{MMC}} < 115$ GeV is blinded in the signal regions. All other distributions with low sensitivity to signal are unblinded in order to check the quality of the background modelling.

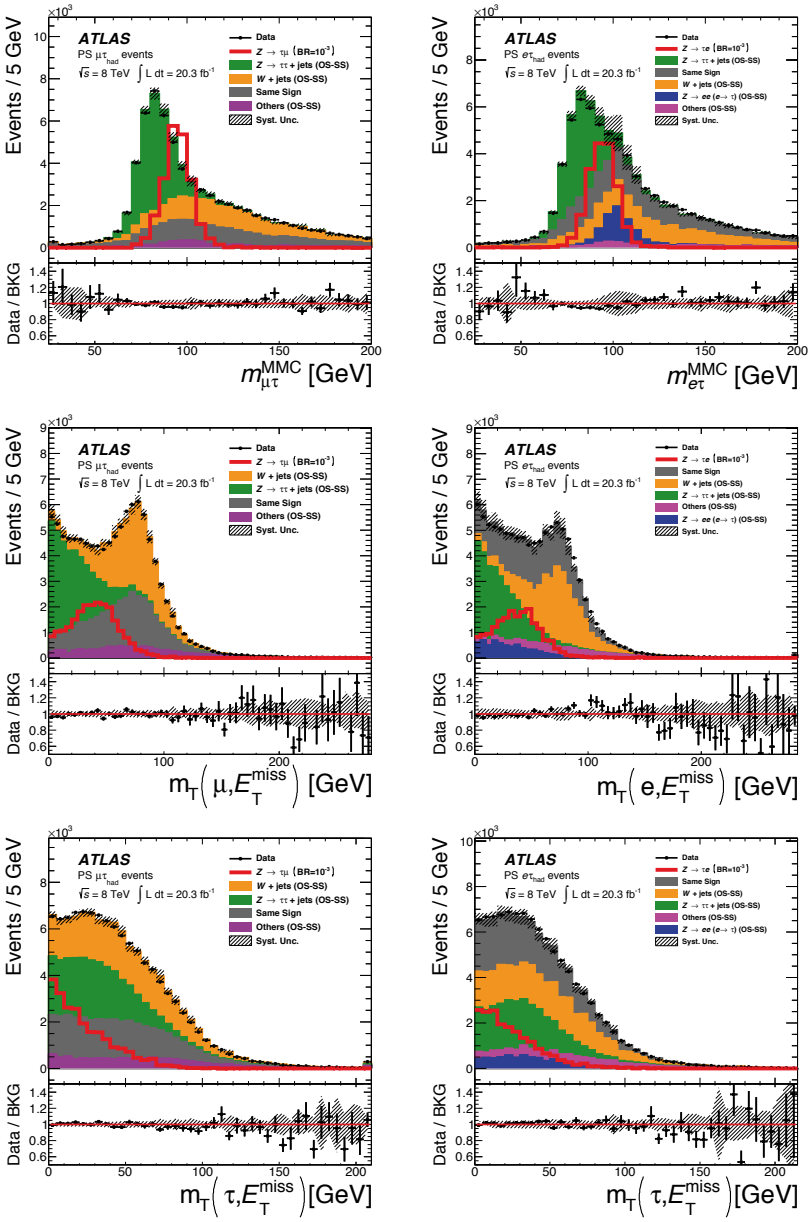

Fig. 5.8 · Various pre-fit kinematic distributions after preselection. The left column shows the $M_{\tau\mu}^{\text{MMC}}$, $m_T(\mu, E_T^{\text{miss}})$ and $m_T(\tau_{\text{had}}, E_T^{\text{miss}})$ for the $\mu\tau_{\text{had}}$ final state. The right column shows the $M_{\tau e}^{\text{MMC}}$, $m_T(e, E_T^{\text{miss}})$ and $m_T(\tau_{\text{had}}, E_T^{\text{miss}})$ for the $e\tau_{\text{had}}$ final state. For the normalisations of the background distributions, their listed cross-sections are used with a rate and shape correction applied obtained from the control regions, see section 5.2. The systematic uncertainties are added in quadrature.

cut	background	ϵ	ϵ_{tot}	$Z \to \tau\mu$	ϵ	ϵ_{tot}	$H \to \tau\tau$	ϵ	$Z \to \tau\tau$	ϵ	$Z \to \mu\mu$	ϵ	$W + jets$	ϵ	DBS	ϵ	top	ϵ	QCD	ϵ
opposite charge μ and τ_{had} with $p_T(\tau_{\text{had}}) > 30$ GeV	135071			246			319		48058		7923		60791		2831		9544		5603	
no 2$^{\text{nd}}$ μ	131351	0.97	0.97	246	1.00	1.00	319	1.00	48054	1.00	4478	0.57	60791	1.00	2719	0.96	9520	1.00	5470	0.98
MV1 b-jet veto	123095	0.94	0.91	245	0.99	0.99	313	0.98	47198	0.98	4445	0.99	60338	0.99	2650	0.97	2733	0.29	5419	0.99
$M_{\tau l}^{\text{MMC}} > 60$ GeV	81677	0.66	0.60	231	0.94	0.94	238	0.76	41140	0.87	3386	0.76	30369	0.50	1225	0.46	936	0.34	4384	0.81
$\Delta\eta(l, \tau_{\text{had}}) < 2$	74882	0.92	0.55	230	0.99	0.93	236	0.99	40967	1.00	3059	0.90	25914	0.85	1028	0.84	805	0.86	2874	0.66
SR1																				
$30 < m_T(\mu, E_T^{\text{miss}}) < 75$	27786	0.37	0.21	143	0.62	0.58	86	0.36	10324	0.25	1666	0.54	13955	0.54	481	0.47	306	0.38	969	0.34
$m_T(\tau_{\text{had}}, E_T^{\text{miss}}) < 20$ GeV	10941	0.39	0.08	93	0.65	0.38	38	0.44	5246	0.51	845	0.51	3951	0.28	145	0.30	87	0.28	629	0.65
$p_T(\mu) > 30$ GeV	9594	0.88	0.07	89	0.96	0.36	34	0.89	4295	0.82	806	0.95	3764	0.95	139	0.95	80	0.92	477	0.76
SR2																				
$m_T(\mu, E_T^{\text{miss}}) < 30$ GeV	36686	0.49	0.27	79	0.34	0.32	142	0.60	30126	0.74	1083	0.35	3213	0.12	166	0.16	136	0.17	1820	0.63
$m_T(\tau_{\text{had}}, E_T^{\text{miss}}) < 45$ GeV	26116	0.71	0.19	64	0.81	0.26	72	0.51	21742	0.72	791	0.73	1988	0.62	92	0.55	62	0.46	1368	0.75
$p_T(\mu) > 30$ GeV	16402	0.63	0.12	59	0.92	0.24	56	0.78	13182	0.61	675	0.85	1647	0.83	72	0.79	57	0.91	713	0.52

Table 5.2 · The weighted expected event yield and efficiency for the combined background samples and $Z \to \tau\mu$ signal sample after each selection cut for SR1 and SR2. For the signal normalisation the current upper limit on the branching fraction of $\text{Br}(Z \to \mu\tau) = 10^{-5}$ is used.

cut	background	ϵ	ϵ_{tot}	$Z \to \tau e$	ϵ	ϵ_{tot}	$H \to \tau\tau$	ϵ	$Z \to \tau\tau$	ϵ	$Z \to ee$	ϵ	$W + jets$	ϵ	DBS	ϵ	top	ϵ	QCD	ϵ
opposite charge, $p_T(\tau_{\text{had}}) > 30$ GeV, $p_T(e) > 26$ GeV	124493			205			259		38266		13271		52463		2150		8105		9980	
no 2$^{\text{nd}}$ e	122638	0.99	0.99	205	1.00	1.00	259	1.00	38263	1.00	11618	0.88	52463	1.00	2099	0.98	8092	1.00	9844	0.99
MV1 b-jet veto	115553	0.94	0.93	203	0.99	0.99	254	0.98	37511	0.98	11559	0.99	52040	0.99	2039	0.97	2329	0.29	9821	1.00
$M_{\tau e}^{\text{MMC}} > 60$ GeV	82159	0.71	0.66	192	0.94	0.93	190	0.75	32466	0.87	9836	0.85	28084	0.54	986	0.48	843	0.36	9754	0.99
$\Delta\eta(e, \tau_{\text{had}}) < 2$	75344	0.92	0.61	191	1.00	0.93	188	0.99	32339	1.00	9325	0.95	24520	0.87	834	0.85	729	0.86	7408	0.76
SR1																				
$30 < m_T(e, E_T^{\text{miss}}) < 75$	29273	0.39	0.24	114	0.60	0.55	68	0.36	7870	0.24	3971	0.43	13646	0.56	381	0.46	295	0.41	3043	0.41
$m_T(\tau_{\text{had}}, E_T^{\text{miss}}) < 20$ GeV	12074	0.41	0.10	70	0.61	0.34	31	0.45	3892	0.49	1708	0.43	4623	0.34	115	0.30	71	0.24	1635	0.54
$p_T(e) > 30$ GeV	11084	0.92	0.09	67	0.97	0.33	28	0.91	3307	0.85	1640	0.96	4423	0.96	106	0.93	66	0.93	1513	0.93
SR2																				
$m_T(e, E_T^{\text{miss}}) < 30$ GeV	36502	0.48	0.29	73	0.38	0.35	114	0.60	24076	0.74	4880	0.52	2945	0.12	145	0.17	112	0.15	4230	0.57
$m_T(\tau_{\text{had}}, E_T^{\text{miss}}) < 45$ GeV	26038	0.71	0.21	60	0.82	0.29	57	0.50	17330	0.72	3355	0.69	1789	0.61	83	0.57	55	0.49	3370	0.80
$p_T(e) > 30$ GeV	17974	0.69	0.14	56	0.94	0.27	46	0.80	10949	0.63	3043	0.91	1505	0.84	73	0.88	51	0.92	2308	0.68

Table 5.3 · The weighted expected event yield and efficiency for the combined background samples and $Z \to e\tau$ signal sample after each selection cut for SR1 and SR2. For the signal normalisation the current upper limit on the branching fraction of $\text{Br}(Z \to e\tau) = 10^{-5}$ is used.

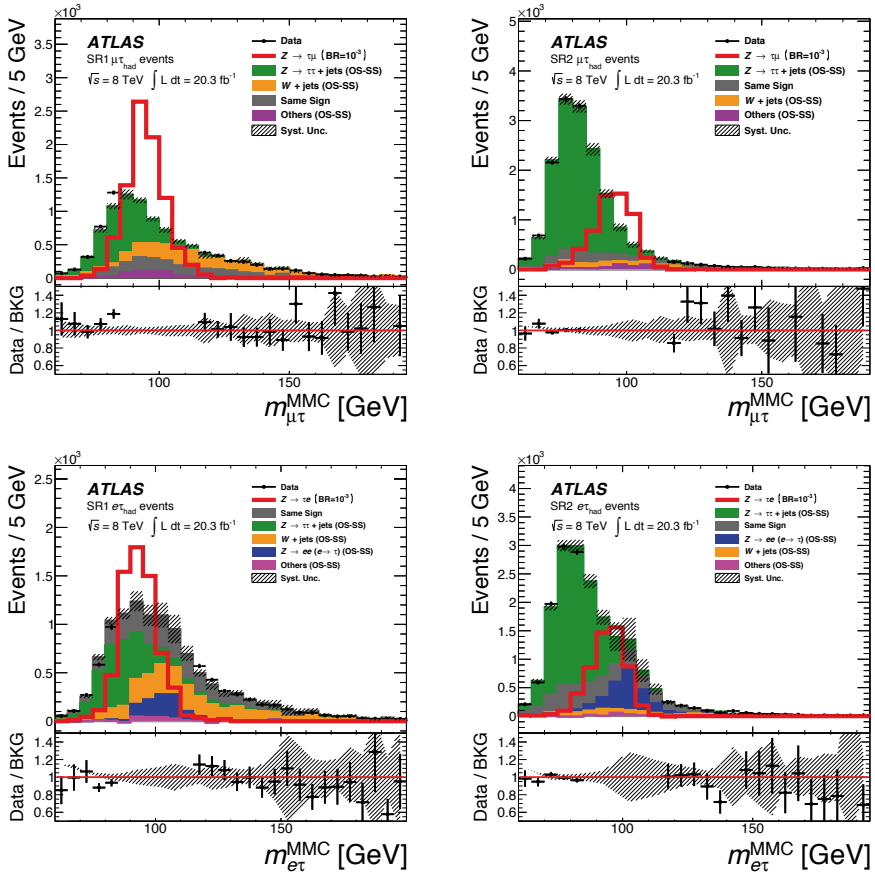

Fig. 5.9 · Both the $Z \to \mu\tau$ and $Z \to e\tau$ analysis have each two signal regions, of which the complete event selection is listed in tables 5.2 and 5.3. The top row shows the pre-fit $M_{\tau\mu}^{\text{MMC}}$ for SR1 and SR2 for the $\mu\tau_{\text{had}}$ final state, the bottom row the pre-fit $M_{\tau e}^{\text{MMC}}$ for SR1 and SR2.

5.4 Fit framework

In this analysis, the $M_{\tau l}^{\text{MMC}}$is the final discriminating variable used to evaluate the presence of a lepton flavour violating $Z \to l\tau$ signal. The expected limits are estimated using the histogram-based fitting machinery HistFactory in the RooStat package [102]. The signal and background template shapes are given with bin-by-bin fluctuations to account for statistical and systematic uncertainties. Four regions are used in the global fit: two signal regions (SR1 and SR2) and two control regions (TCR and WCR).

The signal regions are included as $M_{\tau l}^{\text{MMC}}$histograms. The control regions are included as single-bin histograms, i.e. no shape information is used. The normalisations of $Z \to \tau\tau$, $W +$ jets , $t/t\bar{t}$, and $Z \to ll$ backgrounds are free parameters in the fit. The $VV \to ll$, $Z \to \mu\mu$ (where μ fakes τ_{had}) and $H \to \tau\tau$ are small backgrounds and are normalized to their theory cross section. An additional $W +$ jets normalisation is introduced in SR1 as it was found that the $W +$jets background does not extrapolate perfectly from the WCR to SR1. The backgrounds are mostly constrained from corresponding control regions, with additional constraining power coming from the shapes of the $M_{\tau l}^{\text{MMC}}$distributions in the signal regions.

In case of the $Z \to e\tau$ analysis, the $Z \to ee$ background is split up in two contributions. One template describes the $Z \to ee\,(e \to \tau_{\text{fake}})$ and the other describes the $Z \to ee\,(j \to \tau_{\text{fake}})$ component. The former, where an electron fakes a hadronically decaying tau has a much larger contribution and is floated freely in the fit-model. Because it coincides with the $Z \to e\tau$ signal, as can be seen in figure 5.9, a dedicated control region to adjust its pre–fit normalisation was not possible as was done for other backgrounds. This make it possible for its normalisation to be significantly altered in the global fit.

To avoid dealing with unpopulated bins in the $M_{\tau l}^{\text{MMC}}$distributions and over-optimising the statistical sensitivity that will be cancelled by systematic variations, the varying bin-size scheme from table 5.4 is used. In the handfull of cases when a bin of a background template is negative, its content is set to zero in regions where no signal is expected. When signal is expected its content is set to the average statistical error of the distributions.

To implement the systematic uncertainties discussed in section 5.5, the ATLAS working groups provide tools and descriptions to calculate their one standard up and down variation on the reconstructed physics objects in this analysis. The complete event selection of the signal and control regions is then redone with these variations on all the samples, resulting in the systematic variations of the background and signal templates. All systematic uncertainties enter the fit as nuisance parameters, which are not under investigation in this analysis but still have an impact on the predictions and final result. For the normalisation uncertainties of the templates, it is required that their effect is larger than 0.5 % of the nominal prediction. For shape uncertainties a requirement on the maximum bin-by-bin variation significance $S_i = |u_i - d_i|/\sigma_i$ is applied, with u_i and d_i being the upward and downward fluctuation in each bin and σ_i the statistical uncertainty on the nominal background estimation. If $S_i < 0.2$ for all bins with a count of at least 100 events, then the shape

region	bin boundaries
SR1	$60-75-80-85-90-95-100-105-115-130-150-200-1000$
SR2	$60-70-75-80-85-90-95-100-105-115-150-1000$
WCR	$0-1000$
TCR	$0-1000$

Table 5.4 · Choice of bins used in the fit model. In the hybrid dataset the event count in the mass range $80 < M_{\tau l}^{\text{MMC}} < 115$ GeV is replaced by the ones predicted by the background model. This makes it possible to better evaluate the modelling without unblinding the region of phase space that is sensitive to the $Z \to l\tau$ processes and possibly biasing the result.

variation is considered non-significant. As an example the nuisance parameters that survive these criteria for SR1 in the $Z \to \mu\tau$ channel are summarised in table A.1.

5.4.1 Expected sensitivity

To assess the statistical power and the stability of the constructed model a series of minimisations has been performed on two simulated datasets. The first representative dataset, called the Asimov dataset, provides a simple method to obtain the median experimental sensitivity of the search for $Z \to l\tau$ decays as well as fluctuations about this expectation. The Asimov dataset is such that when one uses it to evaluate the estimators for all parameters, one obtains the true parameter values [103]. It is constructed with the event yield in all the bins set to the nominal prediction of the fitmodel. The second dataset, where the event count outside of the mass window $80 < M_{\tau l}^{\text{MMC}} < 115$ GeV of the signal regions is replaced by the observed count, is called the hybrid dataset. This hybrid dataset makes it possible to partly evaluate the used background model on actual data without unblinding, by looking at the sidebands where no signal is expected.

With the HistFactory machinery a probability density function is created that has all systematic uncertainties implemented as nuisance parameters. The minimised probability density functions are projected on top of the event count in the regions of the hybrid dataset in figure 5.10, for both the $Z \to \mu\tau$ and $Z \to e\tau$ analyses. As can be seen the background prediction is in good agreement with the observed yields of the sidebands.

To predict the sensitivity of the analysis, the expected limits are calculated using the Asimov and hybrid dataset. As the LFV $Z \to l\tau$ decays are not established signals, the CL_S method [104] is used to determine the exclusion intervals. In case of no discovery of the LFV signal, it is expected that the upper limits can be set at $\text{Br}(Z \to \mu\tau) < 2.6 \times 10^{-5}$ and $\text{Br}(Z \to e\tau) < 4.3 \times 10^{-5}$ with a 95% confidence level. The p-value versus the signal strength μ is shown in figure 5.11. It reveals that the observed limits on the hybrid datasets are in perfect agreement with the

expectation from the background model. The lower sensitivity to $Z \to e\tau$ events can be attributed to the lower signal accepance for electrons, as well as the higher QCD multi-jet and $Z \to ee$ background contributions.

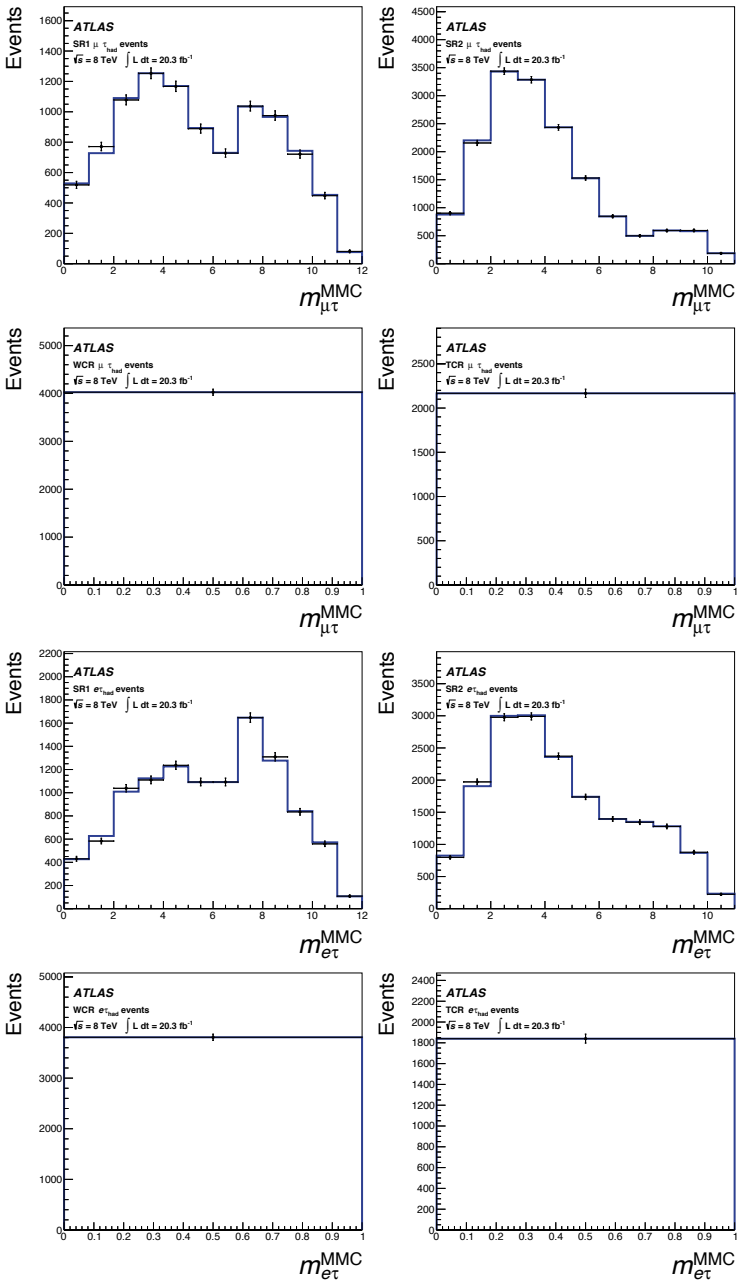

Fig. 5.10 · The projection of the fitted probability density function on the observed $M_{\tau l}^{\mathrm{MMC}}$distributions of the hybrid dataset. The $M_{\tau l}^{\mathrm{MMC}}$distributions are binned according to the binning scheme of table 5.4. The top two rows show the SR1 (top left), SR2 (top right), WCR (left bottom) and TCR (right bottom) signal and control regions for the $Z \to \mu\tau$ channel. The bottom two rows show them for the $Z \to e\tau$ channel.

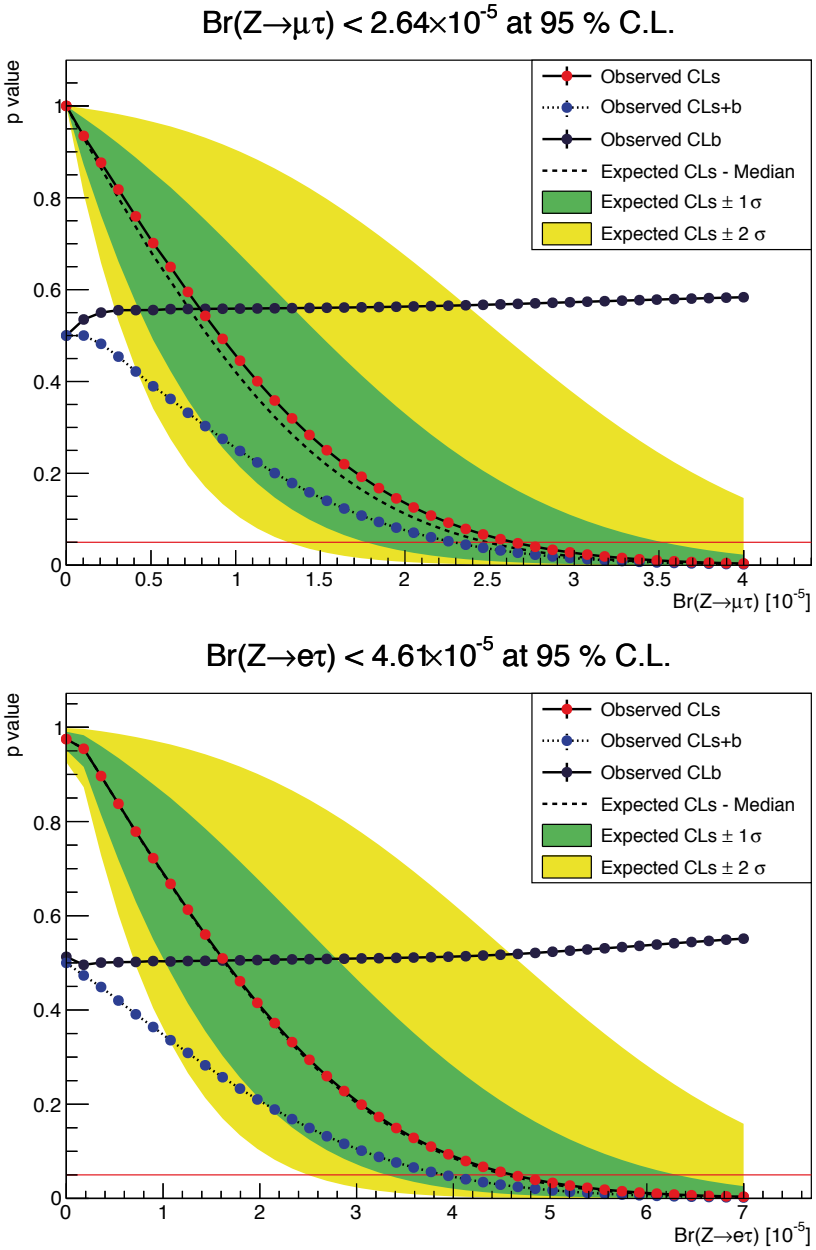

Fig. 5.11 · The observed p-value as a function of the branching fraction of $Z \to l\tau$ for the CLs, CLb and CL$s+b$ hypotheses for the hybrid dataset together with the expectation by the used background model. The intersection of the $p = 0.05$ line and the CLs curve denotes the found 95% upper limit. The top plot shows the result for $Z \to \mu\tau$, the bottom for $Z \to e\tau$.

5.5 Systematics uncertainties

There are certain known inaccuracies in the measurement and reconstruction of the physical objects discused in chapter 4. To account for them the corresponding ATLAS working groups provide tools and descriptions to model them. The analysis presented in this chapter is sensitive to the following systematic uncertainties.

Luminosity

The uncertainty on the integrated luminosity is ±2.8 % for data taken in 2012. The method for determining the luminosity as well as the results for the data taken in 2010 and 2011 are discussed in [105].

Tau energy scale

As the τ lepton decays to a well known combination of charged and neutral hadrons, the energy scale of τ_{had} candidates is derived independently of the jet energy scale [106]. The upwards and downwards variations are applied to the objects according to the recommendations of the tau working group and are also propagated to the E_T^{miss} calculation [107]. As this is a shape-changing systematic, the final $M_{\tau l}^{\text{MMC}}$ discriminant is fully recalculated on samples with different TES values.

The effect of the tau energy resolution (TER) was studied in the context of the $H \to \tau\tau$ analysis [80] and was found to have a negligible effect on the reconstructed Higgs mass $M_{\tau\tau}^{MMC}$, see section 4.9 on its calculation. The TER effect should be even smaller for the $M_{\tau l}^{\text{MMC}}$distribution due to a smaller role of the τ_{had} momentum in its reconstruction and is therefore neglected.

Hadronic tau identification

The τ working group provides a correction factor for the tau identification efficiency, measured in tag-and-probe studies of $Z \to \tau\tau$ events [107]. This correction factor is varied up and down within its uncertainty, to account for its effect on this analysis. This systematic uncertainty is only applied to truth-matched hadronic τ_{had} candidates which are not misidentified.

A correction factor for misidentified electrons is also provided by the τ working group. It is treated in the same way as other correction factors to obtain a systematic uncertainty, but is only applied to hadronic τ_{had} candidates which are truth–matched to an electron.

Lepton momentum and energy resolution

By smearing the appropriate objects according to the recommendation of the performance groups, the uncertainty of the electron energy and muon momentum resolution is accounted for [108, 109].

Lepton reconstruction and identification efficiency

The combined performance groups provide correction factors for the efficiency of reconstructing and identifying leptons and muons for the Monte Carlo samples [110, 109]. These correction factors are varied up and down within their uncertainties, to

obtain the effect of the lepton reconstruction and identification efficiency on the analysis.

Lepton isolation efficiency

The efficiencies of the isolation cuts applied on the electron and muon candidates are measured through tag-and-probe studies, deriving correction factors for the Monte Carlo. These correction factors are then varied upwards and downwards within their uncertainties, to obtain the effect on the analysis.

Trigger efficiency

The trigger efficiencies of the used single lepton triggers are measured through tag-and-probe studies, to account for differences in efficiency compared to that measured in data and Monte Carlo simulation. The obtained correction factors factors for the Monte Carlo samples are varied up and down within their uncertainties, to obtain the effect on the analysis.

Jet energy scale

To obtain the systematic uncertainties and correlations due to jet energy scale (JES), the prescription of the Jet Performance Group is followed [111, 112]. As the LFV analysis does not explicitely use jets for the event selection, apart from the selection of the TCR, the impact of most of the JES uncertainties are quite small. The JES uncertainties that are relevant for the LFV search are:

in-situ jet energy corrections This group account for bin-to-bin correlations in jet calibration and corrections derived from in-situ techniques, and correspond to physical sources.

η intercalibration The uncertainty in the intercalibration in different detector pseudorapidity regions.

flavour composition and response This uncertainty concerns light, non b–jets. It is due to quark-initiated and gluon-initiated jets having a different calorimeter response. Depending on if the signal and background processes are more quark or gluon dominated, one of two uncorrelated uncertainties are used.

b–jets This uncertainty affects only the calorimeter response of b–jets.

pile-up The uncertainties due to in-time and out-of-time pileup.

Jet energy resolution

The systematic uncertainty caused by the finite jet energy resolution (JER) is obtained by smearing every jet with a smearing factor according to the prescription of the Jet Performance Group [113]. The changes in jet energy due to this smearing are also propagated into the E_T^{miss} calculation. The final effect of the variation is symmetrised in order to have a two-sided uncertainty in the fit.

E_T^{miss} uncertainties

The systematic uncertainty due to the energy scales of the leptons, τ_{had} and jets which are described above are propagated to the E_T^{miss} calculation. In addition to that, the E_T^{miss} soft term scale and resolution uncertainties (see section 4.5) are also taken into account according to the prescription of the Etmiss performance group [114].

b-jet identification

The so-called MV1 algorithm is used to to distinguish b-quark jets from jets containing only lighter quarks [115]. It systematic uncertainty comprises of three components: `BTag_BEFF`, `BTag_CEFF` and `BTag_LEFF`. These indicate the tagging efficiencies of b, c and light jets respectively.

Background estimation techniques

The used background estimation techniques bring with them systematic uncertainties. To obtain the normalisation and shape correction for the W + jets and $t/t\bar{t}$ backgrounds, dedicated control regions are used. Because these control regions are kinematically different from the signal regions, extrapolation uncertainties are introduced.

For the W + jets this uncertainty is estimated by replacing the ALPGEN PYTHIA samples with ALPGEN HERWIG samples. The deviation from the nominal is symmetrized and and used as an uncertainty. The amount of W + jets in SR2 affects the $Z \to \tau\tau$ background normalisation. Therefore, this `WJ_EXTRAPOLATION` uncertainty is also introduced for the $Z \to \tau\tau$ background and is anti-correlated with its impact on W+jets . The effect of of this nuisance parameter on the W+jets template can be seen in figure 5.12.

To estimate the extrapolation uncertainty for the top background predictions, POWHEG and MC@NLO $t\bar{t}$ samples were used. The difference between predictions based on these two samples is taken as a corresponding extrapolation uncertainty `TOP_EXTRAPOLATION`.

For the shape corrections for the $Z \to ll$ and W + jets background discussed in section 5.2.1, systematic uncertainties for the reweighting are included by comparing the corrected with the un–corrected templates, namely `WJ_SR1_SHAPE`, `WJ_SR1_SR2_SHAPE` and `Z_SHAPE`.

QCD scale and PDF set

The normalizations for the major backgrounds are obtained by data–driven way. However, the $VV \to ll$, $Z \to \mu\mu$ (where μ fakes τ_{had}) and $H \to \tau\tau$ are small backgrounds and are normalized to their theory cross section. The uncertainties due to missing higher order QCD corrections on these cross sections and the different parametrisation used in PDF sets have to be taken into account. The values for $H \to \tau\tau$ are taken from the CERN Yellow report [116]. For the other backgrounds as well as the LFV $Z \to \mu\tau$ signal the values are obtained from [117].

Nuisance parameter	$\Delta\text{Br}(Z \to \mu\tau)$	Nuisance parameter	$\Delta\text{Br}(Z \to e\tau)$
WJ_EXTRAPOLATION	5.9 %	EL_SCALE	5.4 %
rQCD	3.5 %	norm_LH12_ZttEmb	4.1 %
norm_LH12_ZttEmb	3.2 %	TES_TOTAL_2012_EL	4.1 %
MET_RESOSOFT	1.8 %	ANA_EMB_ISOL	3.9 %
ANA_EMB_ISOL	1.7 %	Wj_shape_corr	1.7 %
pdf_qq	1.6 %	norm_LH12_ZeeET	1.6 %
all	45.2 %	all	49.4 %

Table 5.5 · The nuisance parameters that give rise to the largest uncertainty on the expected upper limit on the $\text{Br}(Z \to l\tau)$ channels. The values are obtained by removing a particular nuisance parameter from the fit model, and calculating the change in expected limit $\Delta\text{Br}(Z \to l\tau)$ on the Asimov dataset.

Embedding Method

Two systematic uncertainties are associated with the embedding method that is used to generate the $Z \to \tau\tau$ data driven sample. The first one is the isolation requirement on the leptons to select the $Z \to ll$ events. To quantify this uncertainty named ANA_EMB_ISOL, events are selected with a tighter and looser isolation requirement. The effect of this systematic uncertainty can be seen in figure 5.12.

The second originates from the replacement of these selected leptons with taus, which also brings significant uncertainties on the modelling calorimeter response. To estimate this uncertainty named ANA_EMB_MFS, the energy of each calorimeter cell is varied by 20 % before the replacement.

5.5.1 Impact of systematic uncertainties on measurement

The systematic uncertanties are introduced as nuisance parameters in the fit-model and dilute the sensitivity with which $Z \to l\tau$ events can be distinguished from the different background processes. A summary of all the systematic uncertainties used in the fit model is shown in table A.2. The nuisance parameters that give rise to the largest uncertainty on the expected upper limit on the $\text{Br}(Z \to l\tau)$ channels are listed in figure 5.5.

In figures 5.13 and 5.14 the systematics uncertainties are ranked according to their impact on the extracted signal strength. This impact is determined by setting a nuisance parameter fixed to their respective up and down variation $\sigma_{\text{up/down}}$ in the likelihood minimisation, and measuring the change in extracted signal strength $\Delta\mu_{\text{up/down}}$. In the same plot the one sigma pull of the nuisance parameters are overlaid. As can be seen all the parameters are well behaved, there are no overconstraints or biases when performing the likelihood minimisation on the hybrid dataset. There

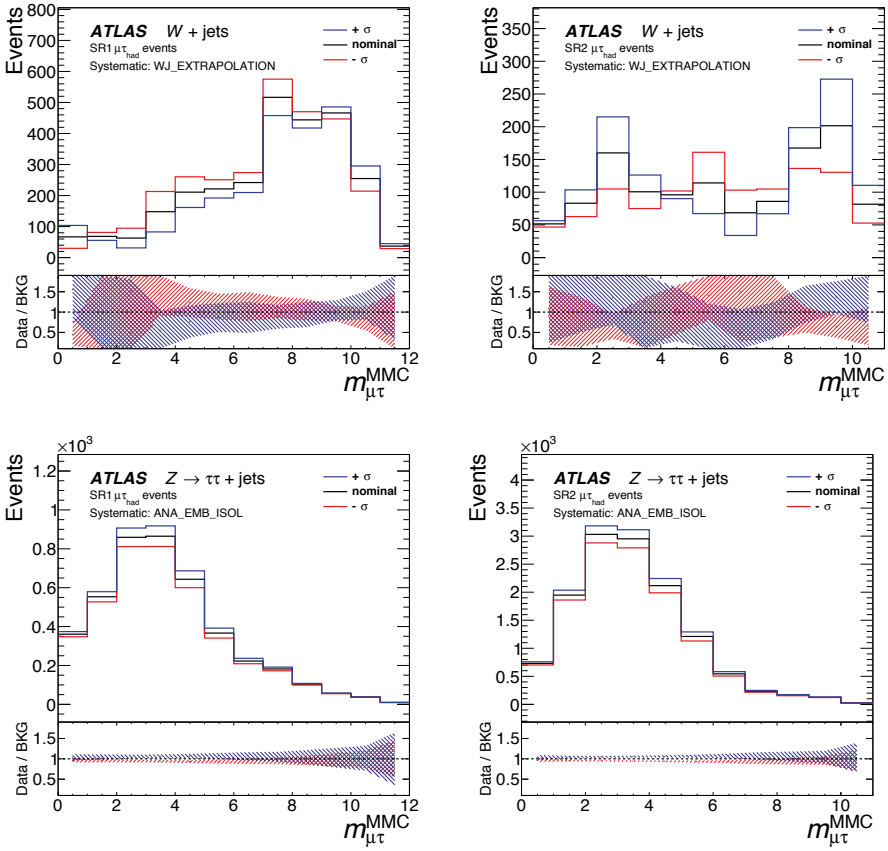

Fig. 5.12 · The systematic variations of the signal $M_{\tau\mu}^{\mathrm{MMC}}$templates associated with W + jets extrapolation from the control region and the isolation requirement for the generation of the embedded $Z \to \tau\tau$ sample. The plots underneath show the ratio of the systematic variations with the nominal template, with the band indicating the systematic uncertainty.

are no significantly constrained or pulled nuisance parameters. The correlation matrix of the nine nuisance parameters which have the highest correlation with the signal strength are shown in figure A.1.

The largest systematic uncertainty arises from the modelling of the W + jets background, in particular the difference in both event yield and normalisation when using samples made with Pythia or Herwig as an Monte Carlo generators. Furthermore the normalisation uncertainty of this background in SR1 plays an important role.

Furthermore the uncertainty on r_{QCD} which is used to model QCD background, and the experimental resolution of the E_T^{miss} vector, which is both used for selection of the signal and control regions and the calculation of final the discriminating variable $M_{\tau l}^{\text{MMC}}$ have an important impact on the sensitivity.

Other important sources of uncertainty are coming from the large $Z \to \tau\tau$ background, from which the normalisation and the isolation requirement on the leptons for the generation of the sample have the largest effect on the measured signal strength.

For the electron channel a similar trend is seen. However as an electron fakes a τ_{had} candidate at much higher rates than a muon, the electron energy scale uncertainty is a dominating uncertainty. Furthermore the W + jets extrapolation uncertainty has less impact because no significant effect on the shape of the $M_{\tau e}^{\text{MMC}}$ distribution was observed when comparing the PYTHIA and HERWIG samples.

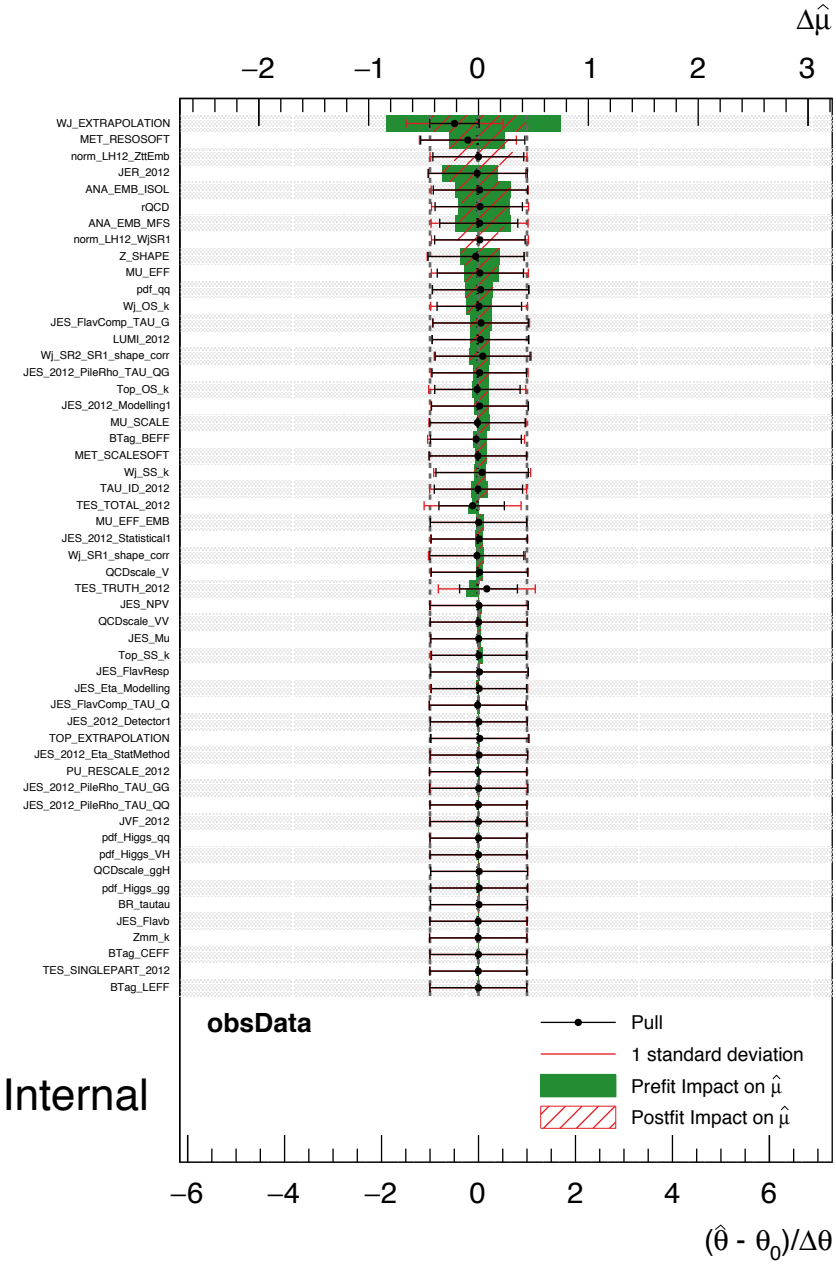

Fig. 5.13 · The pull and impact of the nuisance parameters before and after minimising the fit model to the blinded hybrid dataset for the $Z \to \mu\tau$ channel.

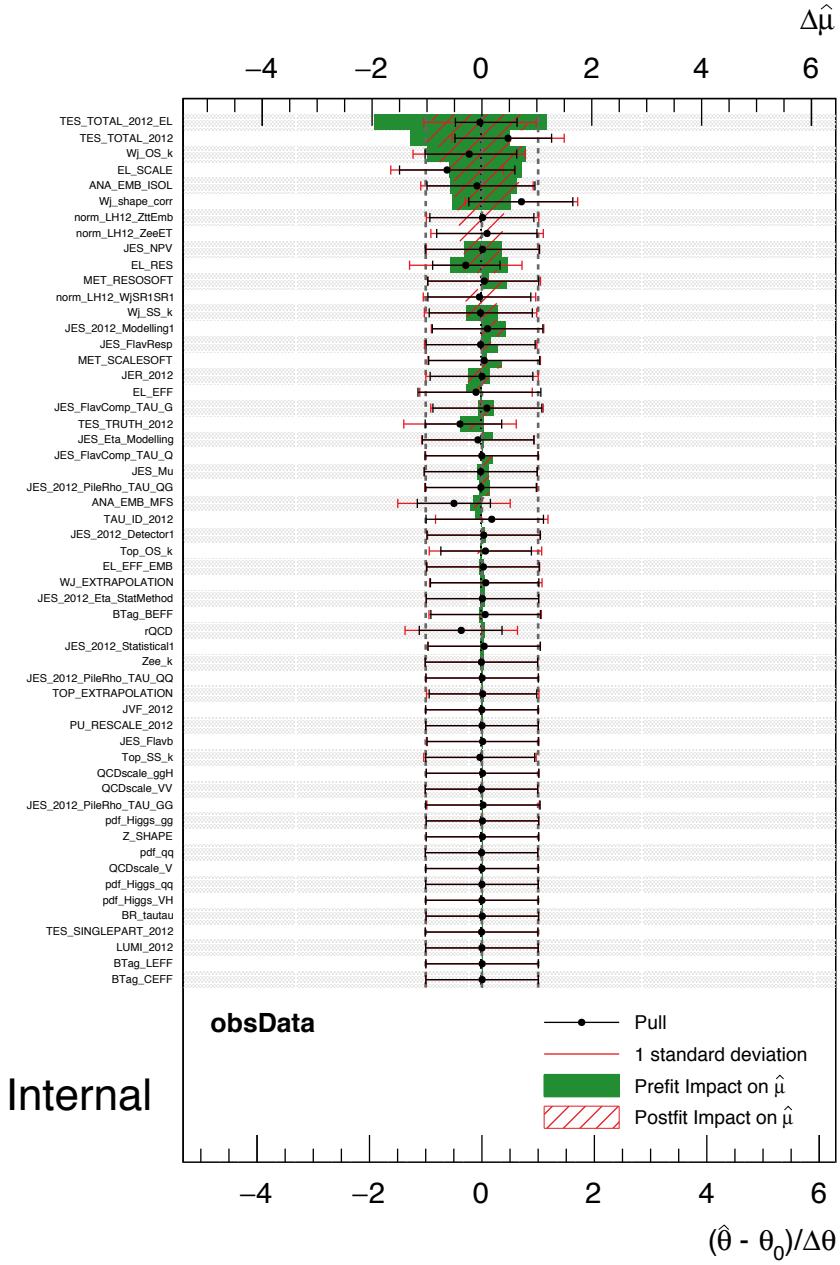

Fig. 5.14 · The pull and impact of the nuisance parameters before and after minimising the fit model to the blinded hybrid dataset for the $Z \to e\tau$ channel.

Conclusion

A binned likelihood model with the invariant mass of the Z as the discriminating observable has been constructed, with the use of a combination of Monte Carlo and data–driven techniques. Four orthogonal regions are used in the global fit for both the muon and electron channels: two signal regions and two control regions. The signal regions were optimised to possess a large shape difference in the $M_{\tau l}^{MMC}$ *distribution for the signal and background processes in addition to having a high statistical significance.*

To avoid possible biasing, the optimisation and model checks have been performed with the signal regions blinded in the mass window $80 < M_{\tau l}^{MMC} < 115$ *GeV. Using the* CL_S *method it is expected that the upper limits can be set at* $Br(Z \to \mu\tau) < 2.6 \times 10^{-5}$ *and* $Br(Z \to e\tau) < 4.3 \times 10^{-5}$ *in the absence of charged lepton flavour violation.*

The systematic uncertainties are introduced as nuisance parameters and dilute the sensitivity with which signal can be distinguished from the different background processes. The largest systematic uncertainties arises from the modelling of the large $W+jets$*,* $Z \to \tau\tau$ *and QCD multi-jet backgrounds, with the total systematics expected to contribute 45.2 % and 49.4 % to the total uncertainty on the* $Z \to \mu\tau$ *and* $Z \to e\tau$ *measurements respectively. All the nuisance parameters are well behaved: there are not overconstraints, biases or large one–sided impacts when performing the likelihood minimisation on the blinded dataset.*

chapter six

Unblinded results

This chapter presents the unblinded results for the search for the charged lepton flavour violation $Z \to l\tau$ (with $l = e, \mu$), using the model described in the previous chapter to extract their branching fractions. For this analysis the total data recorded by the ATLAS experiment in 2012 is used, totalling a recorded luminosity of $\mathcal{L} = 20.3 fb^{-1}$ after passing quality criteria. The high cross section of $\sigma_{pp\to Z} = 33$ nb translates into roughly 700 million Z bosons [117]. The high amount available statistics produced by the LHC gives rise to a new opportunity to search for these decays, despite the fact that pile-up and the underlying event make it a more challenging environment than previous dedicated experiments.

6.1 Observed invariant mass distribution

After unblinding the sensitive mass windows, the complete observed $M_{\tau l}^{\text{MMC}}$ distribution is used for the search of $Z \to l\tau$ decays, which is binned according to the scheme described in table 6.1. The minimised probability density functions are projected on top of the event count in the signal and control region of both the $Z \to \mu\tau$ and $Z \to e\tau$ channels in figure 6.1.

region	bin boundaries
SR1	$60 - 75 - 80 - 85 - 90 - 95 - 100 - 105 - 115 - 130 - 150 - 200 - 1000$
SR2	$60 - 70 - 75 - 80 - 85 - 90 - 95 - 100 - 105 - 115 - 150 - 1000$
WCR	$0 - 1000$
TCR	$0 - 1000$

Table 6.1 · The employed binning scheme of the fit model.

As can be seen the background prediction is in good agreement with seven out of eight used regions. There seems to be a discrepancy however in the between shape of the pdf and the observed event count in bin 3,4 and 5 of SR1 of the $Z \to \mu\tau$ channel.

Figure 6.2 shows the $M_{\tau l}^{\text{MMC}}$distribution for the data as well as the background composition for the four signal regions after the likelihood minimisation

of the complete background model. Here we can observe this behaviour in the $80 < M_{\tau\mu}^{\text{MMC}} < 95$ GeV range for the $Z \to \mu\tau$ channel in SR1. No obvious mismodelling can explain this deviation as the two main backgrounds seem to agree well in the other signal regions. The data of SR2 of $Z \to \mu\tau$ is totally dominated by $Z \to \tau\tau$ events and agrees well with the background prediction. The sideband of SR1 of $Z \to \mu\tau$, as well as the complete mass window for $Z \to e\tau$ seem to have no issues with the $W +$ jets background.

Several additional checks have been performed. The $Z \to \tau\tau$ events have been reweighted according to the p_T of the τ_{had} candidate, to explore if the issue could be related to a tau energy scale mismodelling. Furthermore the $W +$jets templates have been smoothed, to see how much the result is dependent on the shape of their predicted distributions. Lastly a decorrelation of the nuisance parameters between the signal regions has been tried, to explore if kinematic differences could be an issue. None of the tests altered the result significantly, and the other SR1 distributions, including lepton momenta, transverse masses, and missing transverse momentum, are in excellent agreement with the prediction. Therefore this discrepancy is attributed to a statistical fluctuation.

As can be seen in figure 6.2 the background prediction for the shape and normalisation for the $M_{\tau e}^{\text{MMC}}$of the signal regions are in good agreement with the observed data. As mentioned in the previous chapter, no control region was used for the $Z \to ee\,(e \to \tau_{\text{fake}})$ contribution as it coincides with the $Z \to e\tau$ peak. Therefore its pre-fit normalisation was not adjusted but its normalisation was allowed to float freely in the likelihood minimisation. Figure 6.3 shows the profile likelihood scan of its value; the final fit value corresponding to a data–driven correction of 6.5% to the Monte Carlo prediction.

6.2 Extracted signal strength and background composition

The numbers of observed events and background composition for each of the signal regions in the $80 < M_{\tau l}^{\text{MMC}} < 115$ GeV mass window are given in table 6.2.

No signal is observed in the $Z \to \mu\tau$ channel and using the CL_S limit-setting techniques described in the previous chapter, an upper limit on its branching fraction has been calculated. With an 95% confidence level the branching fraction is observed to be $\text{Br}(Z \to \mu\tau) < 1.7 \times 10^{-5}$, which is significantly lower than the expected $\text{Br}(Z \to \mu\tau) < 2.6^{+2.1}_{-0.7} \times 10^{-5}$, but still well within two standard deviations of the expected upper limit as can also been seen in figure 6.4.

A slight, non-significant signal is observed in the $Z \to e\tau$ channel, giving a best fit value of $\text{Br}(Z \to e\tau) = 0.6^{+2.2}_{-2.3} \times 10^{-5}$. Given its value in comparison to its standard deviation, this can be well explained by a statistical fluctuation and it does not give a hint for new physics. Figure 6.4 shows that the observed upper limit $\text{Br}(Z \to e\tau) < 4.7 \times 10^{-5}$ is very close to the expectation value of $\text{Br}(Z \to e\tau) < 2.6^{+2.1}_{-0.7} \times 10^{-5}$.

The results are summarised in table 6.3, which shows the expected and observed 95% CL exclusion limits as well as the best fit values for the branching fraction of $Z \to l\tau$ for SR1, SR2 and the combined signal extraction.

6.3 Systematic uncertainties

In figures 6.5 and 6.6 the pull and ranking of the systematic uncertainties and normalisation are shown. Although there are no large biases or tensions, two nuisance parameters stand out. For the $Z \to \mu\tau$ channel the nuisance parameter associated with the systematic uncertainty that accounts for the modelling difference between the PYTHIA and HERWIG of the $W+$jets sample is roughly one standard deviation biased and more constrained then expected. This however is most likely caused by the statistical fluctuation in SR1, which the model tries to account for.

In the $Z \to e\tau$ channel the nuisance parameter associated with the r_{QCD} is biased, although still well within one sigma deviation. This might indicate that the $r_{\text{QCD}} = 1.00 \pm 0.13$ that was determined for the $H \to \tau\tau$ analysis [80] and describes the symmetry between OS and SS QCD multi-jet events, might be slightly different for the event selection of this analysis. However the difference is well within the systematic uncertainty, and furthermore, as the parameter is not highly ranked, the impact on the final result is negligible.

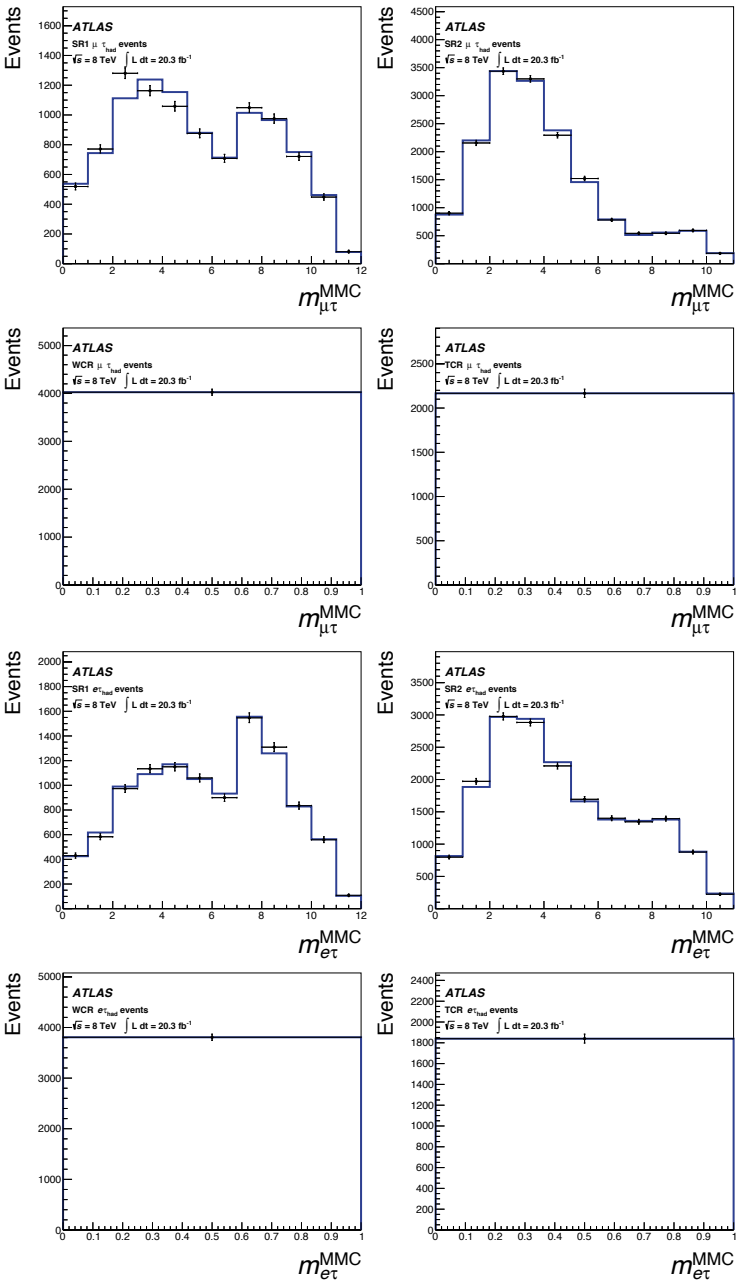

Fig. 6.1 · The projection of the fitted probability density function on the observed $M_{\tau l}^{\mathrm{MMC}}$distributions of the unblinded 2012 ATLAS dataset. The $M_{\tau l}^{\mathrm{MMC}}$distributions are binned according to the binning scheme of table 6.1. The top two rows show the SR1 (top left), SR2 (top right), WCR (left bottom) and TCR (right bottom) signal and control regions for the $Z \to \mu\tau$ channel. The bottom two rows show them for the $Z \to e\tau$ channel.

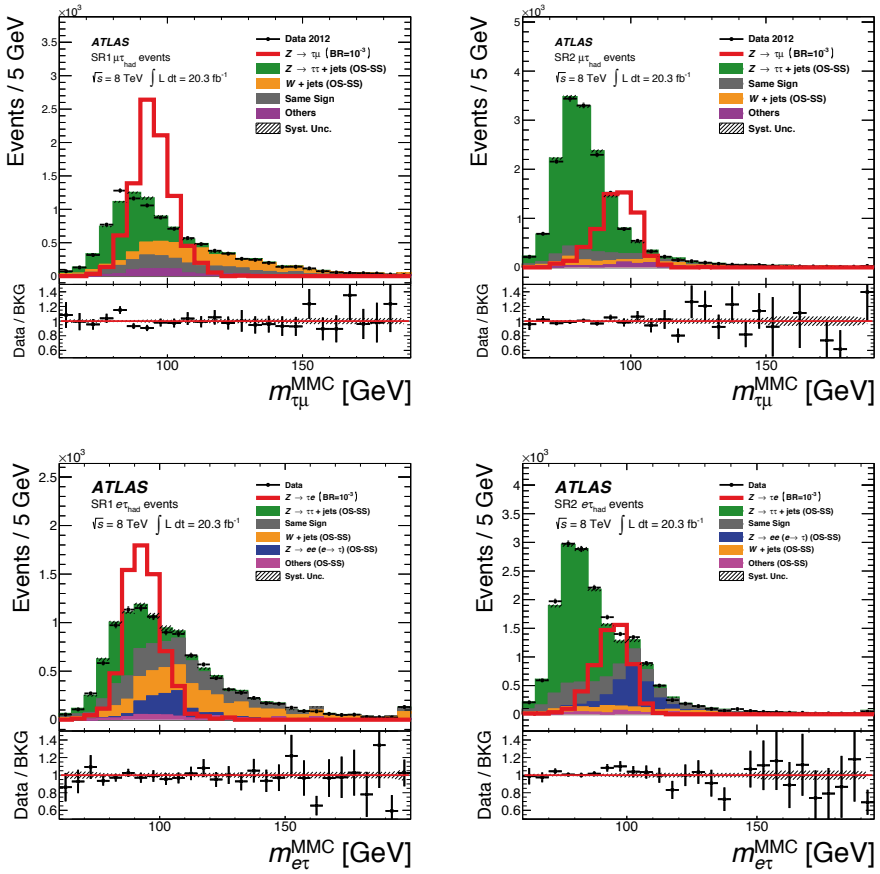

Fig. 6.2 · The distributions of the mass reconstructed by the Missing Mass Calculator $M_{\tau l}^{\mathrm{MMC}}$. The plots show the full 2012 ATLAS dataset as well as the predicted background distribution. The signal distribution is shown assuming a branching fraction of $\mathrm{Br}(Z \to l\tau) = 10^{-3}$ to make it visible. The predicted background is given by the background model with all the systematic uncertainties incorporated as nuisance parameters, after a likelihood minimisation has been performed to the full unblinded dataset. The bottom panel of each sub-figure shows the ratio of the observed data and the estimated background. The hatched grey band for the ratio illustrates post–fit systematic uncertainties on the background prediction. The statistical uncertainties for data and background predictions are added in quadrature for the ratios.

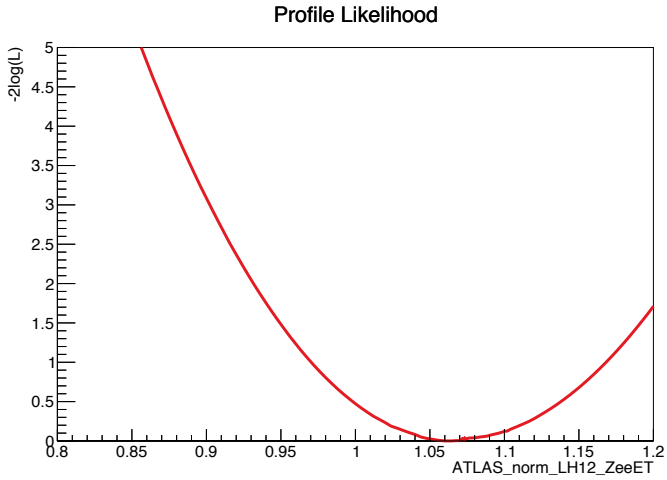

Fig. 6.3 · The profile likelihood scan of the normalisation of the $Z \rightarrow ee\,(e \rightarrow \tau_{\text{fake}})$ contribution. The extracted normalisation from the combined fit is 6.5% higher then the unadjusted pre-fit value based on the cross section.

Table 6.2 · Data yields, signal and post-fit OS–SS background predictions for the $80 < M_{\tau l}^{\text{MMC}} < 115$ GeV region. The signal predictions are given assuming Br($Z \to \mu\tau$) = 10^{-5}. The background predictions are obtained from the combined fit to SR1, SR2, WCR and TCR. To calculate these quantities for SR1 and SR2, the signal strengths are decorrelated in the signal regions and set to zero in the control regions. The post-fit values of systematic uncertainties are provided for the background predictions. For the total background, all correlations between various sources of systematic uncertainties and backgrounds are taken into account.The quoted uncertainties represent the statistical (first) and systematic (second) uncertainties, respectively.

	$Z \to \mu\tau$ SR1	$Z \to \mu\tau$ SR2	$Z \to e\tau$ SR1	$Z \to e\tau$ SR2
Signal	$86.0 \pm 2.3 \pm 21.9$	$56.3 \pm 1.8 \pm 17.7$	$64.3 \pm 2.7 \pm 18.9$	$53.7 \pm 2.5 \pm 17.1$
$Z \to \tau\tau$	$3256 \pm 27 \pm 56$	$7060 \pm 40 \pm 150$	$2317 \pm 29 \pm 82$	$5601 \pm 44 \pm 222$
W + jets	$1350 \pm 70 \pm 110$	$590 \pm 50 \pm 70$	$1558 \pm 90 \pm 169$	$590 \pm 49 \pm 62$
$t/t\bar{t}$	$22 \pm 4 \pm 4$	$15 \pm 4 \pm 4$	$18 \pm 4 \pm 3$	$12 \pm 3 \pm 3$
Same–Sign events	$1110 \pm 40 \pm 100$	$932 \pm 32 \pm 87$	$1814 \pm 46 \pm 194$	$1966 \pm 47 \pm 211$
$H \to \tau\tau$	$25.1 \pm 0.5 \pm 3.0$	$41.0 \pm 0.6 \pm 5.2$	$19.4 \pm 0.4 \pm 2.7$	$32.3 \pm 0.5 \pm 4.1$
$Z/VV \to \mu\mu$	$410 \pm 60 \pm 50$	$240 \pm 60 \pm 60$	–	–
$Z \to ee\,(e \to \tau_{\text{fake}})$	–	–	$956 \pm 62 \pm 97$	$2198 \pm 105 \pm 234$
$VV \to ee{+}Z \to ee\,(j \to \tau_{\text{fake}})$	–	–	$185 \pm 52 \pm 90$	$156 \pm 48 \pm 94$
Total background	$6170 \pm 100 \pm 100$	$8880 \pm 100 \pm 140$	$6868 \pm 132 \pm 139$	$10555 \pm 141 \pm 189$
Data	6134	8982	6763	10929

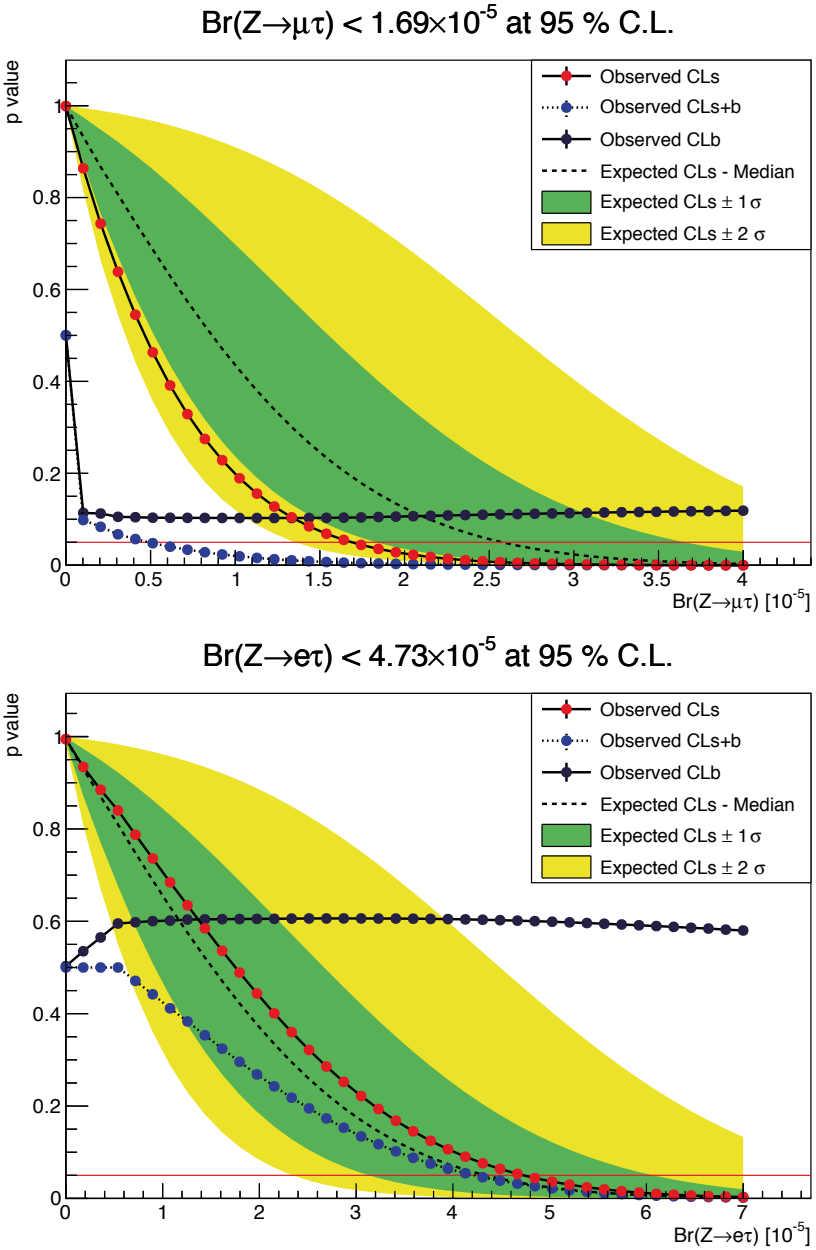

Fig. 6.4 · The observed p-value as a function of the branching fraction of $Z \to \mu\tau$ for the CLs, CLb and CL$s + b$ hypotheses for the complete unblinded 2012 dataset together with the expectation by the used background model. The intersection of the $p = 0.05$ line and the CLs curve denotes the found 95% upper limit. The top plot shows the result for $Z \to \mu\tau$, the bottom for $Z \to e\tau$.

Table 6.3 · The expected and observed 95% C.L. exclusion limits as well as the best fit values for the branching ratio of $Z \to \mu\tau$ and $Z \to l\tau$ are shown for SR1, SR2 and the combined fit. To calculate these quantities for SR1 and SR2, the signal strengths are decorrelated in the signal regions and set to zero in the control regions.

Br$(Z \to \mu\tau)[10^{-5}]$	SR1	SR2	Combined
Expected limit	$2.6^{+1.1}_{-0.7}$	$6.4^{-1.8}_{+2.8}$	$2.6^{+1.1}_{-0.7}$
Observed limit	1.5	7.9	1.7
Best fit	$-2.1^{+1.2}_{-1.3}$	$2.6^{+2.9}_{-2.6}$	$-1.6^{+1.3}_{-1.4}$
Br$(Z \to e\tau)[10^{-5}]$	SR1	SR2	Combined
Expected limit	$4.8^{+1.8}_{-1.3}$	$13.3^{-3.7}_{+6.3}$	$4.3^{+1.7}_{-1.2}$
Observed limit	4.3	21.3	4.7
Best fit	$-1.2^{+2.9}_{-2.9}$	$9.1^{+6.8}_{-6.0}$	$0.6^{+2.2}_{-2.3}$

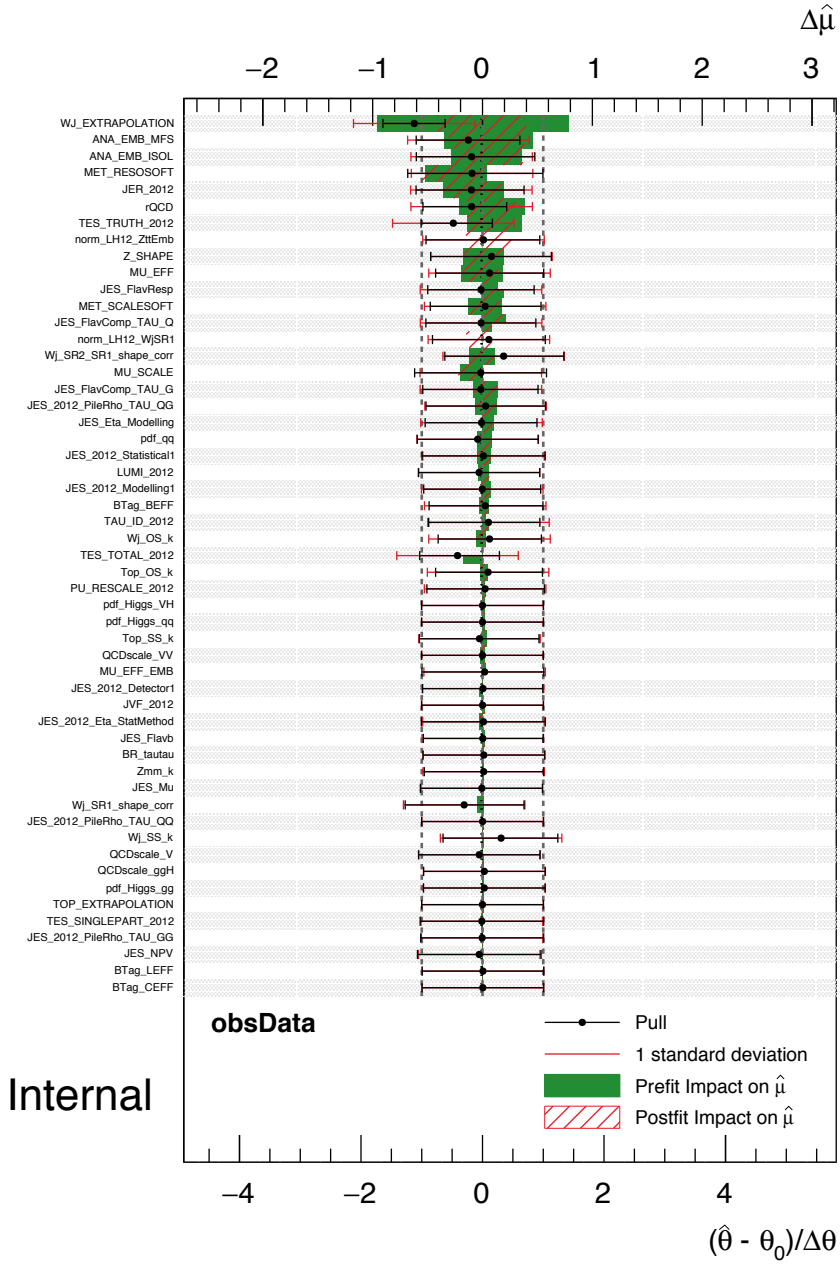

Fig. 6.5 · The pull and impact of the nuisance parameters before and after minimising the fit model to the unblinded dataset for the $Z \to \mu\tau$ channel.

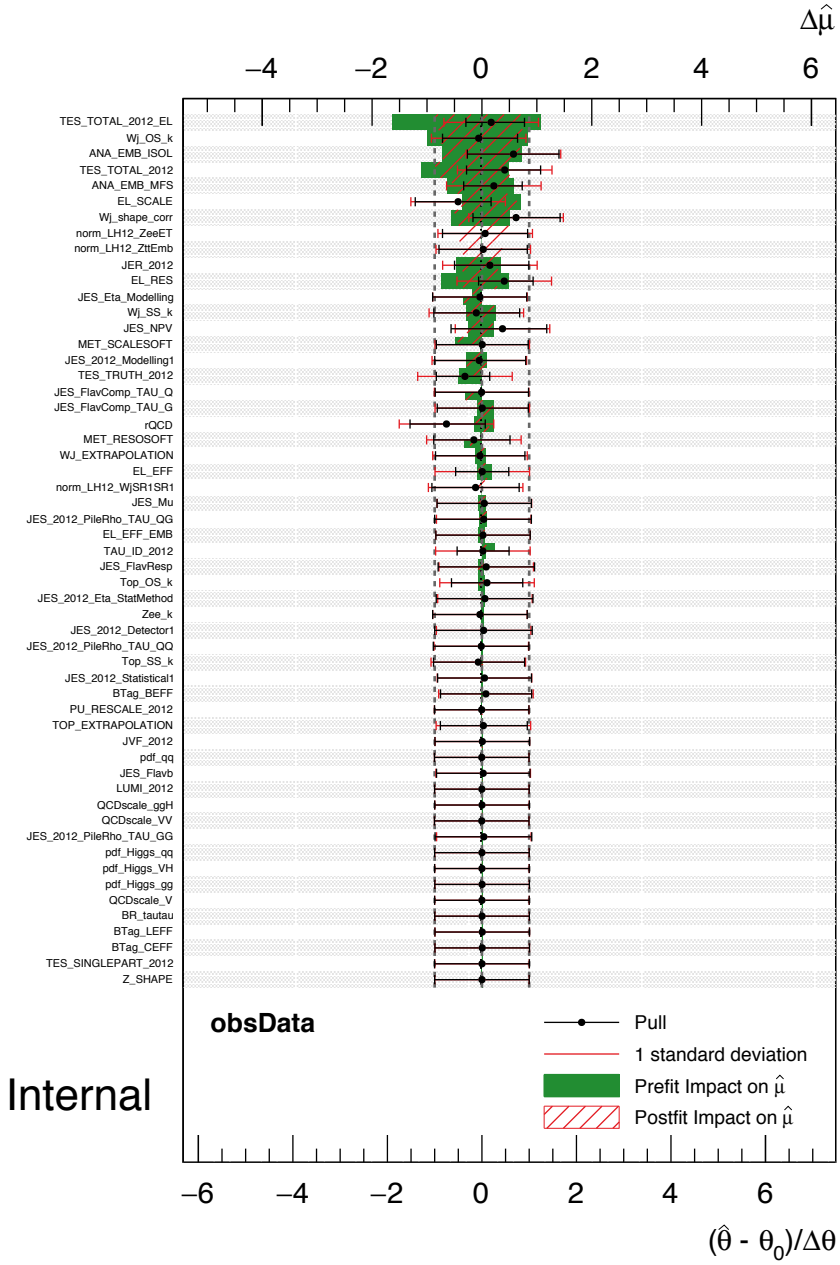

Fig. 6.6 · The pull and impact of the nuisance parameters before and after minimising the fit model to the unblinded dataset for the $Z \to e\tau$ channel.

Conclusion

Searches for lepton–flavour–violating decays of the Z bosons are performed using a data sample of proton–proton collisions recorded by the ATLAS detector at the LHC corresponding to an integrated luminosity of $\mathcal{L} = 20.3 fb^{-1}$ at $\sqrt{s} = 8$ TeV. Two LFV decays are considered: $Z \to \mu\tau$ and $Z \to e\tau$. The search for the LFV decays of the Z boson is performed with in the final state the τ-lepton decaying into hadrons. No significant excess is observed, and upper limits on the LFV branching ratios are set.

A small deficit of data compared to the predicted background is observed in the search for the LFV $Z \to \mu\tau$ decays. The observed and the median expected 95% CL upper limits on Br($Z \to \mu\tau$) are 1.7×10^{-5} and $2.6^{+2.1}_{-0.7} \times 10^{-5}$, respectively. The observed and the median expected upper limits on Br($Z \to e\tau$) are 4.7×10^{-5} and $4.3^{+1.7}_{-1.2} \times 10^{-5}$, respectively.

chapter seven

Summary

We see quarks and neutrinos change flavour as is codified in the CKM and PMNS mixing matrices. However, flavour violation of the charged leptons has never been observed. There is a strong motivation to search for these processes though, as they can possibly explain the matter and anti–matter asymmetry and the physics behind the neutrino masses. Many theoretical models predict a sizeable branching fraction of lepton–flavour–violating (LFV) decays of the Z bosons, up to current upper limits, making them interesting channels to probe for new physics.

Collider experiments are well suited to look at the production of leptons, and the high amount of integrated luminosity of the Large Hadron Collider gives rise to a new opportunity to search for these LFV decays, despite the fact that pile-up and the underlying event make it a more challenging environment than previous searches done at the LEP electron–positron collider.

The analyses in this thesis use recorded proton–proton collisions by the ATLAS experiment, the largest collider-detector ever constructed. Two LFV decays are considered: $Z \rightarrow \mu\tau$ and $Z \rightarrow e\tau$, by looking at the presence of an energetic lepton originating directly from the Z boson decay and carrying roughly half of its energy, and the hadronic products of a τ–lepton.

The analyses are performed on $\mathcal{L} = 20.3\,\text{fb}^{-1}$ of $\sqrt{s} = 8$ TeV data collected by ATLAS in 2012, after a stringent selection is applied to reduce the number of events originating from background events. A binned likelihood model with the invariant mass of the Z as the discriminating observable has been constructed with a combination of Monte Carlo and data–driven techniques. The branching fractions of the $Z \rightarrow l\tau$ decays are then extracted from the likelihood minimisation, by comparing the observed data to the sum of the expected backgrounds while taking into account the various systematic uncertainties.

No significant excess is observed, and upper limits on the LFV branching ratios are set. A small deficit of data compared to the predicted background is observed in the muon channel. The observed (expected) 95% CL upper limit on Br($Z \rightarrow \mu\tau$) is 1.7×10^{-5} ($2.6^{+2.1}_{-0.7} \times 10^{-5}$). In the electron channel the observed data is very close to the background prediction, with the observed (expected) upper limit on Br($Z \rightarrow e\tau$) being 4.7×10^{-5} ($4.3^{+1.7}_{-1.2} \times 10^{-5}$).

In conclusion, no significant deviation from the Standard Model has been found. The measured upper limits are not yet competitive with the searches performed at the LEP collider. However the increase in statistics in the coming years

should make it easily possible to probe these channels at higher sensitivities, creating an exciting opportunity to find new physics.

Samenvatting

We zien quarks en neutrinos veranderen van type zoals beschreven staat in de CKM en PMNS matrices. Voor geladen leptonen is dit echter nog nooit waargenomen. Het is wel interessant om naar deze processen te zoeken, omdat ze mogelijk de materie en anti-materie onbalans en de massa van de neutrinos kunnen verklaren. Meerdere theoretische modellen voorspellen een versterking van de zogenaamde lepton-type-veranderende (LTV) vervallen van het Z boson, tot op de huidige waargenomen experimentele limieten, wat ze tot een uitstekende test maken voor nieuwe natuurkunde.

Deeltjesversnellers zijn uitermate geschikt om naar de productie van leptonen te kijken. Daarnaast geeft de grote hoeveelheid geïntegreerde luminositeit van de Large Hadron Collider een nieuwe kans om naar deze LTV vervallen te zoeken, ondanks het feit dat het een uitdagenderende omgeving is dan de LEP electron-positron versneller uit het verleden.

De analyses beschreven in dit proefschrift maken gebruik van de proton-proton botsingen geregistreerd door het ATLAS experiment, de grootste detector aan een deeltjesversneller ooit gebouwd. Twee LTV vervallen worden behandeld: $Z \to \mu\tau$ en $Z \to e\tau$, door te zoeken naar een energetische lepton die geproduceerd wordt bij het verval van een Z boson, en de hadronische vervalproducten van een τ–lepton.

De analyses maken gebruik van $\mathcal{L} = 20.3\,\text{fb}^{-1}$ aan data met $\sqrt{s} = 8$ TeV die door ATLAS is verzameld in 2012, nadat een strenge selectie de oninteressante botsingen van andere achtergrond processen sterk reduceert. Een statistisch model met de invariante massa van de Z boson als discriminerende observabele is gebouwd met een combinatie van Monte Carlo en data-gedreven technieken. De fractie van de $Z \to l\tau$ vervallen wordt dan vervolgens gemeten door een sjabloon-fittingmethode, door de waargenomen data te vergelijken met de voorspelde achtergronden, waarbij rekening wordt gehouden met de verschillende systematische onzekerheden.

Er is geen significant signaal waargenomen en de bovengrenzen op de LTV vervallen zijn berekend. In het muonkanaal is iets minder data waargenomen dan verwacht op basis van de achtergrondprocessen. De waargenomen (verwachte) bovengrens voor Br($Z \to \mu\tau$) is 1.7×10^{-5} ($2.6^{+2.1}_{-0.7} \times 10^{-5}$) met een 95 % betrouwbaarheidsniveau. In het electronkanaal ligt de geobserveerde data heel dicht bij de voorspelling, met een waargenomen (verwachte) bovengrens op Br($Z \to e\tau$) van 4.7×10^{-5} ($4.3^{+1.7}_{-1.2} \times 10^{-5}$).

Concluderend zijn er geen significante afwijkingen van het Standaard Model waargenomen. De gemeten bovengrenzen zijn nog niet concurrerend met de eerdere zoektochten die verricht zijn bij de LEP versneller. Maar de grote hoeveelheden protonbotsingen die de komende jaren nog gemeten gaan worden, komt daar zeker

verandering in. Dat biedt een spannende mogelijkheid om nieuwe fysica te ontdekken.

appendix one

Additional plots

This appendix shows additional plots and tables mentioned in the thesis: the correlation matrix of the nine nuisance parameters which have the highest correlation with the signal strength in figure A.1, additional pull and ranking plots in figure A.2, a summary of the systematic uncertainties that were considered and applied to SR1 for the $Z \rightarrow \mu\tau$ channel in table A.1 and the names and their description of the systematic uncertainties used in the fit model in tables A.2 and A.3.

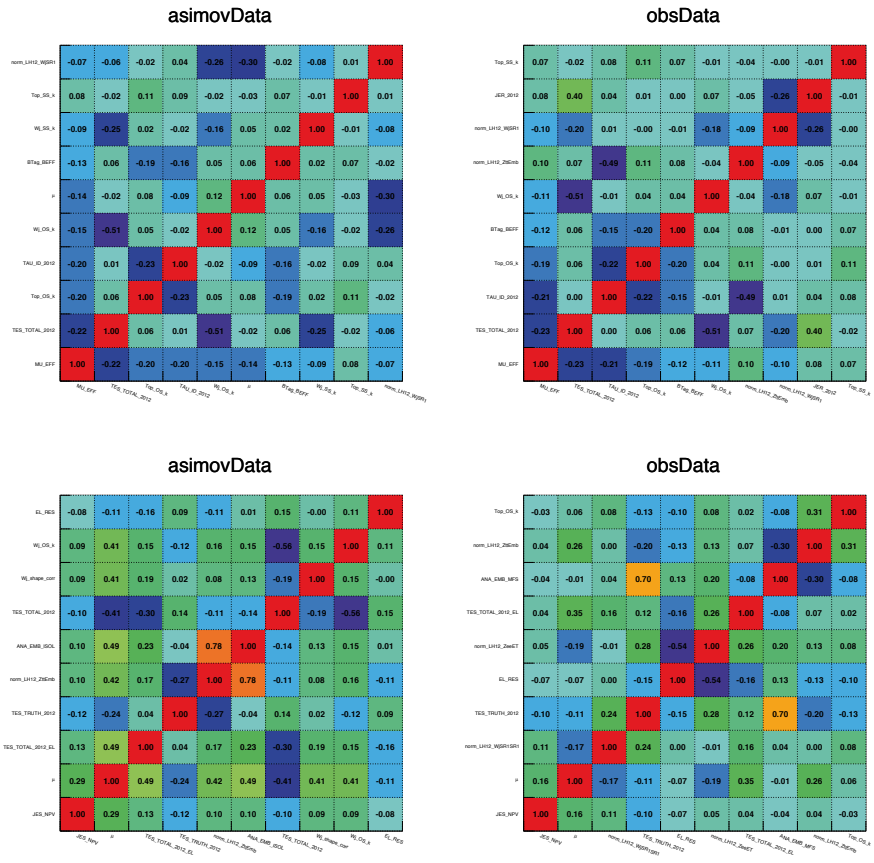

Fig. A.1 · The correlation matrix of the nine nuisance parameters which have the highest correlation with the signal strength μ. On the left the result on the Asimov dataset is shown and gives the prediction from the fit-model. On the right the result on the hybrid dataset is shown.

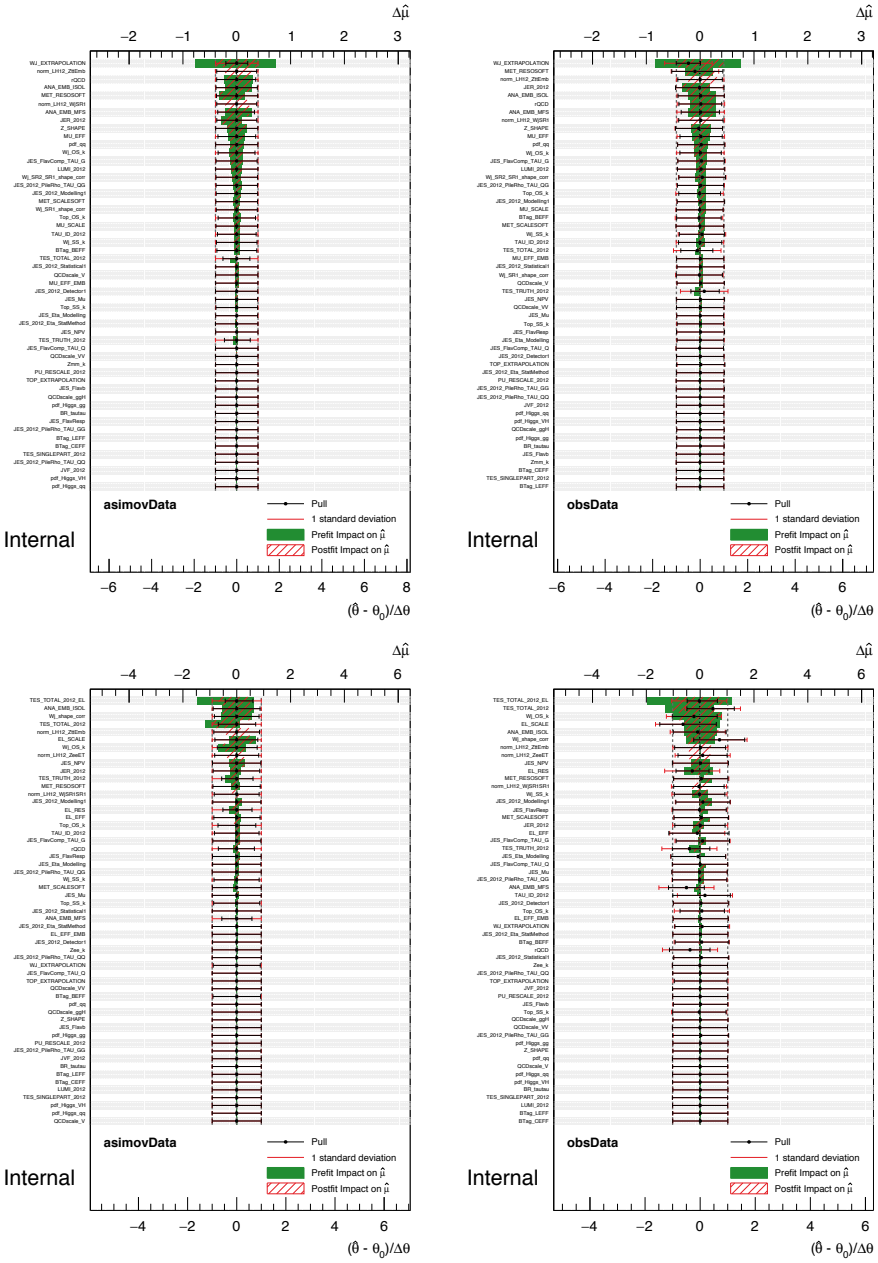

Fig. A.2 · The pull and impact of the nuisance parameters before and after running the fit. The results for the Asimov dataset is shown on the left and for the hybrid dataset on the right.

Systematic	$Z \to \mu\tau$	$H \to \tau\tau$	$Z \to \tau\tau$	W + jets	$t/t\bar{t}$	SS data	$Z/VV \to ll$
MU_SCALE	S	-	-	N	N	-	-
TES_TRUTH_2012	NS	N	N	-	N	-	N
TES_SINGLEPART_2012	-	N	-	-	N	-	-
TES_TOTAL_2012	-	-	-	NS	N	-	N
JER_2012	NS	-	-	N	N	-	N
JES_Flavb	-	-	-	-	N	-	-
JES_2012_Detector1	-	-	-	-	N	-	N
JES_2012_Eta_StatMethod	-	-	-	-	N	-	-
JES_Eta_Modelling	S	N	-	-	N	-	N
JES_FlavComp_TAU_Q	S	-	-	-	N	-	N
JES_FlavComp_TAU_G	-	N	-	N	-	-	N
JES_FlavResp	S	-	-	-	N	-	N
JES_2012_Modelling1	S	N	-	-	N	-	N
JES_Mu	-	-	-	-	-	-	-
JES_NPV	-	-	-	-	N	-	N
JES_2012_PileRho_TAU_QQ	-	-	-	-	-	-	-
JES_2012_PileRho_TAU_QG	-	-	-	-	-	-	N
JES_2012_PileRho_TAU_GG	-	-	-	-	N	-	-
JES_2012_Statistical1	-	-	-	-	N	-	-
JVF_2012	-	-	-	-	-	-	-
MET_RESOSOFT	S	-	-	S	N	-	N
MET_SCALESOFT	S	N	-	-	N	-	N
MU_EFF	N	N	-	N	N	-	N
MU_EFF_Emb	-	-	N	-	-	-	-
TAU_FAKE_2012	-	-	-	-	-	-	-
PU_RESCALE_2012	NS	-	-	-	-	-	-
TAU_ID_2012	N	N	N	-	N	-	-
BTag_BEFF	-	-	-	-	N	-	-
BTag_CEFF	-	-	-	-	-	-	-
BTag_LEFF	-	-	-	-	-	-	-
Z_SHAPE	-	-	-	-	-	-	N
TOP_EXTRAPOLATION	-	-	-	-	N	-	-
WJ_EXTRAPOLATION	-	-	N	NS	-	-	-
Wj_SR1_shape_corr	-	-	-	S	-	-	-
Wj_SR2_SR1_shape_corr	-	-	-	-	-	-	-
ANA_EMB_ISOL	-	-	N	-	-	-	-
ANA_EMB_MFS	-	-	NS	-	-	-	-
BR_tautau	-	N	-	-	-	-	-
pdf_Higgs_gg	-	N	-	-	-	-	-
QCDscale_ggH	-	N	-	-	-	-	-
pdf_Higgs_qq	-	-	-	-	-	-	-
QCDscale_qqH	-	-	-	-	-	-	-
pdf_Higgs_VH	-	-	-	-	-	-	-
QCDscale_VH	-	-	-	-	-	-	-
QCDscale_V	N	-	-	-	-	-	N
pdf_qq	N	-	-	-	-	-	N
QCDscale_VV	-	-	-	-	-	-	N
rQCD	-	-	-	NS	NS	N	NS
LUMI_2012	N	N	-	-	-	-	N
Zmm_k	-	-	-	-	-	-	-
Wj_OS_k	-	-	-	NS	-	-	-
Wj_SS_k	-	-	-	NS	-	-	-
Top_OS_k	-	-	-	-	NS	-	-
Top_SS_k	-	-	-	-	NS	-	-

Table A.1 · A summary of the systematic uncertainties that were considered and applied to SR1 for the $Z \to \mu\tau$ channel. The uncertainties that pass the criteria of having a large enough impact on the prediction of a template are denoted with a 'N' and or an 'S'. 'N' means that the particular systematic is included as a normalisation uncertainty, 'S' that the shape difference is taken into account, and 'NS' both.

Table A.2 · The names and their description of the systematic uncertainties used in the fit model.

Nuiscance parameter	description
EMB_ISOL	embedding isolation systematic
EMB_MFS	embedding muon cell energy subtraction systematic
rQCD	R_{QCD} uncertainty
Top_OS_k	normalization uncertainty for OS top events
Top_SS_k	normalization uncertainty for SS top events
Wj_OS_k	normalization uncertainty for OS W+jets events
Wj_SS_k	normalization uncertainty for SS W+jets events
WJ_SR1_SHAPE	shape uncertainty due to W+jets re-weighting in SR1
WJ_SR2_SR1_SHAPE	shape uncertainty due to W+jets re-weighting in SR2
TOP_EXTRAPOLATION	extrapolation uncertainty for top background
WJ_EXTRAPOLATION	extrapolation uncertainty for W+jets background
Z_SHAPE	reweighting systematic for $Z \to ll\,(j \to \tau_{\text{fake}})$ events
BTag_BEFF	uncertainty on b-tagging efficiency (b-jets)
BTag_CEFF	uncertainty on b-tagging efficiency (c-jets)
BTag_LEFF	uncertainty on b-tagging efficiency (light-jets)
JVF_2012	systematics on jet-vertex-fraction cut
LUMI_2012	systematics on measured integrated luminosity in 2012
TAU_ID_2012	uncertainty for tau identification efficiency
TES_TOTAL_2012	uncertainty on tau energy scale for fake candidates
TES_INSITU_2012	uncertainty on *in situ* tau energy scale
TES_TRUTH_2012	TES uncertainty component for true candidates
JER_2012	uncertainty on jet energy resolution
JES_2012_Detector1	JES uncertainty component
JES_2012_Eta_StatMethod	JES uncertainty component
JES_2012_Modelling1	JES uncertainty component
JES_2012_PileRho_TAU_GG	JES uncertainty component, applies to Top and $gg \to H$
JES_2012_PileRho_TAU_QG	JES uncertainty component, applies to W+jets and Z+jets
JES_2012_PileRho_TAU_QQ	JES uncertainty component, applies to VBF Higgs, VV, WH, ZH
JES_2012_Statistical1	JES uncertainty component
JES_Eta_Modelling	JES uncertainty component

Table A.3 · The names and their description of the systematic uncertainties used in the fit model.

Nuiscance parameter	description
JES_2012_PileRho_TAU_GG	JES uncertainty component, applies to Top and $gg \to H$
JES_2012_PileRho_TAU_QG	JES uncertainty component, applies to W+jets and Z+jets
JES_2012_PileRho_TAU_QQ	JES uncertainty component, applies to VBF Higgs, VV, WH, ZH
JES_2012_Statistical1	JES uncertainty component
JES_Eta_Modelling	JES uncertainty component
JES_FlavComp_TAU_G	JES uncertainty component, applies to $gg \to H$, W+jets and Z+jets
JES_FlavComp_TAU_Q	JES uncertainty component, applies to Top, VBF Higgs, VV, WH, ZH
JES_FlavResp	JES uncertainty component
JES_Flavb	JES uncertainty component
JES_Mu	JES uncertainty component
JES_NPV	JES uncertainty component
MET_RESOSOFT	MET resolution uncertainty on the soft term
MET_SCALESOFT	MET scale uncertainty on the soft term
MU_EFF	muon trigger and identification efficiency uncertainty
MU_EFF_Emb	muon trigger and identification efficiency uncertainty for embedding
MU_SCALE	muon momentum scale uncertainty
PU_rescaling	pileup reweighting uncertainty
BR_tautau	uncertainty on $H \to \tau\tau$ BR
QCDscale_V	uncertainty for W/Z+jets acceptance from QCD scale
QCDscale_VH	uncertainty for VH acceptance from QCD scale
QCDscale_ggH	uncertainty for $gg \to H$ (inclusive) acceptance from QCD scale
QCDscale_qqH	uncertainty for VBF acceptance from QCD scale
pdf_Higgs_gg	PDF uncertainty on ggF production
pdf_Higgs_qq	PDF uncertainty on VBF production
pdf_Higgs_VH	PDF uncertainty on VH production
pdf_qq	PDF uncertainty on MC-based background samples

Bibliography

[1] Charles Bukowski. The captain is out to lunch and the sailors have taken over the ship, 1998. (Cited on page v.)

[2] G. Arnison et al. Experimental Observation of Isolated Large Transverse Energy Electrons with Associated Missing Energy at s**(1/2) = 540-GeV. *Phys. Lett.*, B122:103–116, 1983. [,611(1983)]. (Cited on pages 1 and 23.)

[3] M. Banner et al. Observation of Single Isolated Electrons of High Transverse Momentum in Events with Missing Transverse Energy at the CERN anti-p p Collider. *Phys. Lett.*, B122:476–485, 1983. (Cited on pages 1 and 23.)

[4] K. A. Olive et al. Review of Particle Physics. *Chin. Phys.*, C38:090001, 2014. (Cited on pages 1, 5, 11, 12, 14, 42, and 44.)

[5] Robert H. Bernstein and Peter S. Cooper. Charged Lepton Flavor Violation: An Experimenter's Guide. *Phys. Rept.*, 532:27–64, 2013. (Cited on pages 2 and 16.)

[6] S. L. Glashow. Partial Symmetries of Weak Interactions. *Nucl. Phys.*, 22:579–588, 1961. (Cited on page 5.)

[7] Steven Weinberg. A Model of Leptons. *Phys. Rev. Lett.*, 19:1264–1266, 1967. (Cited on page 5.)

[8] A. Salam. Weak and electromagnetic interactions - in elementary particle theory: relativistic groups and analyticity, 1968. (Cited on page 5.)

[9] S. L. Glashow, J. Iliopoulos, and L. Maiani. Weak Interactions with Lepton-Hadron Symmetry. *Phys. Rev.*, D2:1285–1292, 1970. (Cited on page 5.)

[10] Nicola Cabibbo. Unitary Symmetry and Leptonic Decays. *Phys. Rev. Lett.*, 10:531–533, 1963. [,648(1963)]. (Cited on page 8.)

[11] Makoto Kobayashi and Toshihide Maskawa. CP Violation in the Renormalizable Theory of Weak Interaction. *Prog. Theor. Phys.*, 49:652–657, 1973. (Cited on page 8.)

[12] Ling-Lie Chau and Wai-Yee Keung. Comments on the Parametrization of the Kobayashi-Maskawa Matrix. *Phys. Rev. Lett.*, 53:1802, 1984. (Cited on page 8.)

[13] Marcella Bona et al. The 2004 UTfit collaboration report on the status of the unitarity triangle in the standard model. *JHEP*, 07:028, 2005. (Cited on page 9.)

[14] Georges Aad et al. Observation of a new particle in the search for the Standard Model Higgs boson with the ATLAS detector at the LHC. *Phys. Lett.*, B716:1–29, 2012. (Cited on pages 9 and 20.)

[15] Serguei Chatrchyan et al. Observation of a new boson at a mass of 125 GeV with the CMS experiment at the LHC. *Phys. Lett.*, B716:30–61, 2012. (Cited on pages 9 and 20.)

[16] M.C. Gonzalez-Garcia and Michele Maltoni. Phenomenology with Massive Neutrinos. *Phys.Rept.*, 460:1–129, 2008. (Cited on page 9.)

[17] Elena Giusarma, Roland de Putter, Shirley Ho, and Olga Mena. Constraints on neutrino masses from Planck and Galaxy Clustering data. *Phys.Rev.*, D88(6):063515, 2013. (Cited on page 9.)

[18] M. C. Gonzalez-Garcia and Michele Maltoni. Phenomenology with Massive Neutrinos. *Phys. Rept.*, 460:1–129, 2008. (Cited on page 9.)

[19] M. C. Gonzalez-Garcia, Michele Maltoni, Jordi Salvado, and Thomas Schwetz. Global fit to three neutrino mixing: critical look at present precision. *JHEP*, 12:123, 2012. (Cited on pages 9 and 10.)

[20] Patrick Huber. On the determination of anti-neutrino spectra from nuclear reactors. *Phys. Rev.*, C84:024617, 2011. [Erratum: Phys. Rev.C85,029901(2012)]. (Cited on page 10.)

[21] Olga Mena and Stephen J. Parke. Unified graphical summary of neutrino mixing parameters. *Phys. Rev.*, D69:117301, 2004. (Cited on page 11.)

[22] Marco Drewes. The Phenomenology of Right Handed Neutrinos. *Int. J. Mod. Phys.*, E22:1330019, 2013. (Cited on page 15.)

[23] Peter Minkowski. $\mu \to e\gamma$ at a Rate of One Out of 10^9 Muon Decays? *Phys. Lett.*, B67:421–428, 1977. (Cited on page 15.)

[24] Pavel Fileviez Perez, Tao Han, Gui-yu Huang, Tong Li, and Kai Wang. Neutrino Masses and the CERN LHC: Testing Type II Seesaw. *Phys. Rev.*, D78:015018, 2008. (Cited on page 15.)

[25] http://www.ecap.physik.uni-erlangen.de/nexo/research.shtml. (Cited on page 15.)

[26] Alberto Garfagnini. Neutrinoless Double Beta Decay Experiments. In *12th Conference on Flavor Physics and CP Violation (FPCP 2014) Marseille, France, May 26-30, 2014*, 2014. (Cited on page 15.)

[27] J I Illana, M Jack, and Tord Riemann. Predictions for $Z \to \mu\tau$ and Related Reactions,hep-ph/0001273. desy-99-165. ug-ft-112. lc-th-2000-007. (hep-ph/0001273. DESY-99-165. UG-FT-112. LC-TH-2000-007):34 p, Jan 2000. (Cited on page 16.)

[28] Sacha Davidson, Sylvain Lacroix, and Patrice Verdier. LHC sensitivity to lepton flavour violating Z boson decays. *JHEP*, 09:092, 2012. (Cited on page 16.)

[29] David Delepine and Francesco Vissani. Indirect bounds on Z —> muon e and lepton flavor violation at future colliders. *Phys. Lett.*, B522:95–101, 2001. (Cited on page 16.)

[30] S. Nussinov, R. D. Peccei, and X. M. Zhang. On unitarity based relations between various lepton family violating processes. *Phys. Rev.*, D63:016003, 2001. (Cited on page 16.)

[31] A. Flores-Tlalpa, J. M. Hernandez, G. Tavares-Velasco, and J. J. Toscano. Effective Lagrangian description of the lepton flavor violating decays $Z \to l_i^{\mp} l_j^{\pm}$. *Phys. Rev.*, D65:073010, 2002. (Cited on pages 16 and 17.)

[32] P. Abreu et al. Search for lepton flavor number violating Z0 decays. *Z. Phys.*, C73:243–251, 1997. (Cited on page 17.)

[33] R. Akers et al. A Search for lepton flavor violating Z0 decays. *Z. Phys.*, C67:555–564, 1995. (Cited on page 17.)

[34] A. D. Sakharov. Violation of CP Invariance, c Asymmetry, and Baryon Asymmetry of the Universe. *Pisma Zh. Eksp. Teor. Fiz.*, 5:32–35, 1967. [Usp. Fiz. Nauk161,61(1991)]. (Cited on page 17.)

[35] M. Fukugita and T. Yanagida. Baryogenesis Without Grand Unification. *Phys. Lett.*, B174:45, 1986. (Cited on page 17.)

[36] Murray Gell-Mann, Pierre Ramond, and Richard Slansky. Complex Spinors and Unified Theories. *Conf. Proc.*, C790927:315–321, 1979. (Cited on page 18.)

[37] Osamu Sawada and Akio Sugamoto, editors. *Proceedings: Workshop on the Unified Theories and the Baryon Number in the Universe*, Tsukuba, Japan, 1979. Natl.Lab.High Energy Phys., Natl.Lab.High Energy Phys. (Cited on page 18.)

[38] Tsutomu Yanagida. HORIZONTAL SYMMETRY AND MASSES OF NEUTRINOS. *Conf. Proc.*, C7902131:95–99, 1979. (Cited on page 18.)

[39] Jose I. Illana and T. Riemann. Charged lepton flavor violation from massive neutrinos in Z decays. *Phys. Rev.*, D63:053004, 2001. (Cited on page 19.)

[40] Gordon L. Kane and Mikhail A. Shifman. Introduction to 'the supersymmetric world: The Beginnings of the theory'. *hep-ph/0102298*, 2001. (Cited on page 18.)

[41] Stephen P. Martin. A Supersymmetry primer. 1997. [Adv. Ser. Direct. High Energy Phys.18,1(1998)]. (Cited on page 19.)

[42] John Ellis. The Physics Landscape after the Higgs Discovery at the LHC. In *10th Latin American Symposium on High Energy Physics (SILAFAE 2014) Medellin, Colombia, November 24-28, 2014*, 2015. (Cited on page 19.)

[43] Jin Min Yang. Lepton flavor violating Z-boson decays at GigaZ as a probe of supersymmetry. *Sci. China Phys. Mech. Astron.*, 53:1949–1952, 2010. (Cited on pages 19 and 20.)

[44] Georges Aad et al. Search for lepton-flavour-violating $H \to \mu\tau$ decays of the Higgs boson with the ATLAS detector. *JHEP*, 11:211, 2015. (Cited on page 20.)

[45] Vardan Khachatryan et al. Search for Lepton-Flavour-Violating Decays of the Higgs Boson. *Phys. Lett.*, B749:337–362, 2015. (Cited on page 20.)

[46] R. Benbrik, Chuan-Hung Chen, and Takaaki Nomura. $h, Z \to \ell_i \bar{\ell}_j$, Δa_μ, $\tau \to (3\mu, \mu\gamma)$ in generic two-Higgs-doublet models. 2015. (Cited on page 21.)

[47] http://home.web.cern.ch/about/member-states. (Cited on page 23.)

[48] ATLAS collaboration. http://public-archive.web.cern.ch/public-archive/en/About/Nobels-en.html. (Cited on page 23.)

[49] Nobel Prize Committee. https://www.nobelprize.org/nobel_prizes/lists/universities.html. (Cited on page 23.)

[50] The document that officially put the World Wide Web into the public domain on 30 April 1993. Apr 1993. (Cited on page 23.)

[51] http://www.newscientist.com/article/dn19407-innovation-cern-collides-with-a-patent-reality.html. (Cited on page 23.)

[52] G. Abbiendi et al. Precise determination of the Z resonance parameters at LEP: 'Zedometry'. *Eur. Phys. J.*, C19:587–651, 2001. (Cited on page 23.)

[53] Lyndon Evans and Philip Bryant. LHC Machine. *JINST*, 3:S08001, 2008. (Cited on page 23.)

[54] http://www.lhc-closer.es/taking_a_closer_look_at_lhc/0.proton_source. (Cited on page 24.)

[55] C Lefevre. LHC: the guide, http://cds.cern.ch/record/1165534, Feb 2009. (Cited on pages 24, 25, and 26.)

[56] K. Aamodt et al. The ALICE experiment at the CERN LHC. *JINST*, 3:S08002, 2008. (Cited on page 25.)

[57] G. Aad et al. The ATLAS Experiment at the CERN Large Hadron Collider. *JINST*, 3:S08003, 2008. (Cited on pages 25, 27, 29, 30, 32, and 33.)

[58] S. Chatrchyan et al. The CMS experiment at the CERN LHC. *JINST*, 3:S08004, 2008. (Cited on page 25.)

[59] A. Augusto Alves, Jr. et al. The LHCb Detector at the LHC. *JINST*, 3:S08005, 2008. (Cited on page 25.)

[60] O. Adriani et al. The LHCf detector at the CERN Large Hadron Collider. *JINST*, 3:S08006, 2008. (Cited on page 25.)

[61] G. Anelli et al. The TOTEM experiment at the CERN Large Hadron Collider. *JINST*, 3:S08007, 2008. (Cited on page 25.)

[62] http://atlas.cern/discover/collaboration. (Cited on page 25.)

[63] Joao Pequenao and Paul Schaffner. An computer generated image representing how ATLAS detects particles. Jan 2013. (Cited on page 28.)

[64] Vasiliki A. Mitsou. The ATLAS transition radiation tracker. In *Astroparticle, particle and space physics, detectors and medical physics applications. Proceedings, 8th Conference, ICATPP 2003, Como, Italy, October 6-10, 2003*, pages 497–501, 2003. (Cited on page 31.)

[65] CERN press office. http://press.cern/press-releases/2008/10/cern-releases-analysis-lhc-incident. (Cited on page 34.)

[66] AtlasTWiki RunStatsPublicResults2012. https://twiki.cern.ch/twiki/bin/view/AtlasPublic/RunStatsPublicResults2012. (Cited on pages 34 and 36.)

[67] ATLAS collaboration. https://atlas.web.cern.ch/Atlas/GROUPS/DATAPREPARATION/DataSummary/2012/. (Cited on page 35.)

[68] Georges Aad et al. Measurement of the muon reconstruction performance of the ATLAS detector using 2011 and 2012 LHC proton–proton collision data. *Eur. Phys. J.*, C74(11):3130, 2014. (Cited on page 38.)

[69] Electron efficiency measurements with the ATLAS detector using the 2012 LHC proton-proton collision data. Technical Report ATLAS-CONF-2014-032, CERN, Geneva, Jun 2014. (Cited on pages 39 and 40.)

[70] W. Lampl, S. Laplace, D. Lelas, P. Loch, H. Ma, S. Menke, S. Rajagopalan, D. Rousseau, S. Snyder, and G. Unal. Calorimeter clustering algorithms: Description and performance. 2008. (Cited on page 39.)

[71] Matteo Cacciari, Gavin P. Salam, and Gregory Soyez. The Anti-k(t) jet clustering algorithm. *JHEP*, 04:063, 2008. (Cited on pages 39 and 41.)

[72] The ATLAS collaboration. Monte Carlo Calibration and Combination of In-situ Measurements of Jet Energy Scale, Jet Energy Resolution and Jet Mass in ATLAS. Technical Report ATLAS-CONF-2015-037, CERN, Geneva, Aug 2015. (Cited on page 42.)

[73] The ATLAS collaboration. Commissioning of the ATLAS high-performance b-tagging algorithms in the 7 TeV collision data. Technical Report ATLAS-CONF-2011-102, CERN, Geneva, Jul 2011. (Cited on page 42.)

[74] The ATLAS collaboration. Calibration of the performance of b-tagging for c and light-flavour jets in the 2012 ATLAS data. Technical Report ATLAS-CONF-2014-046, CERN, Geneva, Jul 2014. (Cited on pages 42 and 43.)

[75] Antonio Pich. Precision Tau Physics. *Prog. Part. Nucl. Phys.*, 75:41–85, 2014. (Cited on pages 43 and 45.)

[76] Georges Aad et al. Identification and energy calibration of hadronically decaying tau leptons with the ATLAS experiment in pp collisions at $\sqrt{s}$=8 TeV. *Eur. Phys. J.*, C75(7):303, 2015. (Cited on pages 44, 45, and 46.)

[77] The ATLAS collaboration. Reconstruction and Performance of Missing Transverse Momentum in the ATLAS Detector using Proton-Proton Collisions at $\sqrt{s} = 8$ TeV. *In preparation*. (Cited on pages 47, 48, and 49.)

[78] Matteo Cacciari, Gavin P. Salam, and Gregory Soyez. The Catchment Area of Jets. *JHEP*, 04:005, 2008. (Cited on page 47.)

[79] John Philip Ottersbach. Muons in early atlas data: from first collisions to w^+w^- production. *thesis*, 2012. (Cited on page 52.)

[80] A Andreazza et al. Search for Standard Model $H \to \tau^+\tau^- \to \ell\tau_h$ with the ATLAS Detector in 8TeV Proton-Proton Collisions. Technical Report ATL-COM-PHYS-2013-1494, CERN, Geneva, Nov 2013. (Cited on pages 53, 54, 64, 66, 84, and 95.)

[81] Georges Aad et al. Measurement of the electroweak production of dijets in association with a Z-boson and distributions sensitive to vector boson fusion in proton-proton collisions at $\sqrt{s} = 8$ TeV using the ATLAS detector. *JHEP*, 04:031, 2014. (Cited on page 53.)

[82] Georges Aad et al. Measurement of hard double-parton interactions in $W(\to l\nu)$+ 2 jet events at $\sqrt{s}$=7 TeV with the ATLAS detector. *New J. Phys.*, 15(arXiv:1301.6872. CERN-PH-EP-2012-355):033038. 46 p, Jan 2013. (Cited on page 54.)

[83] F. Abe et al. Observation of top quark production in $\bar{p}p$ collisions. *Phys. Rev. Lett.*, 74:2626–2631, 1995. (Cited on page 54.)

[84] S. Abachi et al. Search for high mass top quark production in $p\bar{p}$ collisions at $\sqrt{s} = 1.8$ TeV. *Phys. Rev. Lett.*, 74:2422–2426, 1995. (Cited on page 54.)

[85] Georges Aad et al. Measurement of jet shapes in top-quark pair events at $\sqrt{s}$ = 7 TeV using the ATLAS detector. *Eur. Phys. J.*, C73(12):2676, 2013. (Cited on page 55.)

[86] Georges Aad et al. Search for anomalous couplings in the Wtb vertex from the measurement of double differential angular decay rates of single top quarks produced in the t-channel with the ATLAS detector. Technical Report CERN-PH-EP-2015-

236, 2015. (Cited on page 55.)

[87] M. G. Pia. The Geant4 Toolkit: Simulation capabilities and application results. *Nucl. Phys. Proc. Suppl.*, 125:60–68, 2003. [,60(2003)]. (Cited on page 55.)

[88] Paolo Nason. A New method for combining NLO QCD with shower Monte Carlo algorithms. *JHEP*, 11:040, 2004. (Cited on page 55.)

[89] Stefano Frixione and Bryan R. Webber. Matching NLO QCD computations and parton shower simulations. *JHEP*, 06:029, 2002. (Cited on pages 55 and 56.)

[90] Hung-Liang Lai, Marco Guzzi, Joey Huston, Zhao Li, Pavel M. Nadolsky, Jon Pumplin, and C. P. Yuan. New parton distributions for collider physics. *Phys. Rev.*, D82:074024, 2010. (Cited on page 55.)

[91] Torbjorn Sjostrand, Stephen Mrenna, and Peter Z. Skands. PYTHIA 6.4 Physics and Manual. *JHEP*, 05:026, 2006. (Cited on pages 55 and 56.)

[92] Michelangelo L. Mangano, Mauro Moretti, Fulvio Piccinini, Roberto Pittau, and Antonio D. Polosa. ALPGEN, a generator for hard multiparton processes in hadronic collisions. *JHEP*, 07:001, 2003. (Cited on pages 55 and 56.)

[93] J. Pumplin, D. R. Stump, J. Huston, H. L. Lai, Pavel M. Nadolsky, and W. K. Tung. New generation of parton distributions with uncertainties from global QCD analysis. *JHEP*, 07:012, 2002. (Cited on page 55.)

[94] G. Corcella, I. G. Knowles, G. Marchesini, S. Moretti, K. Odagiri, P. Richardson, M. H. Seymour, and B. R. Webber. HERWIG 6.5 release note. *CERN-TH-2002-270*, 2002. (Cited on page 56.)

[95] J. M. Butterworth, Jeffrey R. Forshaw, and M. H. Seymour. Multiparton interactions in photoproduction at HERA. *Z. Phys.*, C72:637–646, 1996. (Cited on page 56.)

[96] Borut Paul Kersevan and Elzbieta Richter-Was. The Monte Carlo event generator AcerMC versions 2.0 to 3.8 with interfaces to PYTHIA 6.4, HERWIG 6.5 and ARIADNE 4.1. *Comput. Phys. Commun.*, 184:919–985, 2013. (Cited on page 56.)

[97] T. Binoth, M. Ciccolini, N. Kauer, and M. Kramer. Gluon-induced W-boson pair production at the LHC. *JHEP*, 12:046, 2006. (Cited on page 56.)

[98] A. Elagin, P. Murat, A. Pranko, and A. Safonov. A New Mass Reconstruction Technique for Resonances Decaying to di-tau. *Nucl.Instrum.Meth.*, A654:481–489, 2011. (Cited on pages 56 and 57.)

[99] Georges Aad et al. Search for the Standard Model Higgs boson in the H to $\tau^+\tau^-$ decay mode in $\sqrt{s} = 7$ TeV pp collisions with ATLAS. *JHEP*, 09:070, 2012. (Cited on page 64.)

[100] Georges Aad et al. Measurement of the Z to tau tau Cross Section with the ATLAS Detector. *Phys. Rev.*, D84:112006, 2011. (Cited on page 64.)

[101] Glen Cowan, Kyle Cranmer, Eilam Gross, and Ofer Vitells. Asymptotic formulae for likelihood-based tests of new physics. *Eur. Phys. J.*, C71:1554, 2011. [Erratum: Eur. Phys. J.C73,2501(2013)]. (Cited on page 74.)

[102] Roostats. https://twiki.cern.ch/twiki/bin/view/RooStats/WebHome. (Cited on page 79.)

[103] G. Cowan, K. Cranmer, E. Gross, and O. Vitells. Asymptotic formulae for likelihood-based tests of new physics. *European Physical Journal C*, 71:1554, February 2011. (Cited on page 80.)

[104] Alexander L. Read. Presentation of search results: The CL(s) technique. *J. Phys.*, G28:2693–2704, 2002. [,11(2002)]. (Cited on page 80.)

[105] Georges Aad et al. Improved luminosity determination in pp collisions at sqrt(s) = 7 TeV using the ATLAS detector at the LHC. *Eur. Phys. J.*, C73(8):2518, 2013. (Cited on page 84.)

[106] Georges Aad et al. Determination of the tau energy scale and the associated systematic uncertainty in proton-proton collisions at $\sqrt{s} = 8$ TeV with the ATLAS detector at the LHC in 2012. Technical Report ATLAS-CONF-2013-044, CERN, Geneva, Apr 2013. (Cited on page 84.)

[107] https://twiki.cern.ch/twiki/bin/viewauth/AtlasProtected/TauRecommendationsWinterConf2013. (Cited on page 84.)

[108] https://twiki.cern.ch/twiki/bin/view/AtlasProtected/EGammaCalibrationGEO20. (Cited on page 84.)

[109] https://twiki.cern.ch/twiki/bin/viewauth/AtlasProtected/MCPAnalysisGuidelinesData2012. (Cited on page 84.)

[110] https://twiki.cern.ch/twiki/bin/viewauth/AtlasProtected/EfficiencyMeasurements2012. (Cited on page 84.)

[111] The ATLAS Jet Energy Scale Uncertainty Recommendations. https://twiki.cern.ch/twiki/bin/viewauth/AtlasProtected/JetUncertainties2012. (Cited on page 85.)

[112] The ATLAS Jet Energy Scale Correlation Recommendations. https://twiki.cern.ch/twiki/bin/viewauth/AtlasProtected/JESCorrelationRecommendations. (Cited on page 85.)

[113] The ATLAS Jet Energy Resolution Recommendations. https://twiki.cern.ch/twiki/bin/viewauth/AtlasProtected/ApplyJetResolutionSmearing. (Cited on page 85.)

[114] The ATLAS ETmiss Recommendations. https://twiki.cern.ch/twiki/bin/viewauth/AtlasProtected/METUtilSystematics. (Cited on page 86.)

[115] The ATLAS collaboration. Calibration of the performance of b-tagging for c and light-flavour jets in the 2012 ATLAS data. Technical Report ATLAS-CONF-2014-046, CERN, Geneva, Jul 2014. (Cited on page 86.)

[116] J R Andersen et al. Handbook of LHC Higgs Cross Sections: 3. Higgs Properties. 2013. (Cited on page 86.)

[117] J Butterworth, E Dobson, U Klein, B Mellado Garcia, T Nunnemann, J Qian, D Rebuzzi, and R Tanaka. Single Boson and Diboson Production Cross Sections in pp Collisions at sqrts=7 TeV. Technical Report ATL-COM-PHYS-2010-695, CERN, Geneva, Aug 2010. (Cited on pages 86 and 93.)

A special thanks to Olya for her continuous support, patience, motivation, knowledge and kindness. I could not have had a better advisor and mentor. Thanks to the many people who gave me their time, help and expertise. I know you had better things to do. And lastly, thanks to everyone for the fun times and fond memories.

UNIVERSITY OF AMSTERDAM